



JBISE

ISSN: 1937-6871

Volume 3 Number 8 August 2010

Journal of Biomedical Science and Engineering



ISSN: 1937-6871



Editor-in-Chief
Kuo-Chen Chou

Journal Editorial Board

ISSN 1937-6871 (Print) ISSN 1937-688X (Online)

<http://www.scirp.org/journal/jbise>

Editor-in-Chief

Prof. Kuo-Chen Chou

Gordon Life Science Institute, San Diego, California, USA

Editorial Board (According to Alphabet)

Prof. Suleyman I. Allakhverdiev	Institute of Basic Biological Problems, Russia
Prof. Christopher J. Branford-White	London Metropolitan University, UK
Prof. Thomas Casavant	University of Iowa, USA
Dr. Arezou Ghahghaei	University of Sistan ad Baluchistan, Iran
Prof. Reba Goodman	Columbia University, USA
Prof. Fu-Chu He	Chinese Academy of Science, China
Prof. Robert L. Heinrikson	Proteos, Inc., USA
Prof. Zeng-Jian Hu	Howard University, USA
Prof. Sami Khuri	San Jose State University, USA
Prof. Takeshi Kikuchi	Ritsumeikan University, Japan
Prof. Rob Krams	Imperial College, UK
Prof. Lukasz Kurgan	University of Alberta, Canada
Dr. Girdhar K. Pandey	University of Delhi South Campus, India
Prof. Zhi-Pei Liang	University of Illinois, USA
Prof. Juan Liu	Wuhan University, China
Dr. Patrick Ma	The Hong Kong Polytechnic University, China
Dr. Bouzid Menaa	Fluorotronics, Inc. USA
Prof. Eddie Ng	Technological University, Singapore
Prof. Harold A. Scheraga	Cornell University, USA
Prof. Hong-Bin Shen	Shanghai Jiaotong University, China
Prof. Min-Gui Sun	University of Pittsburgh, USA
Prof. Yan-Mei Tie	Harvard Medical School, USA
Dr. Elif Derya Ubeyli	TOBB University of Economics and Technology, Turkey
Prof. Ching-Sung Wang	Oriental Institute Technology, Taiwan (China)
Prof. Dong-Qing Wei	Shanghai Jiaotong University, China
Prof. Zhi-Zhou Zhang	Harbin Institute of Technology, China
Prof. Jun Zhang	University of Kentucky, USA

Editorial Assistant

Shirley Song

Scientific Research Publishing, USA. Email: jbise@scirp.org

Guest Reviewers(According to Alphabet)

Odilio B. G. Assis	Giuseppe Ferri	Michael Komaitis	Rangaraj M. Rangayyan
Jacques M.T. de Bakker	Yong Hu	A. Maratea	Ajit Sadana
Adrian Baranchuk	Darius Jegelevicius	Nahel N. Saied MB	Nina F. Schor
P. K. Chan	Kyu-Young Kim	Jagadish Nayak	Pier Andrea Serra
Long Cheng	Shuzo Kobayashi	Adriaan van oosterom	Jong-Pil Son
Chua Kuang Chua	Du-Yih Tsai	Qing-Ping Sun	

TABLE OF CONTENTS

Volume 3, Number 8, August 2010

Dextran coating on and among fibers of polymer sponge scaffold for osteogenesis by bone marrow cells *in vivo*

M. Yoshikawa, N. Tsuji, H. Kakigi, T. Yabuuchi, Y. Shimomura, H. Hayashi, H. Ohgushi.....751

Antimicrobial activity of the autochthonous compound Enoxil

L. Lupaşcu, V. Rudic, V. Cotos, T. Lupaşcu.....758

MRI monitoring of lesions created at temperature below the boiling point and of lesions created above the boiling point using high intensity focused ultrasound

C. Damianou, K. Ioannides, V. Hadjisavvas, N. Mylonas, A. Couppis, D. Iosif, P. A. Kyriacou.....763

Anisotropic WM conductivity reconstruction based on diffusion tensor magnetic resonance imaging: a simulation study

D. D. Yan, W. L. Xu, J. Li.....776

Categorizing HIV-1 subtypes using an ant-based clustering algorithm

D. King, W. Hu.....785

Innovative data mining approaches for outcome prediction of trauma patients

E.-M. Theodoraki, S. Katsaragakis, C. Koukouvinos, C. Parpoula.....791

Uncovering preferences from patient list data using benefit efficient models

J. Ubøe, J. Lillestøl.....799

Study of the bones tissue reparation using nanostructured titanium implants with hydroxylapatite coatings by scanning electron microscopy

T. V. Pavlova, S. Y. Zaitsev, L. A. Pavlova, D. A. Kolesnikov.....807

Shoulder joint flexibility in top athletes

H. Daneshmandi, F. Rahmaninia, H. Shahrokhi, P. Rahmani, S. Esmaeili.....811

Use of instantaneous energy of ABR signals for fast detection of wave V

A. Arooj, M. M. Rushaidin, S.-H. Salleh, M. H. Omar.....816

Tele-care for emergency announcements

C.-S. Wang, C.-W. Liu, T.-W. Wang.....822

Use of traditional Chinese medicine in HIV/AIDS in China

J. Wang, W. Zou, Y. Liu.....828

Journal of Biomedical Science and Engineering (JBiSE)

Journal Information

SUBSCRIPTIONS

The *Journal of Biomedical Science and Engineering* (Online at Scientific Research Publishing, www.SciRP.org) is published monthly by Scientific Research Publishing, Inc., USA.

Subscription rates:

Print: \$50 per issue.

To subscribe, please contact Journals Subscriptions Department, E-mail: sub@scirp.org

SERVICES

Advertisements

Advertisement Sales Department, E-mail: service@scirp.org

Reprints (minimum quantity 100 copies)

Reprints Co-ordinator, Scientific Research Publishing, Inc., USA.

E-mail: sub@scirp.org

COPYRIGHT

Copyright©2010 Scientific Research Publishing, Inc.

All Rights Reserved. No part of this publication may be reproduced, stored in a retrieval system, or transmitted, in any form or by any means, electronic, mechanical, photocopying, recording, scanning or otherwise, except as described below, without the permission in writing of the Publisher.

Copying of articles is not permitted except for personal and internal use, to the extent permitted by national copyright law, or under the terms of a license issued by the national Reproduction Rights Organization.

Requests for permission for other kinds of copying, such as copying for general distribution, for advertising or promotional purposes, for creating new collective works or for resale, and other enquiries should be addressed to the Publisher.

Statements and opinions expressed in the articles and communications are those of the individual contributors and not the statements and opinion of Scientific Research Publishing, Inc. We assume no responsibility or liability for any damage or injury to persons or property arising out of the use of any materials, instructions, methods or ideas contained herein. We expressly disclaim any implied warranties of merchantability or fitness for a particular purpose. If expert assistance is required, the services of a competent professional person should be sought.

PRODUCTION INFORMATION

For manuscripts that have been accepted for publication, please contact:

E-mail: jbise@scirp.org

Dextran coating on and among fibers of polymer sponge scaffold for osteogenesis by bone marrow cells *in vivo*

Masataka Yoshikawa^{1,2}, Norimasa Tsuji¹, Hideyuki Kakigi¹, Takayoshi Yabuuchi¹, Yasunori Shimomura¹, Hiroyuki Hayashi¹, Hajime Ohgushi²

¹Department of Endodontics, Osaka Dental University, Osaka, Japan;

²Tissue Engineering Research Group, Health Research Institute, National Institute of Advanced, Industrial Science and Technology, Amagasaki, Japan.

Email: yosikawa@cc.osaka-dent.ac.jp

Received 25 May 2010; revised 8 June 2010; accepted 20 June 2010.

ABSTRACT

Although hydroxyapatite is commonly used as a scaffold for bone regeneration, sponges may be suitable because of the adaptability to the defect. To use as a scaffold, the fiber of sponge would be coated with any adhesive to storage stem cells in the sponges. Fiber in the structure of commercially available sponges was coated by immersion in dextran solution and air dried. After seeding of rat bone marrow cells (rBMCs), the sponges were implanted subcutis of rats for estimate osteogenesis *in vivo*. The level of osteocalcin was 25.28 ± 5.71 ng/scaffold and that of Ca was 129.20 ± 19.69 μ g/scaffold. These values were significantly higher than those in sponges without dextran coating ($p < 0.01$). It was thought that rBMCs could be stored on the shelf by dextran deposition in the fiber of the sponge. *In vivo* examination, dextran induced osteogenesis by rBMCs in many spaces in the inner structure of the sponge.

Keywords: Dextran; Cell Adhesion; Scaffold; Bone Marrow Cells; Osteogenesis

1. INTRODUCTION

A part or total tooth regeneration has been studied by many researchers [1-5]. In a basic study for tooth regeneration, it was shown that stem cells were detected in the tooth pulp [6]. And it was shown in the report that the stem cells differentiated to osteoblasts, chondrocytes, adipocytes or neurocytes. Development of the removed tooth germ to mature tooth was also attempted *in vitro* [7]. However, tooth regeneration by tissue engineering is particularly difficult because the constitution and configuration of a tooth is complex. Odontoblasts, ameloblasts and cement blasts will be required for tooth regeneration. Methods to isolate these cells from tissue or

technique for differentiation and induce these blast cells from stem cells are not still established. This may be one of the reasons that tooth regeneration is not realized. Restoration of partial defect of the tooth or reproduction of the whole tooth that had been missed for any reason should be a definitive goal of the regenerative therapy in the dentistry. Also, for regeneration of tooth, isolation from the tissue of odontoblasts, ameloblasts and cementoblasts, and induction of differentiation from stem cells to these blast cells would be required. However, these methods have not yet been established.

It is well-known that bone consists of an apatite structure like dentine. Furthermore, osteocalcin which should be synthesized by osteoblasts is present in dentine as calcium-binding protein [8,9]. Therefore, for the restoration of teeth, a method of substituting bone which resembles dentine in properties should be established. For the regeneration of tooth or bone with a three-dimensional structure, a scaffold for proliferation and differentiation of bone marrow stem cells and osteogenesis is required. Sufficient resistance to load in the living body is required for regenerated hard tissue.

The morphology of the scaffold should be easily modifiable in order to apply the technique to any configuration of defects. The intensity of the sponge as a scaffold is extremely low, but modification of the shape is easy. Polyvinyl alcohol (PVA) sponge with bone marrow cells was used for bone regeneration in the defective part of the bone [10]. In this study, commercially available polyvinyl formal (PVF) sponge was selected as the scaffold. PVF sponge consists of PVA cross-linked construction by formalin. Stem cells must attach to the structure of the scaffold to induce osteogenesis by the cells in a porous scaffold [11,12]. However, the sponge is inappropriate for keeping cells because of the fibrous construction. One of the methods for seeding many cells to attach in the pores of scaffold is coating with a

chemical substance that promotes cell adhesion on the scaffold [13]. Dextran, which has superior biocompatibility [14], is a natural polymer with linkage of a large number of D-glucose, and is a kind of polysaccharide existing in extracellular matrix. Dextran promotes adhesion between protein and cells [15].

This experiment investigated the effect of dextran to induce stem cell differentiation in dextran-coated PVF sponge. To confirm the effects of dextran and the availability the PVF sponge as a scaffold, coating of a PVF sponge with dextran was accomplished by immersion in dextran solution and *in vivo* examinations were performed.

2. MATERIALS AND METHODS

2.1. Experimental Animals

In this study, 6- and 7-week-old male Fischer 344 rats (CLEA Japan Inc., Tokyo, Japan) were used. The Animal Welfare Committee of Osaka Dental University approved the experimental procedures regarding use and care of animals in this study. This study was performed under the Guidelines for Animal Experimentation at Osaka Dental University.

2.2. Rat Bone Marrow Cell (rBMC) Isolation

rBMCs were obtained from the bone shaft of femora of six 6-week-old male Fischer 344 rats after euthanasia by intraperitoneal overdose of sodium pentobarbital (Dainippon-Sumitomo Pharmaceutical Co., Ltd., Osaka, Japan) essentially according to the methods described in previous reports [16,17] with minimal modification. Both ends of the femur were cut off at the epiphysis and bone marrow was flushed out with 10 ml of minimum essential medium (MEM: Nakalai Tesque Inc., Kyoto, Japan) expelled from a syringe through a 21-gauge needle.

2.3. Primary Culture for Preparing rBMCs Suspension

rBMCs in 10 ml of MEM were removed in a cell culture flask (T75: BD Biosciences, MA, USA). For primary culture, MEM supplemented with 15% fetal bovine serum (FBS: JRH Biosciences, KS, USA) and antibiotics (100 units/ml penicillin, 100 µg/ml streptomycin, and 0.25 µg/ml amphotericin B; Sigma Chemical Co., MO, USA) was prepared. Primary culture was performed for 1 week in T75 in 5% CO₂ and 95% relative humidity at 37°C in an incubator. The culture medium was renewed twice.

After primary culture, rBMCs in T75 culture flask were washed three times using phosphate buffer solution without Ca²⁺ and Mg²⁺ (PBS (-): Nakalai Tesque Inc.) and the cells were isolated from the bottom of T75 flask

with trypsin-EDTA (0.5 mg/ml trypsin and 0.53 µmol EDTA: Nakalai Tesque Inc.) solution. Harvested cells were re-suspended in culture medium at 1×10^7 cells/ml concentration.

2.4. Dextran Coating of Polyvinyl Formal (PVF) Sponge and rBMCs Seeding in the Sponges

PVF sponges made by formalization of polyvinyl alcohol were generously donated by Ione (Osaka, Japan). PVF sponges with a cubic configuration (5 × 5 × 5 mm) for use in this study were obtained by cutting from a sheet. Pores were 130 µm diameter on average. The PVF sponges were sterilized in ethylene oxide gas before use.

Dextran with 10 kDa of molecular weight was purchased from Sigma-Aldrich (MO, USA) and dissolved at 2 g/dl concentration in ultra purified water. The liquid was sterilized by filtration (0.22 µm) (Millex®: Milipore Japan, Tokyo, Japan). The sponges were immersed in dextran solution for 24 hours. The sponges used as a control were immersed in ultra purified water. The sponges were air-dried under radiation with ultraviolet light. Each of the PVF sponges with and without immersion in dextran solution were respectively seeded with 1×10^6 rBMCs in a 0.1 ml cell suspension and were incubated for 3 hours in 5% CO₂ and 95% relative humidity at 37°C to promote cell adhesion in the sponges.

The micro structures of PVF sponges with and without immersion in dextran solution were observed by scanning electron microscopy (SEM, JSM 5400: JEOL DATUM Ltd., Tokyo, Japan). For SEM confirmation of whether the dextran coating on sponge fiber would be preserved during rBMCs seeding and subcutaneous implantation, sponges that had been immersed in dextran solution were stored in MEM for 4 weeks in 5% CO₂ and 95% relative humidity at 37°C.

2.5. Dorsal Subcutaneous Implantation of PVF Sponge with rBMCs

For *in vivo* osteogenesis in PVF scaffolds, six of 7-week-old male Fischer 344 rats were used. Under general anaesthesia with intra-peritoneal injection of 0.04 mg/g body weight of sodium pentobarbital, the backs of rats were shaved and disinfected with povidone iodine (Isodine®: Meiji Seika Kaisha Ltd., Tokyo, Japan). The dorsal skin of the rat was incised close to the scapula on both sides across the vertebra at right angles and subcutaneous pockets were made using a mucosal raspator. All rats were respectively implanted with four scaffolds in individual subcutaneous pockets alongside the vertebra. Two scaffolds without dextran coating but with rBMCs seeding were inserted in the left subcutaneous

pocket of three rats and the other two with dextran coated and rBMCs seeding were inserted in the right side of the other three rats. The incised wounds were sutured, and adhesive (Aron alpha®: Toa-gosei Co., Ltd., Tokyo, Japan) was applied over the wounds. Implanted scaffolds were removed from the dorsal subcutaneous tissue of the rats 4 weeks postoperatively after euthanasia by intraperitoneal injection of excessive dose of sodium pentobarbital.

2.6. Histological Examination of Osteogenesis in Implanted Scaffolds

Three of each removed scaffold with or without dextran coating and with rBMCs seeding were fixed in 10% buffered formalin solution (pH 7.2). Specimens were decalcified in 10% formic acid solution for two days, embedded in paraffin, and 6 μ m serial sections were made. All sections were stained with hematoxylin-eosin and examined under an optical microscope.

2.7. Immunochemical and Biochemical Examination of Osteogenesis in Implanted Scaffolds

The other remaining sponges removed from rat subcutaneous tissue were frozen in liquid nitrogen and crushed respectively using a Mixer Mill (MM 301: Retsch Co., Ltd., Tokyo, Japan). The crushed samples were respectively added to 1 ml of buffer solution (pH 7.4) consisting of 10 mM Tris-HCl, 1 mM EDTA and the 100 mM NaCl. The cells in the solution were sonicated for 30 seconds at 3°C (BIORUPTOR UCW-201: Tosho Electric Co., Ltd., Tokyo, Japan). The samples were centrifuged for 1 minute at 16,000 \times g. The supernatants were used for quantitative analysis of osteocalcin (Rat Osteocalcin ELISA kit DS®; DS Pharma Biomedical Co., Ltd., Osaka, Japan). Then, 1 ml of formic acid was individually added to each precipitation and samples were decalcified for 72 hours for analyze calcium quantity in each sponge using Calcium-E test WAKO® (Wako Pure Chemical Co. Inc., Osaka, Japan).

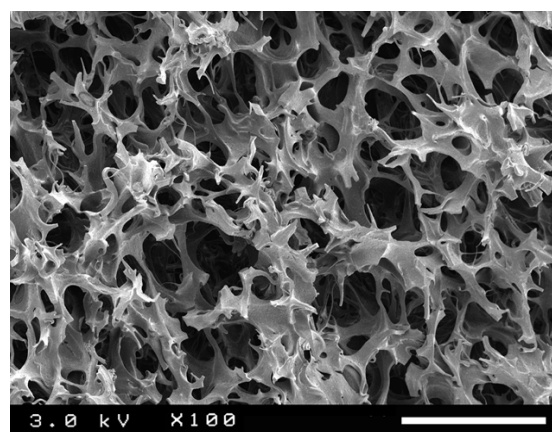
Data were presented as mean \pm standard deviations. Statistical comparisons between the mean values of osteocalcin in implanted scaffolds were performed using two-way unreplicated ANOVA followed by post hoc analysis using Tukey-Kramer's test. Differences of $p < 0.01$ were considered significant.

3. RESULTS

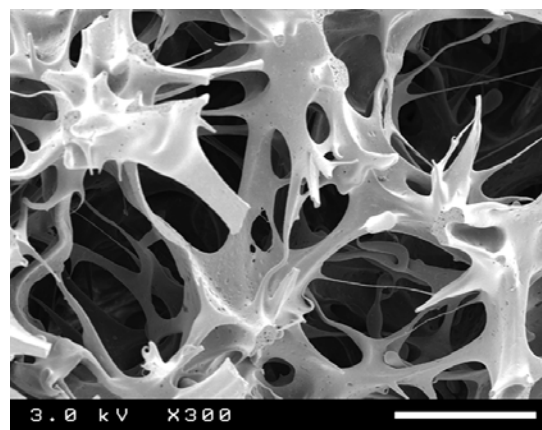
3.1. SEM Examination of PVF Sponges with and without Immersion in Dextran Solution

The SEM image of the PVF sponge without immersion in dextran solution showed reticular configuration as in **Figures 1(a)** and **(b)**. Sizes of the fibers ranged from

about 5 μ m in the fine portion to 150 μ m in the thick portion. The large nodes formed a spacious shelf and extended fibrous branches in every direction. The major axes were 150 to 250 μ m. The fibers of sponges immersed in dextran solution were larger in diameter than those of sponges without immersion in dextran solution (**Figures 2(a)** and **(b)**). Each fiber presented a thick plate with a width of 150-300 μ m. The fibers of the sponge seemed to be covered with viscous substance. The possibility that the dextran coating on the fiber was preserved under rBMCs seeding and during subcutaneous tissue implantation was shown by SEM observation of sponges that had been kept in MEM for 4 weeks after immersion in dextran solution (**Figure 3**). However, the surface of the substance on the fiber of sponge just after immersion in dextran solution was smoother than the surface of the sponge stored in MEM.

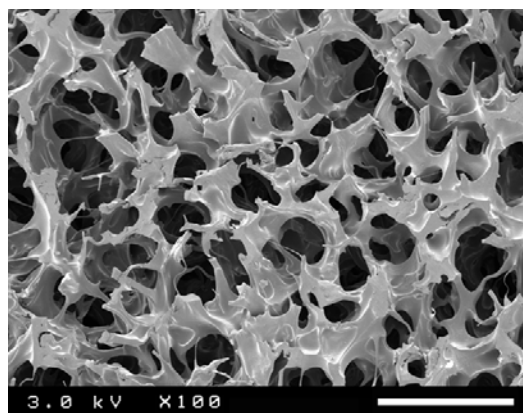


(a)

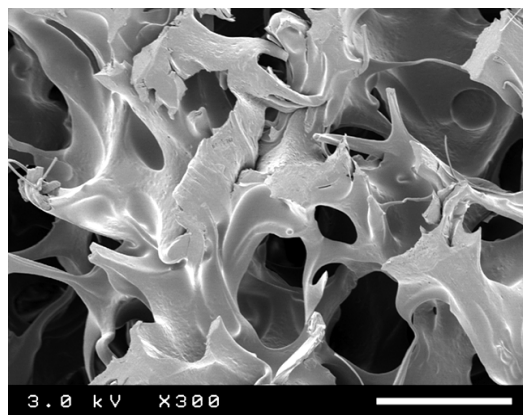


(b)

Figure 1. (a) SEM image of PVF sponge without immersion in dextran solution. Fine fibers connected with each other were observed in the interior of the sponge. (Bar: 300 μ m); (b) This illustrate shows image of higher magnification of **Figure 1(a)**. Fine fibers were clearly seen. (Bar: 100 μ m).



(a)



(b)

Figure 2. (a) SEM image of PVF sponge following immersion in the dextran solution. The fibers seemed to be covered with a viscous substance. (Bar: 300 μ m); (b) This illustration shows image of higher magnification of **Figure 2(a)**. Dense coating with dextran was seen on the fibers (Bar: 100 μ m).

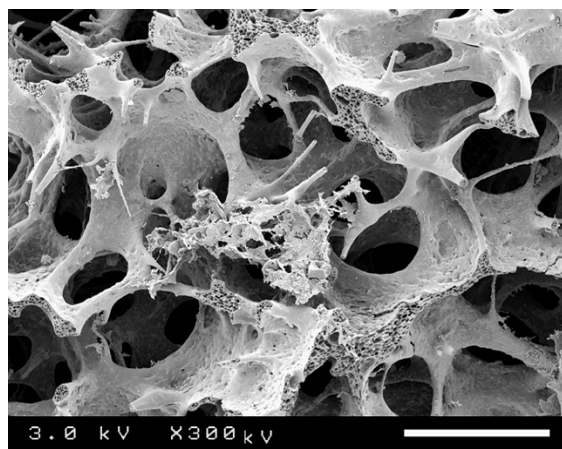


Figure 3. SEM image of dextran-coated PVF sponge After storage in MEM for 4 weeks following immersion in dextran solution (Bar: 100 μ m).

3.2. Effect of Dextran on Osteogenesis in the PVF Sponge used as a Scaffold *in vivo*: Histological Examination

Based on histological findings of PVF scaffold after a 4-week implantation in the rat subcutis, there was no bone recognized in the sponge without immersion in dextran solution prior to seeding of rBMCs as shown in **Figure 4**. Densely arranged fibrous connective tissue infiltrated the fibers of the sponge. In the sponge with immersion in dextran solution prior to rBMCs seeding, conspicuous osteogenesis was recognized on fibers accompanied by infiltration of connective tissue (**Figure 5**).

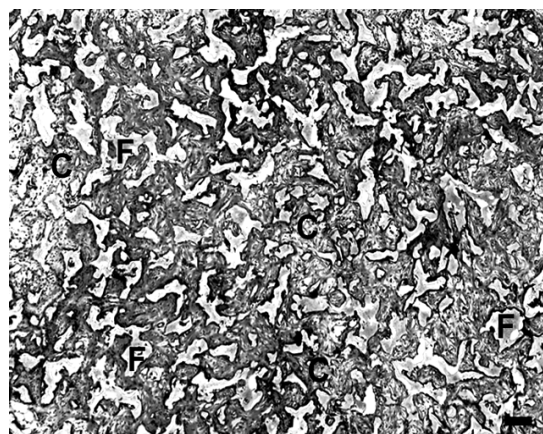


Figure 4. Histological findings of implanted PVF sponge without immersion in dextran solution before implantation. There was no apparent bone in the sponge. Between fibers of the sponge, densely arranged fibrous connective tissue was seen. C: Fibrous tissue infiltrated in the sponge; F: Fiber of sponge (Bar: 200 μ m).

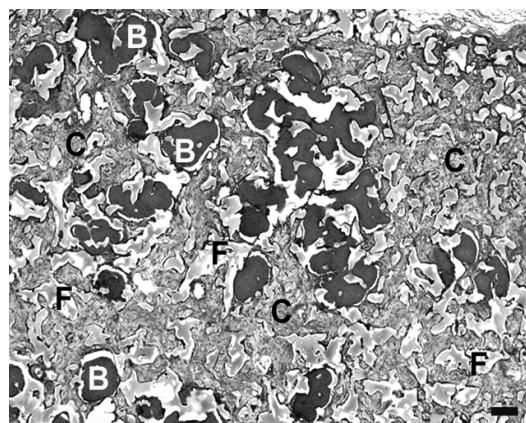


Figure 5. Histological findings of implanted PVF sponge immersed in dextran solution before implantation. Conspicuous osteogenesis was recognized among the fibers of sponge. Infiltrated fibrous connective tissue was also seen. B: Bone; C: Fibrous connective tissue infiltrated in the sponge; F: Fiber of sponge (Bar: 200 μ m).

3.3. Quantity of Osteocalcin in Implanted Sponge with and without Immersion in Dextran Solution: Immunochemical Quantitative Analysis

In the sponge without immersion in dextran solution before rBMCs seeding and subcutaneous tissue implantation, 9.42 ± 5.67 ng/scaffold of osteocalcin was measured. However, 25.28 ± 5.71 ng/scaffold of osteocalcin was detected in the sponge immersed in dextran solution. There was a significant difference between the sponges with and without immersion in dextran solution (Figure 6: $p < 0.01$).

3.4. Quantity of Calcium in Implanted Sponge with and without Immersion in Dextran Solution: Biochemical Quantitative Analysis

Quantity of calcium detected in the implanted sponge with immersion in dextran solution before rBMCs seeding was 129.20 ± 19.69 $\mu\text{g/scaffold}$ (Figure 7). In implanted sponge without immersion in dextran solution, detected quantity of calcium was 79.41 ± 8.69 $\mu\text{g/scaffold}$. There was a significant difference between the implanted sponges with and without immersion in dextran solution prior to seeding of rBMCs ($p < 0.01$).

4. DISCUSSION

The tooth is classified into an anterior tooth, a canine, a premolar and a molar tooth. Moreover, those are distinguished morphologically about a maxillary or a mandibular tooth, and left or right. Tooth configurations vary, and there are differing origins of hard tissues and pulp that

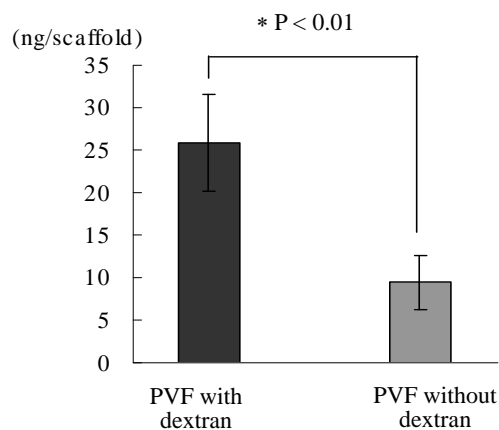


Figure 6. Osteocalcin level of implanted sponges with or without immersion in dextran solution prior to seeding of rBMCs. On comparison between sponges without and with immersion in dextran solution, there was a greater quantity of osteocalcin in sponges with dextran than in those without dextran. Values are means \pm SD ($n = 3$). * $p < 0.01$ vs. sponges with immersion in dextran solution.

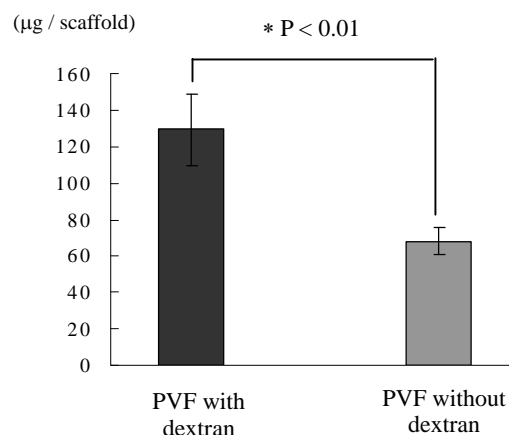


Figure 7. Calcium level of implanted sponges with or without immersion in dextran solution followed by seeding of rBMCs. On comparison between sponges with and without immersion in dextran solution, quantity of calcium was greater in sponges with immersion in dextran solution than in those without immersion in dextran solution. Values are means \pm SD ($n = 3$). * $p < 0.01$ vs. sponges with immersion in dextran solution.

construct a tooth. Therefore, tooth regeneration is difficult for the complicated configuration [18]. It was reported that a structure similar to a mature tooth including dentine, enamel, cementum and pulp was induced from a tooth germ *in vitro* [7]. For tooth regeneration, several steps will be required, such as restoration of the defect by regeneration of hard tissue, realization of endothelial and fibrous conjugation to a regenerated root, regeneration of the dentine-pulp complex, and then, complete tooth regeneration.

For restoration of a tooth defect, stem cells should be differentiated into odontoblasts from odontoblast precursor cells in a scaffold. Therefore, it would be desirable for the scaffold to be configured according to the defect. PVF sponge is considered a desirable scaffold material because it can easily be shaped to the configuration of the defect. PVF scaffold has previously been used for three-dimensional *in vivo* osteogenic examination [19]. On SEM observation, pores measuring about 100-280 μm in diameter were recognized in PVF sponge. It was reported that such a pore size is suitable for osteogenesis in an HA scaffold [20]. This finding suggests that osteogenesis in the PVF sponge is possible. However, there is a conspicuous difference in the internal structures of a hydroxyapatite (HA) scaffold and those of a PVF scaffold. Reticular structure of PVF sponge was shown by SEM findings. Stem cells seeded in PVF sponge may flow out of the sponge with the suspension, while HA scaffold, stem cells may be taken into the

pores. The PVF sponge is an unfavorable substrate for adhesion of BMCs.

Therefore, for osteogenesis in PVF sponge by subcutaneous tissue implantation *in vivo*, the sponge should be modified so that seeded stem cells could adhere in the sponge. In fact, it was reported that modification of PVA by extracellular matrix is necessary for adhesion and proliferation of stem cells in the sponge [21,22]. As a result of proliferation and differentiation to osteoblasts of stem cells, bone is formed. In this *in vivo* study of seeding bone marrow cells in PVF sponge, there was no osteogenesis recognized in the sponge without dextran coating. This finding showed that rBMCs did not adhere to the construction in the PVF scaffold. PVA having aldehyde groups and hydroxyl groups as functional groups reacts with formalin and produces acetal in the intramolecule of PVA. As a result, it is thought that these functional groups were covered and lost reactivity. PVF sponge without functional group could not be used as a scaffold for osteogenesis by BMCs.

It was reported that intercellular adhesion involves direct binding by cell adhesion molecule in an extracellular matrix or cell membrane [21,22]. In addition, the cells are activated by stimulus from cytokine and adhesive high polymer and adhere to the surface of the scaffold [23]. By coating the inner structures of PVF with a highly cytotropic substance, adhesion of seeded stem cells is enabled.

It is known that dextran is a major extracellular matrix and it is a natural macromolecule polysaccharide. Furthermore, dextran shows excellent biocompatibility and adhesiveness to protein and cells [15]. It has also been reported that dextran promotes differentiation of BMCs to osteoblasts [24]. Therefore, rBMCs may adhere to PVF sponge through dextran. It is evident that stable adhesion may occur between PVF sponge and dextran [25,26]. Based on the SEM findings in this experiment, it seemed that the internal structures of the PVF sponge were covered with a layer of dextran after immersion in the solution. Osteogenesis was subsequently recognized in the PVF scaffold that had been immersed in dextran solution. These findings show that dextran adhered sufficiently to the internal structure of the sponge and facilitated the attachment of the rBMCs. It was reported that dextran agglutinates BMCs and then promoted adherence of the cells to the pore wall in the scaffold [27,28].

Greater osteogenesis was induced by 10 kDa of dextran in PVF sponge than by higher molecular weight dextran. It is necessary to retain BMCs in the PVF sponge for effective osteogenesis. One method to achieve the purpose appears to be using low-molecular-weight dextran to coat the scaffold. It was suggested in

this study that coating PVF sponge with low-molecular-weight dextran (10 kDa) effectively promoted osteogenesis in the sponge.

5. CONCLUSIONS

For regeneration of a tooth defect, in this study, PVF sponge was selected as the scaffold because it could be easily shaped and showed excellent biocompatibility. In addition, it was considered that dextran was useful to promote adhesion of BMCs. *In vivo* osteogenesis by rBMCs in PVF sponge as a scaffold with dextran coating was examined histologically, biochemically and immunochemically.

The findings obtained from this study were as follows.

1) rBMCs did not adhere to untreated PVF sponge and no bone was formed.

2) The fiber in PVF sponge should be covered with a layer of the dextran by immersion in a solution of 10kDa dextran.

3) In PVF sponge immersed in dextran solution, the dextran layer coating the inner structure of the sponge persisted after 4 week immersion in MEM.

4) In PVF sponge coated with dextran, osteogenesis by rBMCs was promoted.

REFERENCES

- [1] Yamada, Y., Ueda, M., Naiki, T. and Nagasaka, T. (2004) Tissue-engineered injectable bone regeneration for osseointegrated dental implants. *Clinical Oral Implants Research*, **15**(5), 589-597.
- [2] Ohazama, A., Modino, S.A., Miletich, I. and Sharpe, P.T. (2004) Stem-cell-based tissue engineering of murine teeth. *Journal of Dental Research*, **83**(7), 518-522.
- [3] Hu, B., Unda, F., Bopp-Kuchler, S., Jimenez, L., Wang, X.J., Haikel, Y., Wang, S.L. and Lesot, H. (2006) Bone marrow cells can give rise to ameloblast-like cells. *Journal of Dental Research*, **85**(5), 416-421.
- [4] Yen, A.H. and Sharpe, P.T. (2008) Stem cells and tooth tissue engineering. *Cell Tissue Research*, **331**(1), 359-372.
- [5] Jing, W., Wu, L., Lin, Y., Liu, L., Tang, W. and Tian, W. (2008) Odontogenic differentiation of adipose-derived stem cells for tooth regeneration: Necessity, possibility, and strategy. *Medical Hypotheses*, **70**(3), 540-542.
- [6] Duailibi, M.T., Duailibi, S.E., Young, C.S., Bartlett, J.D., Vacanti, J.P. and Yelick, P.C. (2004) Bioengineered teeth from cultured rat tooth bud cells. *Journal of Dental Research*, **83**(7), 523-528.
- [7] Zhang, W., Walboomers, X.F., Van Kuppevelt, T.H., Daamen, W.F., Van Damme, P.A. and Bian, Z., (2008) *In vivo* evaluation of human dental pulp stem cells differentiated towards multiple lineages. *Journal of Tissue Engineering and Regenerative Medicine*, **2**(2-3), 117-125.
- [8] Satoyoshi, M., Koizumi, T., Teranaka, T., Iwamoto, T., Takita, H., Kuboki, Y., Saito, S. and Mikuni-Takagaki, Y. (1995) Extracellular processing of dentin matrix protein in the mineralizing odontoblast culture. *Calcified Tissue*

- International*, **57**(3), 237-241.
- [9] Papagerakis, P., Berdal, A., Mesbah, M., Peuchmaur, M., Malaval, L., Nydegger, J., Simmer, J. and Macdougall, M. (2002) Investigation of osteocalcin, osteonectin, and dentin sialophosphoprotein in developing human teeth. *Bone*, **30**(2), 377-385.
 - [10] Jeong, W.K., Oh, S.H., Lee, J.H. and Im, G.I. (2008) Repair of osteochondral defects with a construct of mesenchymal stem cells and a polydioxanone/poly (vinyl alcohol) scaffold. *Biotechnology and Applied Biochemistry*, **49**(2), 155-164.
 - [11] Robinson, B.P., Hollinger, J.O., Szachowicz, E.H. and Brekke, J. (1995) Calvarial bone repair with porous D, L-polylactide. *Otolaryngology-Head and Neck Surgery*, **112**(6), 707-713.
 - [12] Chang, Y.S., Oka, M., Kobayashi, M., Gu, H.O., Li, Z.L., Nakamura, T. and Ikada, Y. (1996) Significance of interstitial bone ingrowth under load-bearing conditions: A comparison between solid and porous implant materials. *Biomaterials*, **17**(11), 1141-1148.
 - [13] Nuttelman, C.R., Mortisen, D.J., Henry, S.M. and Anseth, K.S. (2001) Attachment of fibronectin to poly (vinyl alcohol) hydrogels promotes NIH3T3 cell adhesion, proliferation, and migration. *Journal of Biomedical Materials Research*, **57**(2), 217-223.
 - [14] Cadée, J.A., van Luyn, M.J., Brouwer, L.A., Plantinga, J.A., van Wachem, P.B., de Groot, C.J., den Otter, W. and Hennink, W.E. (2000) *In vivo* biocompatibility of dextran-based hydrogels. *Journal of Biomedical Materials Research*, **50**(3), 397-404.
 - [15] Liu, J.M., Haroun-Bouhedja, F. and Boisson-Vidal, C. (2000) Analysis of the *in vitro* inhibition of mammary adenocarcinoma cell adhesion by sulfated polysaccharides. *Anticancer Research*, **20**(5A), 3265-3271.
 - [16] Maniopoulos, C., Sodek, J. and Melcher, A.H. (1988) Bone formation *in vitro* by stromal cells obtained from bone marrow of young adult rats. *Cell and Tissue Research*, **254**(2), 317-330.
 - [17] Ohgushi, H., Dohi, Y., Katuda, T., Tamai, S., Tabata, S. and Suwa, Y. (1996) *In vitro* bone formation by rat marrow cell culture. *Journal of Biomedical Materials Research*, **32**(3), 333-340.
 - [18] Lemus, D. (1995) Contributions of hetero specific tissue recombinations to odontogenesis. *International Journal of Developmental Biology*, **39**(1), 291-297.
 - [19] Lewin-Epstein, J., Azaz, B. and Ulmansky, M. (1969) Fate of osteogenic tissue transferred to the subcutaneous area by means of polyvinyl-formal sponge. *Israel Journal of Medical Sciences*, **5**(2), 365-372.
 - [20] Tsuruga, E., Takita, H., Itoh, H., Wakisaka, Y. and Kuboki, Y. (1997) Pore size of porous hydroxyapatite as the cell-substratum controls BMP-induced osteogenesis. *The Journal of Biochemistry*, **121**(2), 317-324.
 - [21] Zajackowski, M.B., Cukierman, E., Galbraith, C.G. and Yamada, K.M. (2003) Cell-matrix adhesions on poly (vinyl alcohol) hydrogels. *Tissue Engineering*, **9**(3), 525-533.
 - [22] Tsuji, Y., Yoshimura, N., Aoki, H., Sharov, A.A., Ko, M.S., Motohashi, T. and Kunisada, T. (2008) Maintenance of undifferentiated mouse embryonic stem cells in suspension by the serum- and feeder-free defined culture condition. *Developmental Dynamics*, **237**(8), 2129-2138.
 - [23] Wang, Y.W., Wu, Q. and Chen, G.Q. (2003) Reduced mouse fibroblast cell growth by increased hydrophilicity of microbial polyhydroxyalkanoates via hyaluronan coating. *Biomaterials*, **24**(25), 4621-4629.
 - [24] Li, D., Dai, K. and Tang, T. (2008) Effects of dextran on proliferation and osteogenic differentiation of human bone marrow-derived mesenchymal stromal cells. *Cytotherapy*, **10**(6), 587-596.
 - [25] Cascone, M.G., Maltinti, S., Barbani, N. and Laus, M. (1999) Effect of chitosan and dextran on the properties of poly (vinyl alcohol) hydrogels. *Journal of Materials Science: Materials in Medicine*, **10**(7), 431-435.
 - [26] Thébaud, N.-B., Pierron, D., Bareille, R., Le Visage, C., Letourneur, D. and Bordenave, L. (2007) Human endothelial progenitor cell attachment to polysaccharide-based hydrogels: A pre-requisite for vascular tissue engineering. *Journal of Materials Science: Materials in Medicine*, **18**(2), 339-345.
 - [27] Noble, B.S., Dean, V., Loveridge, N. and Thomson, B.M. (1995) Dextran sulfate promotes the rapid aggregation of porcine bone-marrow stromal cells. *Bone*, **17**(4), 375-382.
 - [28] Lévesque, S.G., Lim, R.M. and Shoichet, M.S. (2005) Macroporous interconnected dextran scaffolds of controlled porosity for tissue-engineering applications. *Biomaterials*, **26**(35), 7436-7446.

Antimicrobial activity of the autochthonous compound Enoxil

Lucian Lupaşcu¹, Valeriu Rudic^{1,2}, Viorica Cotos³, Tudor Lupaşcu⁴

¹Institute of Microbiology and Biotechnology of the ASM, Chişinău, Moldavia;

²Academy of Sciences of Moldova (ASM), Chişinău, Moldavia;

³Hospital of Contagious Diseases “T. Ciorba”, Chişinău, Moldavia;

⁴Institute of Chemistry of the ASM, Chişinău, Moldavia.

Email: lucian1978@mail.ru

Received 24 February 2010; revised 18 March 2010; accepted 31 March 2010.

ABSTRACT

The paper presents data about the antimicrobial activity of the autochthonous compound of tannin source Enoxil. The minimal inhibitory and bactericidal/fungicidal concentrations were established for some skin and wound infectious agents. It was established, based on *Pseudomonas* bacteria model, that the Enoxil compound suppress the activity of some important enzymes—a phenomenon that leads to the increase of bacterial sensibility to many tested antibiotics.

Keywords: Bacteria; Compound; Tannins; Wound; Infection

1. INTRODUCTION

Skin and wound infections, although more characteristic for countries with low economic level and low hygiene standards [1], have lately become a serious concern for highly socio-economically developed countries, as well [2-5]. Of great concern are also the intrahospital plague infections, as they complicate the recovering process, produce anxiety, increase patient's discomfort and may lead to death, being at the same time a serious threat to the medical worker [5,6]. The economical aspects of infections are also considerable [7]. The most frequent microorganisms in the derma or the purulent wound are the gram-positive bacteria *Staphylococcus aureus* and the gram-negative bacteria *Escherichia coli*, *Pseudomonas aeruginosa* [8]. Special attention is paid to pseudomonadic infections as complications of combustions, traumas, tattoo procedures, cellulites, decubital chronic ulcers, folliculitis [9-11].

One of the traditional methods of fighting infections is the use of antibiotics. However, a concerning phenomenon is observed lately in the entire world, including the Republic of Moldova—resistance of microorganisms to

these compounds [12,13]. A permanent and, often, abusive treatment with antibiotics had as a result the selection of new virulences, aggressive and severe, with a high genetic resistance potential. This situation directs the specialists in the field towards the elaboration of antimicrobial compounds on the basis of novel action mechanisms [14]. Albeit the use of tannin extracts from plants for the treatment of various derma and plague infections has been known for a long time, these don't exhibit the expected effect for many microorganisms [15-17]. At the moment, the number of efficient medicinal compounds, elaborated on the basis of tannin compounds is quite low, mostly due to the insolubility of many of them in aqueous or alcoholic solutions. The capacity of phenolic (tannin) extracts to disinfect and rapidly treat wounds is based on two fundamental phenomena—antimicrobial and antioxidant activities, determined by a series of mechanisms: capturing of iron ions from the substrate, thus depriving microorganisms of compounds necessary for their physiological activity; their binding to microbial proteins and formation of complexes; capturing of free radicals; absorption of oxygen radicals; inhibition of low density lipoproteins oxidation [18]. It is known that grape seeds are a rich source of so called enotannins—condensed tannins which represent a wide variety of natural substances with polyphenolic structure, remarkable due to the high content of proanthocyanidins [19]. There are enotannins in industrial quantities in the Republic of Moldova. Taking into account that many tannins with antimicrobial properties are insoluble in water, as well as the growing microbial resistance to vegetal tannins, of great potential are researches regarding the possibility of structural modification of enotannins, increase of their oxidation number, in order to increase their efficiency and to use them for the treatment of skin and plague infections.

The objective of present researches was to elucidate the antimicrobial activity of the autochthonous com-

pound Enoxil of tanninic origin.

2. MATERIALS AND METHODS

Research was carried out at the Department of Microbiology, Immunology and Virusology of the State University of Medicine and Pharmaceutics “N.Testemiteanu”.

The autochthonous compound Enoxil served as the antimicrobial remedy, obtained by hydro-solubilization of enotannins using chemical and physico-chemical procedures [20]. As microbial cultures, served several pathogens with severe implications in many contagious diseases—bacteria *Staphylococcus aureus*, *Escherichia coli*, *Salmonella abony*, *P.aeruginosa*, *Proteus vulgaris* and the fungus *Candida albicans*.

In order to determine the level of activity of the tested compound, the values of minimal inhibiting concentration (MIC) and the minimal bactericidal/fungicidal concentration (MBC/MFC) were used [21]. As test indices of the action of Enoxil on the *P.aeruginosa* bacteria, served a range of important biochemical parameters – indices of bacterial viability and pathogenicity: synthesis of cytochrome oxidase, citrate reductase, haemolysins, pyocyanin, odour presence, and as the index of sensibility towards antibiotics—zone of inhibition (mm) of the culture, specific to each antibiotic. The sensibility of the *P.aeruginosa* bacteria was determined using the method of antibiotics diffusion in gelose from roundels [22] that contained the following antibiotics homologated in the Republic of Moldova: cloramfenicol (30 mkg), pefloxacin (5 mkg), erythromycin (15 mkg), cefuroxim (30 mkg), ceftioxin (30 mkg), cefalotine (30 mkg), piperacillin (30 mkg), imipenem (10 mkg), ciprofloxacin (5 mkg), tobramycin (10 mkg), gentamicin (10 mkg), tetracycline (30 mkg). The standardized nutritive medium Mueller-Hinton was used for testing. The boxes with bacteria and antibiotics were maintained at 37°C, for 24 hours, with a subsequent determination of the result of antibioticogram.

The acute toxicity research during the enteral administration of the Enoxil compound was made on mice and white rats. It was established that the 500, 1000 and 2000 mg/kg body weight doses do not provoke modifications in the animals behaviour and neither their death. The cronical toxicity was established by the administration of the Enoxil in 100 and 300 mg/kg body weight doses at the male rats during 30 days.

Data were statistically analysed using the soft package STATISTICA 7.

3. RESULTS AND DISCUSSIONS

During the research was established that the animals that took the 300 mg/kg dose were more adinamic and were dead in 5-21 days time, but those administrated the 100

mg/kg dose survived. At macroscopical examination of the internal organs were not attested any pathological modifications. After undertaken the cronical toxicity study was established that the Enoxil compound in the 100 mg/kg dose do not modify essentially the level of creatinin and cholesterol.

Investigations on the action of Enoxil compound on bacteria *E.coli*, *S.abony*, *S.aureus*, *P.vulgaris*, *P.aeruginosa* and the fungus *C.albicans* resulted in the determination of the MIC (**Figure 1(a)**) and the minimal bactericidal/fungicidal concentration (MBC/MFC) (**Figure 1(b)**). Thus, Enoxil presents antibacterial, as well as antifungal properties at relatively low concentrations. The minimal

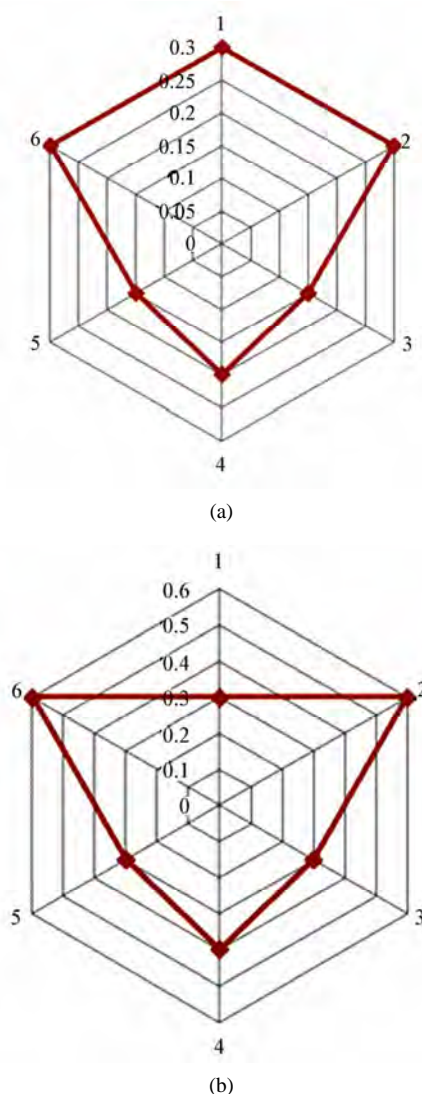


Figure 1. (a) Minimal inhibiting concentration and (b) Bactericidal/fungicidal of Enoxil for several microorganisms. On the hexagonal perimeter: 1–*E.coli*, 2–*S.abony*, 3–*S.aureus*, 4–*P.vulgaris*, 5–*P.aeruginosa*, 6–*C.albicans*. On the vertical—concentrations, %.

inhibiting concentration of Enoxil for the tested bacteria was shown to be in the range 0.15-0.3%, while the bactericidal one—in the range 0.3-0.6%. For the fungus *C.albicans* the minimal inhibiting concentration equals to 0.3%, while the fungicidal one—to 0.6%.

The values MIC and MBC/MFC for the microorganisms taken into the study presented differences of an order of magnitude, except for the *E.coli* bacteria, when these indexes coincided. As a result of the correlation analysis, it was determined that the degree of dependence (r) between MIC and MBC/MFC is significant and positive, equal to 0.66. Regression analysis, which has a predictive value and represents the mathematical relation of the dependence, demonstrated that its equation is: $y = 0.0923 + 0.3385 x$ ($p \leq 0.05$).

Data presented in **Table 1** shows that under the action of Enoxil at the determined static concentration (0.15%) took place the suppression of activities of oxidases, citrate reductases and haemolysin. At the same time, the bacterial culture didn't produce any pyocyanin and indole, and it didn't develop any specific odours. In these conditions, the maintenance of the mobility is a proof of bacteria viability, which reveals the correctness of the test. Thus, the static concentration of Enoxil produces significant perturbations at the biochemical level inside the bacterial cell, which probably significantly diminishes the capacity of substrates decomposition, as well as its pathogenic potential.

Treatment of the bacterial culture with Enoxil in-

creased the sensitivity (S) for the majority of investigated antibiotics, with manifested resistance (R) only for erythromycin and cefalotine (**Table 2**).

In the case of tetracycline, a reaction of medium sensitivity was observed (RS). In the case of blank, the culture manifested sensitivity only for pefloxacin and imipenem, while in the case of using Enoxil, the sensitivity was exhibited towards the majority of antibiotics, except for erythromycin and cefalotine. It should be mentioned that Enoxil introduced sensitivity into the bacteria towards several antibiotics considered inactive for *P.aeruginosa*, for example cefoxitin. The analysis of the similitude degree of the compounds using the clusterian method of dendrograms construction, demonstrated that the tested antibiotics were distributed in big clusters (**Figure 2(a)**), quite different, which reveals that

Table 1. Influence of the static concentration of Enoxil on several biochemical and functional indices of the *P.aeruginosa* bacterium.

Indicator	Blank (+/-)	Enoxil (+/-)
Oxidase	+	-
Citrate reductase	+	-
Haemolysin	+	-
Indole	-	-
Pyocyanin	+	-
Odour	+	-
Mobility	+	+

Table 2. Influence of the static concentration of Enoxil on the sensibility of the culture *P. aeruginosa* towards several antibiotics.

Nr.	Antibiotic	Untreated culture (blank)		Treated culture	
		Inhibition zone, mm	Reaction	Inhibition zone, mm	Reaction
1	Cloramfenicol	0.0	R	26.0 ± 0.6*	S
2	Pefloxacin	14.0 ± 0.6	R	26.3 ± 0.3*	S
3	Erythromycin	0.0	R	13.0 ± 0.6*	R
4	Cefuroxim	0.0	R	20.0 ± 1.2*	S
5	Cefoxitin	0.0	R	22.0 ± 0.6*	S
6	Cefalotine	0.0	R	0.0	R
7	Piperacillin	0.0	R	20.0 ± 1.2*	S
8	Imipenem	30.0 ± 1.2	S	29.3 ± 1.5*	S
9	Ciprofloxacin	0.0	R	24.0 ± 0.6*	S
10	Tobramycin	0.0	R	17.0 ± 1.2*	S
11	Gentamicin	0.0	R	16.0 ± 0.6*	S
12	Tetracycline	0.0	R	19.0 ± 0.7*	R-S

* - difference from the blank with statistic support at $p < 0.05$.

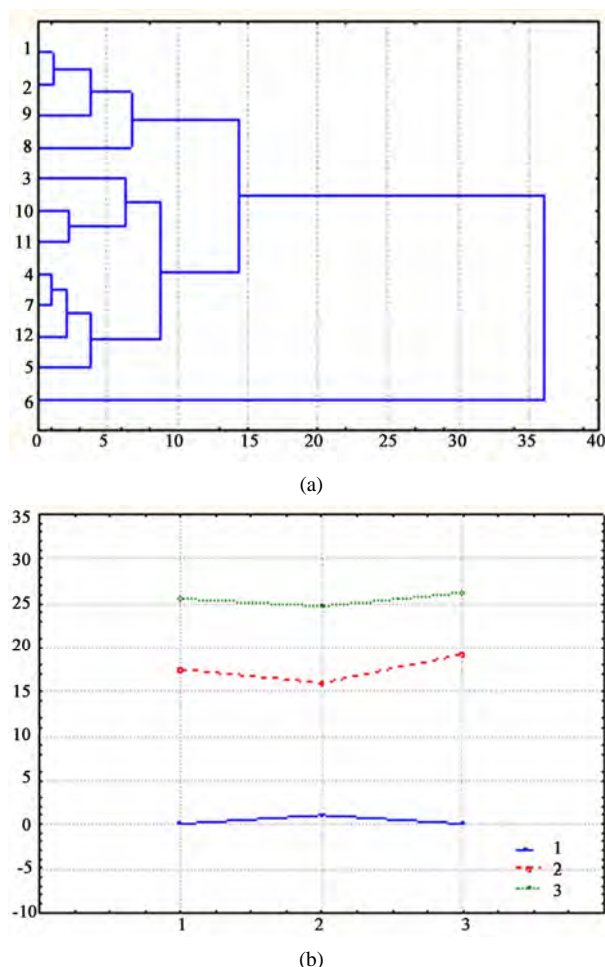


Figure 2. Clusterian analysis ((a)–construction of the dendrogram; (b)–method of k-means) of antibiotics on the basis of the capacity of suppression of *p.aeruginosa* strain treated with enoxil (0.2%). (a) on the vertical: 1–cloramfenicol, 2–pefloxaciline, 3–erythromycin, 4–cefuroxim, 5–cefoxitin, 6–cefalotine, 7–piperacillin, 8–imipenem, 9–ciprofloxacin, 10–tobramycin, 11–gentamicin, 12–tetracycline. on the horizontal: 0–40–euclidian distances. (b) on the vertical: 1, 2, 3–clusters of antibiotics. On the horizontal: 1, 2, 3–repeats.

the bacterial stem treated with Enoxil has different reaction towards antibiotics. A significantly different cluster was presented by the compound 6 – cefalotine (one of the most efficient antibiotics in pseudomonadic infections), for which the stem manifested the greatest resistance (inhibition zone: 0.0 mm). The lowest is the aggregation degree of clusters, the greatest is antibiotics similitude, on the basis of the inhibition zone (for example, cloramfenicol–1 and pefloxaciline–2). As opposed to the method of dendrograms construction, which is an agglomeration-iterative method and performs objects classification (antibiotics) on the basis of various aggregation levels, the method k-means of clusterian analysis,

non-iterative, classifies objects in clusters, determined by the researcher, on the basis of possible effects: low, medium, high, etc. and presents opportunities of high precision [23].

The classification (repartition) of antibiotics on the basis of the action on the *P.aeruginosa* strain, treated with Enoxil evidenced the existence of clusters with pronounced differences (**Figure 2(b)**). Through the examination of members (antibiotics) of the 3 clusters, it was determined that cluster 1 was formed by cefalotine alone, for which *P.aeruginosa* manifested the highest resistance, which was confirmed by the analysis of the repartition dendrogram. The cluster 2, where the antibiotics erythromycin, cefuroxim, piperacillin, tobramycin, gentamicin, tetracycline were distributed, is characterized by their capacity to produce a reaction of medium sensibility, while the cluster 3 – antibiotics cloramfenicol, pefloxaciline, cefoxitin, imipenem, ciprofloxacin – a reaction of strong sensibility.

Thus, if we make abstraction of the antibiotic imipenem, for which the strain presented sensibility in the blank as well, it may be observed that Enoxil induced a reaction of strong sensibility for the majority of antibiotics, among which 3 antibiotics – cloramfenicol, pefloxaciline and cefalotine are not used for the treatment of pseudomonadic infections [24], *i.e.* are non-specific.

4. CONCLUSIONS

The values MIC and MBC/MFC of Enoxil for the investigated microorganisms presented differences of an order of magnitude, except for the bacterium *E.coli*, for which these indices coincided. It was found that there is a high and positive correlation for MIC/MBC during treatment with Enoxil, which makes microorganisms behaviour predictive.

On the model of the *P.aeruginosa* bacteria it was determined that several of the biochemical mechanisms of suppression of growth and development by Enoxil consist in the inhibition of synthesis of such enzymes, important for the bacterial organism viability, as oxidases, citrate reductases, haemolysins, as well as pyocyanin. This phenomenon influenced most directly the sensibility of the bacteria towards a series of antibiotics used in modern medicine. The compound Enoxil in bactericidal concentrations (MBC–0.3%) may be considered of great potential in the treatment of pseudomonadic infections.

5. ACKNOWLEDGEMENTS

The authors are very grateful to Prof. V. Gonciar from the Department of Pharmacology from the State University of Medicine and Pharmacy “N.Testemitanu” who carried out the research on the toxicity of the Enoxil compound.

REFERENCES

- [1] Dogra, S. and Kumar, B. (2003) Epidemiology of skin diseases in school children: A study from Northern India. *Pediatric Dermatology*, **20**(6), 470-473.
- [2] Collier, M. (2002) Wound-bed management: Key principles for practice. *Professional Nurse*, **18**(4), 221-225.
- [3] Cooper, R. (2002) Wound microbiology: Past, present, and future. *British Journal of Nursing*, **11**(22), 4-6.
- [4] Miller, M. (2001) Wound infection unravelled. *Journal of Community Nursing*, **15**(3), 31-33.
- [5] Nosocomial Infection National Surveillance Service (2002) Surveillance of surgical site infection in English hospitals: A national surveillance and quality improvement programme. Health Protection Agency, London.
- [6] Singh, N.P., Goyal, R., Manchanda, V., *et al.* (2003) Changing trends in bacteriology of burns in the burns unit. *Burns*, **29**(2), 129-132.
- [7] Prisacari, V. and Paraschiv, A. (2008) Contributions in the epidemiological surveillance systems optimization within nosocomial septico-purulent infections of surgical profile. *Epidemiology and Microbiology. Mat. Congress VI of Hygienists, Epidemiologists and Microbiologists from the Republic of Moldova*, Chișinău, **2**, 22-25.
- [8] Rodgers, G., Mortensen, J., Fisher, M., *et al.* (2000) Predictors of infectious complications after burn injuries in children. *Pediatric Infectious Disease Journal*, **19**(10), 990-995.
- [9] Gang, R.K., Bang, R.L., Sanyal, S.C., *et al.* (1999) Pseudomonas aeruginosa septicaemia in burns. *Burns*, **25**(7), 611-616.
- [10] Kehheth, T. (2008) Pseudomonas aeruginosa. <http://www.textbookofbacteriology.net/pseudomonas.html>
- [11] Rozhavin, M.A. (1983) Some biological properties of the *P.aeruginosa* melanin. *Journal of Microbiology*, in Russian, **1**, 45-47.
- [12] Valencia, I., Kirsner, R. and Kerdel, F. (2004) Microbiologic evaluation of skin wounds: Alarming trend toward antibiotic resistance in an inpatient dermatology service during a 10-year period. *Journal of the American Academy of Dermatology*, **50**(6), 845-849.
- [13] Visnevchi, L. and Bradu, V. (2008) Antibiotical microorganisms resistance modification, tested in the microbiological laboratory of PRMC Ungheni. *Epidemiology and Microbiology. Mat. Congress VI of Hygienists, Epidemiologists and Microbiologists from the Republic of Moldova*, Chișinău, **2**, 264-265.
- [14] Schwaber, M.J., Cosgrove, S.E., Gold, H.S., *et al.* (2004) Fluoroquinolones protective against cephalosporin resistance in gram-negative nosocomial pathogens. <http://www.medscape.com/viewarticle/466484>
- [15] Asres, K., Mazumder, A. and Bucar, F. (2006) Antibacterial and antifungal activities of extracts of combretum molle. *Ethiopian Medical Journal*, **44**(3), 269-277.
- [16] Santos, S.C. and Mello, J.C.P. (2004) Taninos. *Farmacognosia da Planta ao Medicamento*, in Portuguese, 5th Edition, Porto Alegre, Florianópolis, 615-656.
- [17] Timbola, A.K., Szpoganicz, B., Branco, A., *et al.* (2002) A new flavonol from leaves of *Eugenia jambolana*. *Fitoterapia*, **73**(2), 174-176.
- [18] Chung, K., Lu, Z. and Chou, M. (1998) Mechanism of inhibition of tannic acid and related compounds on the growth of intestinal bacteria. *Food and Chemical Toxicology*, **36**(12), 1053-1060.
- [19] Kulcički, V., Vlad, P., Duca, G., *et al.* (2007) Investigation of grape seed proanthocyanidins. *Chemistry Journal of Moldova*, **2**(1), 36-50.
- [20] Lupășcu, T. and Lupășcu, L. (2006) The obtaining procedure of the watersoluble enotannins. Patent Nr. 3125. MD. BOPI: 8.
- [21] Andrews, J.M. (2001) Determination of minimum inhibitory concentrations. *Journal of Antimicrobial Chemotherapy*, **48**(1), 5-16.
- [22] National Committee for Clinical Laboratory Standards (NCCLS) (2002) Performance standards for antimicrobial susceptibility testing. 12th Informational Supplement M100-S12 NCCLS, Wayne.
- [23] Halafian, A.A. (2008) Modern statistical methods of medical research. In Russian, LKI Publishers, Moscow.
- [24] Matcovschi, C., Procopisin, V. and Pării, B. (2006) Pharmacotherapeutical guide. Central Printing, Chișinău.

MRI monitoring of lesions created at temperature below the boiling point and of lesions created above the boiling point using high intensity focused ultrasound*

Christakis Damianou^{1,2}, Kleanthis Ioannides³, Venediktos Hadjisavvas⁴, Nikos Mylonas⁴,
Andreas Couppis⁴, Demetris Iosif¹, Panayiotis A. Kyriacou⁴

¹Frederick University Cyprus, Limassol, Cyprus;

²MEDSONIC LTD, Limassol, Cyprus;

³Polikliniki Ygia, Limassol, Cyprus;

⁴City University, London, UK.

Email: cdamianou@cytanet.com.cy

Received 11 April 2010; revised 26 May 2010; accepted 31 May 2010.

ABSTRACT

Magnetic Resonance Imaging (MRI) was utilized to monitor lesions created at temperature below the boiling point and lesions created at temperature above the boiling point using High Intensity Focused Ultrasound (HIFU) in freshly excised kidney, liver and brain and *in vivo* rabbit kidney and brain. T2-weighted fast spin echo (FSE) was proven as an excellent MRI sequence that can detect lesions with temperature above the boiling point in kidney. This advantage is attributed to the significant difference in signal intensity between the cavity and the thermal lesion. In liver the MRI sequence of Proton Density is recommended to detect lesions above boiling. In brain T1-W FSE was the optimum pulse sequence to detect lesions of either type. In order to monitor the temperature elevation during a HIFU exposure, T1-weighted fast spoiled gradient (FSPGR) was used. The shape of the focal temperature distribution was uniform with the absence of boiling, whereas with an exposure affected by boiling, the temperature distribution could be of irregular shape, demonstrating the drastic effects taking place during boiling. In order to confirm that boiling occurred, the temperature was estimated using the widely used method of Proton Resonance Frequency (PRF) shift.

Keywords: Ultrasound; Kidney; Brain; Liver; MRI; Lesion

1. INTRODUCTION

This paper is a continuation of previous papers by Damia-

nou [1] and Damianou *et al.* [2]. The first paper describes methods for ablating kidney tissue using high intensity focused ultrasound (HIFU), whereas the second paper deals with magnetic resonance imaging (MRI) guidance of HIFU for the case of kidney. This paper goes one step further by evaluating lesions created at temperatures above the boiling point during HIFU exposures using MRI. The evaluation was performed in kidney, liver and brain.

We have chosen to explore kidney, liver and brain because there is currently a lot of ongoing research either in animal models or in humans for these 3 tissues. In the area of kidney ablation with HIFU Watkin *et al.* [3] used a large animal model and proved the feasibility of this treatment method. Recently Roberts *et al.* [4] have performed ablations in the normal rabbit kidneys and they suggested that the mechanical effects of ultrasound, can be used to homogenize tissue.

HIFU ablation of renal tumours in humans remains in the early stages of clinical trials. In the early 1990s, Valancien *et al.* [5] reported the first clinical feasibility study in kidney using extracorporeal HIFU. Susani *et al.* [6], Wu *et al.* [7], and Marberger *et al.* [8] conducted clinical trials in patients with renal tumours and proved that HIFU may have a place in the treatment of renal tumours.

Hacker *et al.* [9] performed also ablation of 43 kidneys (porcine and human), using an experimental handheld extracorporeal technology. Finally Klingler *et al.* [10] use laparoscopic methods to treat kidney tumors.

Small animal models [11,12] were used to establish the feasibility of HIFU to create lesions in liver tissue. The thresholds for liver tissue destruction at varying exposure parameters were established in the 70s and 80s [13].

*This work was supported by the Research Promotion Foundation (RPF) of Cyprus under the contract ERYAN/2004/1, ANABA ΘΜΙΣΗ/ ΠΑΓΙΟ/0308/05, and ΕΠΙΧΕΙΡΗΣΕΙΣ/ ΕΦΑΡΜ /0308/01.

Basic research in the area of liver continued during the 1990s; for example the histological effects of HIFU [14], the effects of blood perfusion on during liver ablation [15], and the relationship between tissue depth and the required intensity levels [16].

Several tumour models have been used to predict the effects of HIFU on liver tumors in humans (for example [17,18]) and to destroy VX2 liver tumours in rabbits [19, 20]. Hooded Sarcoma N (HSN) fibrosarcoma has been also used as a tumour model in rats with some success [21]. HIFU was also used for the treatment of metastatic melanoma in liver in a cat [22].

There is an increasing interest of work describing HIFU in the treatment of liver cancer in human clinical trials. In the early 1990s, Vallancien *et al.* [23] reported treatment of liver metastases using HIFU.

The Chongqing group published a study [24] describing a clinical trial of 68 patients with liver malignancies using HIFU. Li *et al.* [25] reported clinical trial of patients with liver cancer who were treated also with HIFU. Wu *et al.* [26] use HIFU in combination with TACE for the treatment of HCC.

MRI-guided HIFU has generally been used for the treatment of uterine fibroids using the ExAblate 2000 system (InSightec, Haifa, Israel). However, it is very likely that soon this system will be utilized for the treatment of kidney, liver and brain tumours. At Imperial College, London they have recently started a non-randomised clinical trial to assess the safety and efficacy of the MRI-guided HIFU system of InSightec in the treatment of liver tumours [27].

Thermal ablation of brain in animals with high intensity focused ultrasound (HIFU) was very popular in the 50's and 60's (for example [28] and [29]). HIFU was used in the clinical setting by Fry and Johnson [30] and showed that HIFU had the potential to treat brain cancer. Several groups used hyperthermia (heating of several minutes at 43°C) to treat brain tumours [31,32]. The clinical trials were abandoned probably due to the inexistence of effective imaging modality to guide the therapy. Especially for the case of brain it is extremely important to have absolute control of the ablation in order to avoid vital brain tissue damage such as the neurons. Now with the advancement of HIFU technology guided by MRI, it will be possible to conduct clinical studies for brain cancer.

In the early nineties several studies by the group of Dr. Hynynen [33-38] demonstrated the creation of lesions in animal brain and use MRI successfully for guiding and monitoring. Therefore, now there is increasing interest regarding brain ablation.

The combination of HIFU and MRI was first cited by

Jolesz and Jakab [39] who demonstrated that an ultrasonic transducer could be used inside a MRI scanner. The concept of using MRI to monitor the necrosis produced by HIFU was fully demonstrated in the early nineties in canine muscle [40-42]. In these studies it was shown that the contrast between necrotic tissue and normal tissue was excellent. This was a great enhancement for the HIFU systems because the therapeutic protocols can be accurately guided. Therefore the interest of using MRI as the diagnostic modality of guiding HIFU was increased. Although there are numerous studies regarding lesions created with temperature below the boiling point (also known as thermal lesions), there is insufficient information regarding MRI detection of lesions created with temperature above the boiling point. This paper focuses in the detection of lesions above boiling using MRI.

Several MRI sequences are investigated. For high quality imaging, this can be used at the end of a therapeutic protocol or at some instances of the protocol, the fast spin echo (FSE) techniques T1, and T2-weighted are investigated in all 3 tissues under investigation. For fast imaging, the T1-weighted fast spoiled gradient (FSPGR) MRI sequence was used. Fast imaging can be used to monitor the dynamic increase of tissue temperature during the application of an ultrasonic exposure. We have also use the fluid-attenuated inversion recovery (FLAIR) sequence for brain since this is the predominant sequence used in the clinical setting.

In order to prove whether a lesion is created at temperature below boiling or above, it is necessary to estimate the temperature at the focus. The proton resonance frequency (PRF) shift has been proven to be best pulse sequence for estimating temperature, because with this sequence the temperature is less dependent on the physiological changes of tissue during high-temperature HIFU exposures [43]. The temperature dependence of the PRF shift was measured to be linear above 50°C [43]. This linearity of the PRF shift above the tissue necrosis threshold allows the tissue temperature to be estimated during the therapeutic ultrasound exposures.

The task with high quality imaging was to find an optimum technique that can discriminate thermal from boiling lesions. Discriminating between lesion and normal tissue involves two types of tissues. Discriminating between thermal and boiling lesions involves three types of layers (normal tissue, lesion and cavity). Therefore the signal intensity vs. MR parameters needs to be evaluated for the above layers in order to optimise the contrast among tissue of interest, lesion and cavity. The other main task was to monitor the temperature elevation using a fast MRI technique in order to observe the shape

of the beam during HIFU exposures.

The growth of vapor bubbles due to boiling occurs due to the temperature induced by HIFU. Boiling is different from cavitation which occurs due to pressure oscillations induced by HIFU. Vapor bubbles created by boiling can grow rapidly to a size of few millimetres [44]. This growth can be explosive due to the super heating caused by HIFU. Therefore the cavities produced of few mms can be easily monitored by MRI.

There are two reasons for studying the MRI appearance of boiling lesions that could be of importance:

1) Since boiling provides enhanced heating, it could be possible for large tumours (for example giant fibroadenomas) to use this type of heating (especially in the center of the tumor) in order to accelerate the ablation,

2) since the rabbit model is used extensively by many researchers in MRI animal experiments (for example [33-37]), then it is very useful for them to know the appearance of boiling lesions.

2. MATERIALS AND METHODS

2.1. HIFU/MRI System

Figure 1 shows the block diagram of the HIFU/MRI system which includes the following subsystems:

1) HIFU system, 2) MR imaging, 3) Positioning device (robot) and associate drivers, 4) Temperature measurement, 5) Cavitation detection, 6) MRI compatible camera, 7) Software.

2.1.1. HIFU System

The HIFU system consists of a signal generator (HP 33120A, Agilent technologies, Englewood, CO, USA), a RF amplifier (250 W, AR, Souderton, PA, USA), and a spherically shaped bowl transducer made from piezoelectric ceramic of low magnetic susceptibility (Etalon, Lebanon, IN, USA). The transducer used for the kidney and liver ablation operates with frequency of 4 MHz, and the transducer for brain ablation operates at 1 MHz. The transducer is rigidly mounted on the MRI-compatible positioning system (MEDSONIC LTD, Limassol, Cyprus) which is described shortly.

2.1.2. MRI Imaging

The 3-d positioning device and the transducer were placed inside a MRI scanner (Signa 1.5 T, by General Electric, Fairfield, CT, USA). The spinal coil (USA instruments, Cleveland, OH, USA) was used to acquire the MRI signal for the case of kidney and liver, whereas a brain coil (USA instruments, Cleveland, OH, USA) was used to acquire the MRI signal from the brain tissue.

2.1.3. Positioning Device/Drivers

The robot has been developed initially for three de-

grees-of-freedom, but it can be easily developed for 5 degrees of motion. Since the positioning device is placed on the table of the MRI scanner its height should be around 55 cm (bore diameter of the MRI scanner). The length of the positioning device is 45 cm and its width 30 cm. The weight of the positioning device is only 6 kg and therefore it can be considered portable. **Figure 2** shows the schematic the positioning device illustrating the 3 stages, transducer, and coupling method. The positioning device operates by means of 3 piezoelectric motors (USR60-S3N, Shinsei Kogyo Corp., Tokyo, Japan). More details of this positioning device can be found in [31]. The movement of the positioning device is monitored by an MRI compatible camera (not shown in the figure) which is placed on a non-magnetic holder. Moreover, the positioning system includes optoelectronic encoders for providing signals indicating the relative positions of the movable elements in the positioning system. The resolution of all 3 axes of the positioning device is 0.1 mm.

2.1.4. MRI Compatible Camera

In order to monitor the condition of the animal or humans

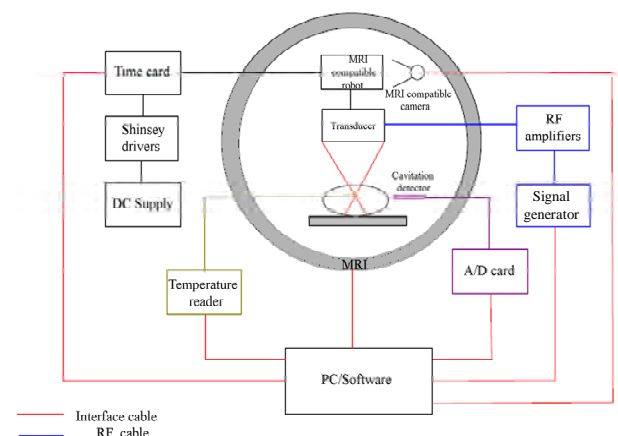


Figure 1. HIFU system under MRI guidance showing the various functionalities of the HIFU/MRI system.

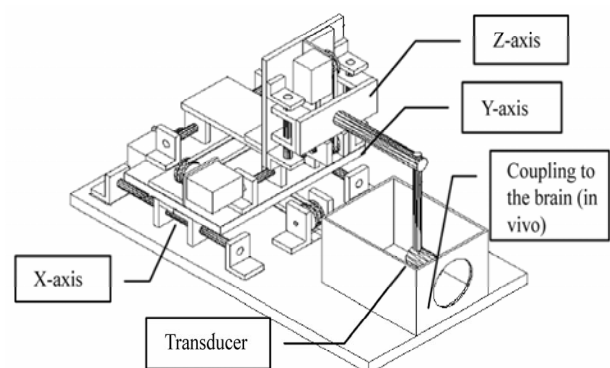


Figure 2. Schematic of the robot showing all of its stages.

(future use), a MRI compatible camera (MRC Systems GmbH, Heidelberg, Germany) was mounted on the system. The camera was interfaced by means of a video card. With the aid of the MRI compatible camera, the researcher can monitor the welfare of the animal.

2.1.5. Temperature Measurement

Temperature was measured in few experiments in order to confirm that the temperature estimated using the PRF method was accurate enough. Temperature is measured using a data acquisition system (HP 34970A, Agilent technologies, Englewood, CO, USA). Temperature is sensed using a 50- μ m diameter T-type copper-constantan thermocouple (Physitemp Instruments, Inc. New Jersey, USA) which is MRI compatible. The thermocouple is placed in the tissue by means of a catheter. The thermocouple measures the temperature at the focus. This is achieved by applying low-intensity (low enough not to cause tissue damage) and during the application of ultrasound the transducer is scanned accordingly in order to detect the maximum temperature. This establishes positioning of the thermocouple in the focus of the transducer. The temperature error of the thermocouple is in the order of 0.1°C.

2.1.6. Cavitation Detector

From a scientific point of view it will be useful to separate lesions developed based on thermal and based on cavitation mechanisms. In this system we use a passive MRI compatible cavitation detector (Etalon, Lebanon, IN, USA), which is placed perpendicularly to the beam of the HIFU transducer (method described in [45]). Since the HIFU protocol is applied inside the magnet of an MRI scanner, the detector must be MRI compatible. The diameter of the detector was 1 cm, its radius of curvature was 10 cm and operated between 1 and 13 MHz (centre frequency is 7 MHz). The detector was mechanically coupled to the HIFU transducer. The voltage from the detector was fed to an analogue to digital (A/D) card (CS1250, A/D 12 bit, 50 MHz, from GAGE, Lachine, Canada). The A/D card was synchronised to receive the signal when the HIFU transducer was activated. The received signal was stored in a PC (Dell Inc. Round Rock, Texas, USA). The signal was then displayed using EXCEL (Microsoft Corporation, Redmond, WA USA) in order to visualize whether cavitation occurs or not.

2.1.7. Software

A user-friendly program written in MATLAB (The Mathworks Inc., Natick, MA) has been developed in order to control the system. The software serves the following main tasks: 1) Displaying of MR images, 2) transducer movement (the user may move the robotic arm in a specific direction or customize the automatic movement of the robotic arm in any rectangular forma-

tion by specifying the pattern, the step and the number of steps), 3) messaging (starting time, treatment time left etc), 4) Patient data (age, weight, etc), 5) Display of motor position, and 6) Display of the contents of an MR compatible camera, 7) Cavitation detection window, 8) temperature measurement, and 9) MR estimated temperature using the PRF method.

2.2. *In Vitro* Experiments

The tissue was placed on top of an absorbing material in order to shield adjacent tissue from stray radiation from the bottom. The transducer was placed on the arm of the positioning device and was immersed in the water tank, thus providing good acoustical coupling between tissue and transducer. Any bubbles that may have collected under the face of the transducer face were removed in order to eliminate any reflections. In all experiments the tissues used (kidney, liver and brain) were extracted from freshly killed lamb, and the experiment was conducted in the same day. Totally 22 kidneys, 8 liver and 16 brains were ablated for investigating various issues.

2.3. *In Vivo* Experiments

For the *in vivo* experiments, adult rabbits from Cyprus were used weighting approximately 3.5-4 kg. Totally 8 rabbits were used in the experiments. The rabbits were anaesthetized using a mixture of 500 mg of ketamine (100 mg/mL, Aveco, Ford Dodge, IA), 160 mg of xylazine (20 mg/mL, Loyd Laboratories, Shenandoah, IA), and 20 mg of acepromazine (10 mg/mL, Aveco, Ford Dodge, IA) at a dose of 1 mL/kg.

Presence of the skull in the ultrasonic path not only distorts the field by reflection, but may also destroys the underlying tissue in contact with it by absorbing ultrasonic energy and dissipating it as heat. A craniotomy adequate in extent to permit unimpeded passage of the cone of sound was imperative. The extent of the craniotomy depends on the solid angle of radiation and the depth of the target from the cranial surface. The larger the angle and the deeper the target, the larger the size of craniotomy needed. For the transducer used and a target depth of 1 cm, a circular craniotomy of 3 cm in diameter was adequate. The animal experiments protocol was approved by the national body in Cyprus responsible for animal studies (Ministry of Agriculture, Animal Services).

2.4. HIFU Parameters

The *in situ* spatial average intensity was estimated based on the applied power and the half-power width of the beam of the transducer. The details of the intensity estimation can be found in Damianou 2003 [1]. In order to create large lesions, a grid pattern of 3×3 or 4×4 over-

lapping lesions was used. The spacing between successive transducer movements was 2 mm, which creates overlapping lesions for the intensity and pulse duration used. In all the exposure, unless stated otherwise the ultrasound was turn on for 5 s. The delay between successive ultrasound firings was 10 s for the scanned ablation. The intensity indicated through this paper is in situ spatial average intensity.

2.5. MRI Parameters

The various MRI parameters used for the various pulse sequences are listed in **Table 1**. The Region of Interest (ROI) was circular with diameter of nearly 2 mm.

The temperature change (T) has been estimated using the equation stated in Chung *et al.* 1996 [46] which is as follows:

$$\Delta\phi = \gamma B_0 \alpha \Delta T T E \quad (1)$$

where $\Delta\phi$ is the temperature-dependent phase shift which is the phase acquired before and during temperature elevation and which accumulates during the echo time TE using the gradient-echo pulse sequence FSPGR. The other terms are γ which is the gyromagnetic ratio of proton, 42.58 MHz/T, α is the average proton resonance frequency coefficient and B_0 is the flux density of the static magnetic field. The measured temperature elevation can be added to the base-line temperature to obtain the absolute temperature. The average temperature coefficient for the frequency shift was taken from the study of Vykhodtseva *et al.* [47].

3. RESULTS

Figure 3 shows an MRI image of 4 lesions *in vitro* kidney (plane perpendicular to the beam) resulting from intensities ranging from 1000 to 2500 W/cm² using T1-weighted FSE (**Figure 3(a)**), T2-weighted FSE (**Figure 3(b)**) and T1-weighted FSPGR (**Figure 3(c)**) with pulse duration of 5 s. The MRI parameters used are shown in **Table 1** (row 1, 2 and 4). The MRI estimated maximum temperature at the focus was 55°C for the intensity of 1000 W/cm², 83°C for 1500 W/cm², 105°C for 2000 W/cm² and 123°C for 2500 W/cm². The

temperature measured using the thermocouple for the 1000 W/cm² was 53°C, which is very close to the temperature estimated using the PRF method.

Note that with T2-weighted FSE (**Figure 3(b)**) white spots (cavity) within the dark thermal lesion are seen for intensities higher than 2000 W/cm². T1-W FSE and FSPGR show some indication of these cavities, but the resolution is weaker than T2-w FSE.

Figure 4 shows MRI images (in a plane parallel to the transducer beam) of 3 lesions in kidney *in vitro* at intensities of 1000, 2000 and 3000 W/cm². Again T2-weighted FSE shows cavities (due to boiling) within the thermal lesion. T1-W FSE and T1-W FSPGR fail to provide good resolution in this axis.

Having observed that T2-W FSE was probably a successful MRI sequence to detect boiling lesions, this pulse sequence was investigated further by evaluating the Contrast to Noise Ratio (CNR) vs. Echo Time (TE). **Figure 5** shows the plot of CNR vs. TE for kidney tissue, lesion and cavity of the lesion of **Figure 4(b)** (intensity of 3000 W/cm²) demonstrating that good contrast between lesion and cavity is achieved using T2-weighted FSE between 20 and 50 ms.

Figure 6 shows a T2-weighted FSE image of 3 lesions in rabbit kidney *in vivo* using different intensities (1000, 2000 and 2500 W/cm²) for a 5 s pulse. The estimated temperature was 52°C, 95°C and 115°C.

The lesion created using 2500 W/cm² appears to have a white spot (cavity). These temperatures are lower than the corresponding temperatures *in vitro* (**Figure 4**) for the same intensity due to the removal of heat due to blood flow or possibly due to reflection from various interfaces.

Figure 7(a) shows an MR image of a lesion acquired using T1-weighted FSPGR (for MRI parameters see **Table 1**, row 4). **Figure 7(b)** shows the photograph of the kidney showing cavity within the large thermal lesion.

Note that this large lesion was created using a matrix of 4 × 4 single lesions with intensity of 1500 W/cm². Out of these 16 lesions, one lesion was created possibly due to the mechanism of cavitation, which results to tissue evaporation or boiling. The estimated temperature during

Table 1. Parameters used for the various MRI pulse sequences.

Series	NAME	TR (ms)	TE (ms)	Slice thickness (mm)	Matrix	FOV (cm)	NEX	BW (KHz)	ETL	Other
1	T1-weighted FSE	500	9.2	3, (gap 0.3 mm)	256 × 256	16	1	31.25	8	-
2	T2-weighted FSE	2500	8,16,32,48,64,80	3, (gap 0.3 mm)	256 × 256	16	1	31.25	8	-
3	PD	2500	7.2	3, (gap 0.3 mm)	256 × 256	16	1	31.25	8	-
4	FSPGR T1-weighted	50	2.7	3, (gap 0.3 mm)	256 × 256	16	1	62.50	-	Flip angle 50
5	FLAIR	8000	80	3, (gap 0.3 mm)	256 × 256	16	1	6.9	8	Inversion Time 1200-2200

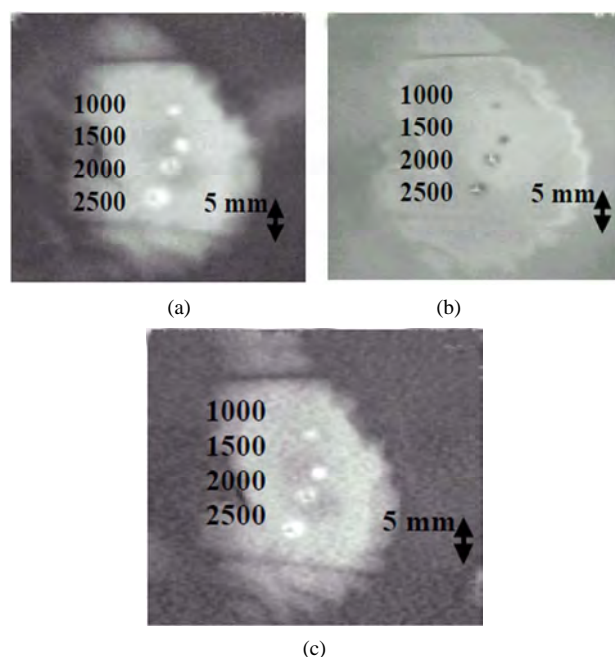


Figure 3. MR images (in a plane perpendicular to the beam) of four lesions (intensities 1000, 1500, 2000 and 2500 W/cm²) in kidney *in vitro* using. (a) T1-weighted FSE; (b) T2-weighted FSE; (c) T1-weighted FSPGR. With intensities above 2000 W/cm² the lesions exhibit boiling activity. The discrimination between boiling and non-boiling lesion is best monitored using T2-W FSE.

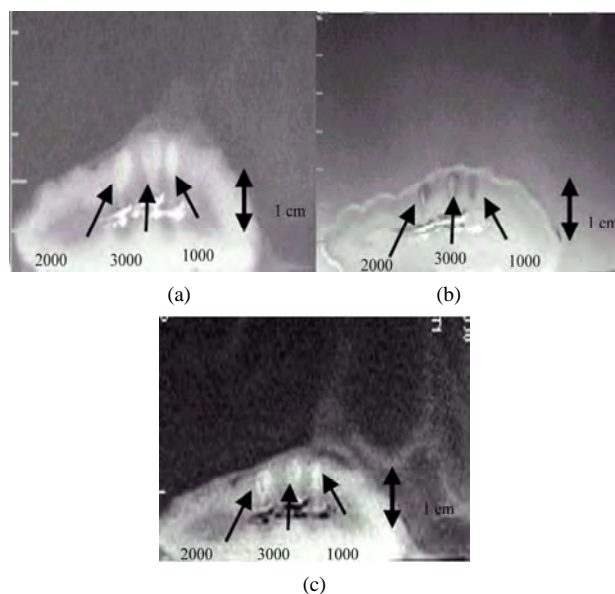


Figure 4. MR images (in a plane parallel to the beam) of 3 lesions in kidney *in vitro* using. (a) T1-weighted FSE; (b) T2-weighted FSE; (c) T1-weighted FSPGR. With intensities above 2000 W/cm² the lesions exhibit boiling activity. The discrimination between boiling and thermal lesion is best monitored using T2-W FSE.

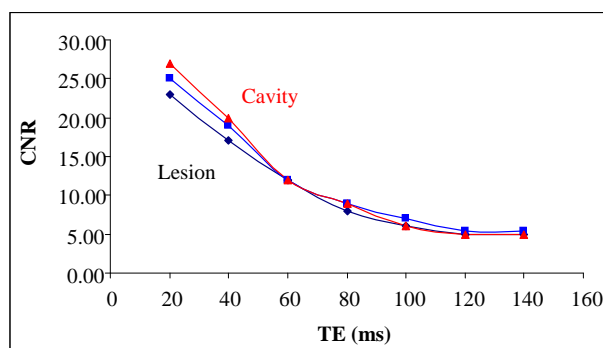


Figure 5. CNR vs. TE for the lesion, kidney and cavity for the lesion of **Figure 8(b)** with intensity of 3000 W/cm².

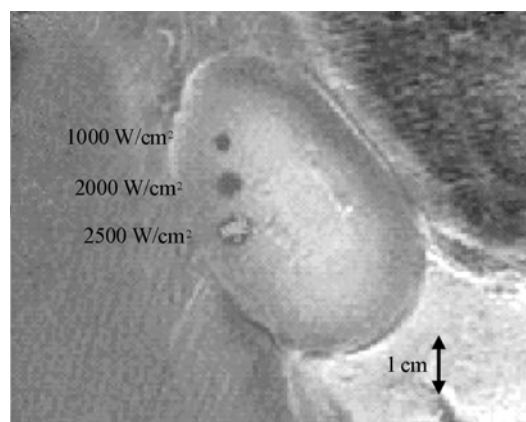


Figure 6. MRI image using T2-weighted FSE of 3 lesions in rabbit kidney *in vivo* at different intensities (1000, 2000, and 2500 W/cm²) for a 5 s pulse. The lesion with intensity of 2500 W/cm² is affected by tissue boiling.

the creation of this lesion was 120°C, whereas the temperature for the rest of the lesions (non-boiling) varied from 80 to 85°C.

This bubbly lesion exhibits low-signal lesion (dark spot) and lies inside the large lesion (white spot within the kidney tissue). At the location of the boiling lesion, the passive cavitation detector confirmed the occurrence of cavitation since broadband emission was detected (see **Figure 7(c)** which shows the frequency spectrum of the HIFU transducer). Although with this intensity bubbly lesions should not be produced, the high temperature estimated for this one lesion, should be attributed to cavitation. Cavitation was possibly initiated by bubbles that are trapped in the *in vitro* tissue due to the absence of blood in the vasculature.

Figure 8 demonstrates the temperature increase *in vitro* kidney using HIFU and MRI monitoring. The MRI images were acquired using the dynamic sequence T1-weighted FSPGR. Each image was acquired in 5 s. In **Figure 8(a)** ultrasound was OFF. In the next 5 images

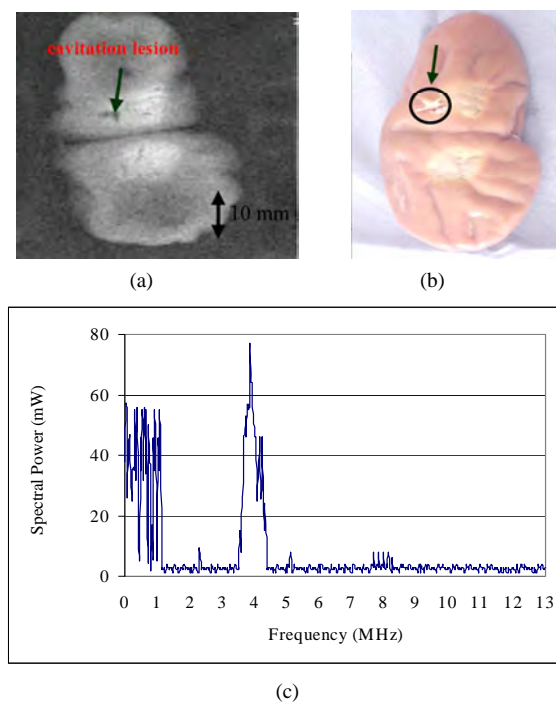


Figure 7. (a) MR image (in a plane perpendicular to the beam) of large lesion in kidney *in vitro* using T1-weighted FSPGR (TR = 50 ms), showing one cavitation lesion; (b) Photograph of the kidney showing the cavitation lesion within the large thermal lesion; (c) Frequency spectrum of the HIFU transducer exhibiting cavitation activity.

the applied spatial average intensity was 1000 W/cm^2 (for 25 s), and in the last 2 images ultrasound is turned OFF. Due to the heating a dark spot is observed (see arrows). The estimated maximum temperature was 55°C .

Figure 9 shows the corresponding temperature increase using T1-weighted FSPGR influenced by boiling. In **Figure 9(a)** ultrasound was OFF. In the next 5 images the applied spatial average intensity was 3500 W/cm^2 (for 25 s). Note that compared to **Figure 7** where the focal beam is circular, the focal beam in this figure is distorted, which is attributed to the occurrence of boiling confirmed also by the temperature of 112°C measured.

Figure 10 shows MRI image of lesion in liver. The image was acquired using Proton density. The lesion was created using low intensity (1000 W/cm^2) for long time (30 s). These ultrasonic parameters produce temperature elevation which is above the boiling point (120°C). Thus, the evaporation of tissue causes a cavity that follows the shape of the beam.

Figure 11 shows the MRI image a large lesion in lamb brain *in vitro* created by scanning the transducer with a 4×4 grid using 2000 W/cm^2 using T1-w FSE resulting to a large bubbly lesion. The maximum estimated temperature for this lesion was 110°C . Note that

in some location no lesion was created due to poor ultrasound penetration due to the air bubbles possibly trapped in the blood vessels. This image shows once more the excellent contrast between normal brain and lesions (in this case boiling lesions).

Figure 12 shows ablation in rabbit *in vivo* using a 4×4 grid with intensity of 2000 W/cm^2 for 20 s. This large lesion was created using thermal mechanisms and therefore the lesion appears bright. The maximum estimated temperature for this exposure was 90°C . The contrast of thermal lesions is definitely much better than the case of boiling lesions. Unlike the *in vitro* case of **Figure 11** where with this level of intensity boiling lesions were created, in this *in vivo* example in none of the 16 lesions a boiling lesion was produced. This proves that *in vitro* brain includes bubbles which are responsible for producing boiling lesions possibly due to enhanced heating or cavitation. Both of these mechanisms possibly produced temperatures above boiling and therefore bubbly lesions were created.

The methodology applied for kidney which evaluates T1-W FSE, T2-W FSE and FSPGR (**Figures 3 and 5**) was also applied for liver. In brain in addition to these 3 pulse sequences, FLAIR was also evaluated because this MRI sequence is widely used clinically for the case of brain. It was found that for liver the best pulse sequence to evaluate boiling lesions was T2-w FSE with minimum TE (*i.e.* proton density). For brain T1-W FSE was the best pulse sequence to monitor both boiling and non-boiling lesions. **Table 2** summarizes the recommended MRI sequence according to our experience for monitoring boiling lesions.

4. DISCUSSION

So far it was concluded by several studies (for example Quesson *et al.* [48], Salomir *et al.* [49], McDannold *et al.* [50]) that MRI-guidance of HIFU serves mainly 4 purposes: 1) localisation of the focus, 2) imaging of the temperature elevation, 3) imaging at the end of the treatment protocol, in order to evaluate the necrosis and

Table 2. Recommended pulse sequences for discriminating between (a) normal and thermal lesions; and (b) normal tissue, lesions created with temperature below boiling and lesions created with temperature above boiling.

Tissue type	Contrast between lesion below boiling and tissue	Contrast between lesion below boiling, tissue, and lesion above boiling
Kidney	T1-W FSE, T2-W FSE	T2-W FSE
Liver	T1-W FSE, T2-W FSE	T2-W FSE
Brain	T1-W FSE	T1-W FSE

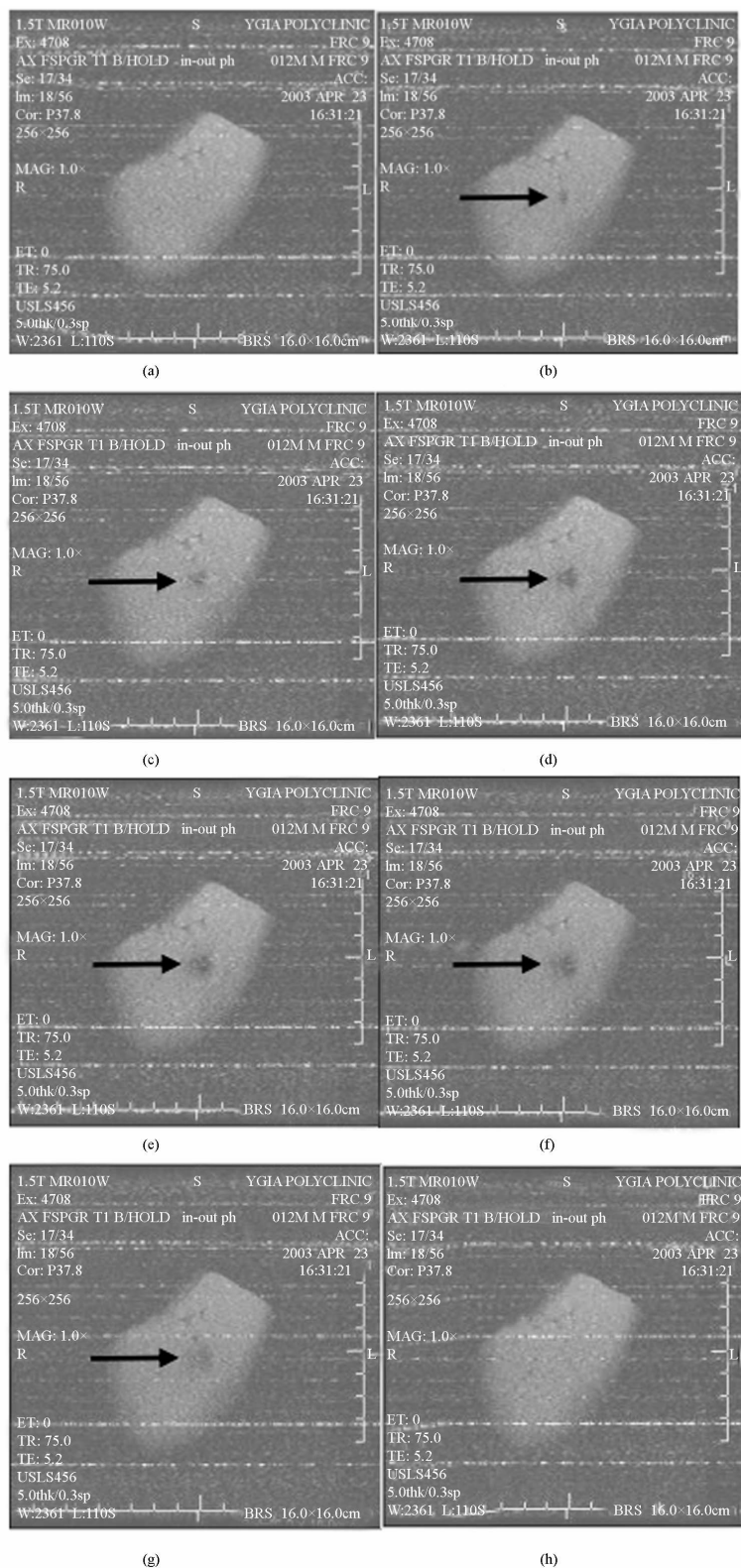


Figure 8. Temperature evolution *in vitro* kidney using T1- weighted FSPGR (thermal mechanism). Each image was acquired in 5 s. (a) Ultrasound is OFF; (b)-(f) Applied spatial average intensity: 1000 W/cm² (for 25 s); (g)-(h) Ultrasound is OFF.

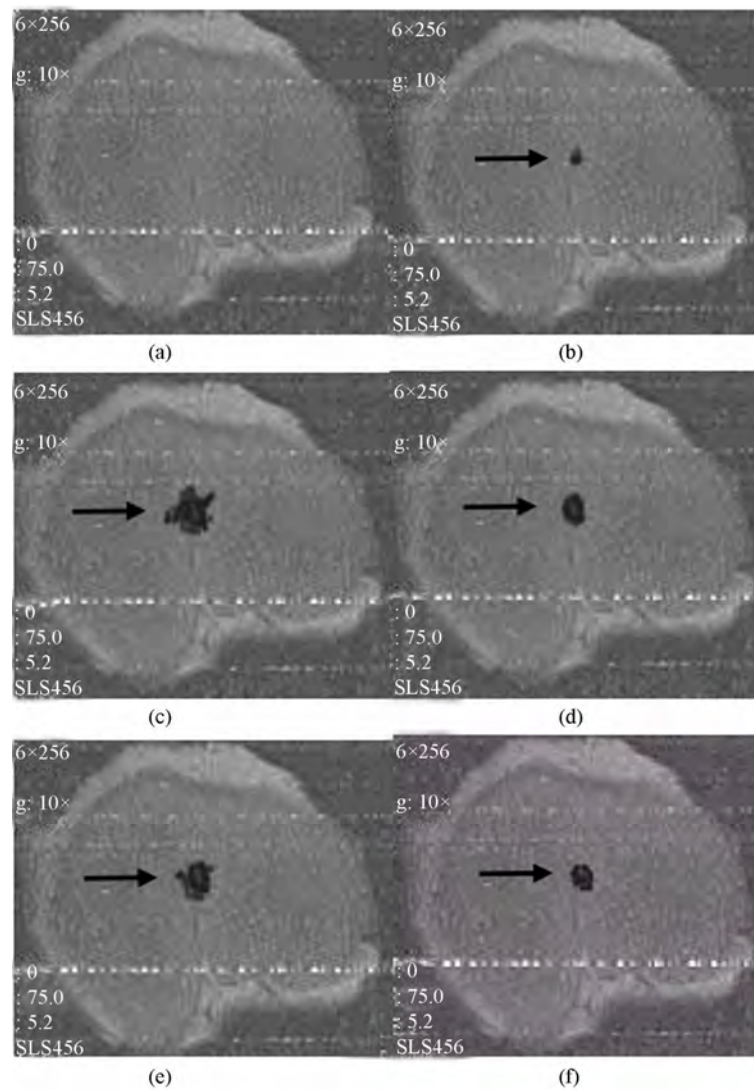


Figure 9. Temperature elevation *in vitro* kidney using T1- weighted FSPGR (boiling). (a) Ultrasound is OFF; (b)-(f) applied spatial average intensity: 3500 W/cm^2 (for 25 s).

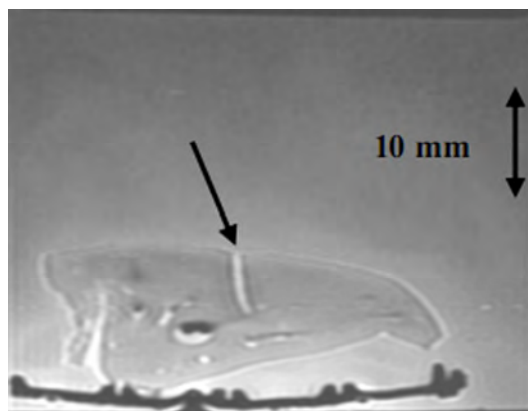


Figure 10. MR image using proton density of lesion in liver created under the influence of boiling. The lesion was created using low intensity (1000 W/cm^2) for long time (30 s).

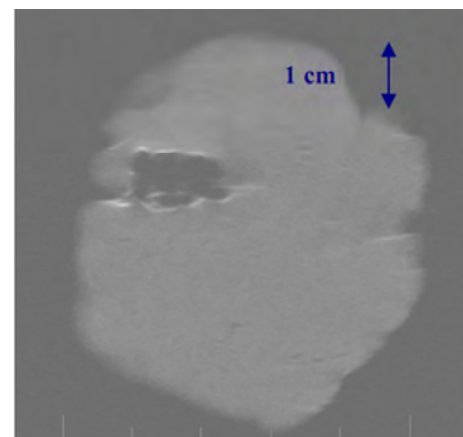


Figure 11. MRI image using T1-w FSE of large boiling lesion created *in vitro* using 2000 W/cm^2 for 20 s.

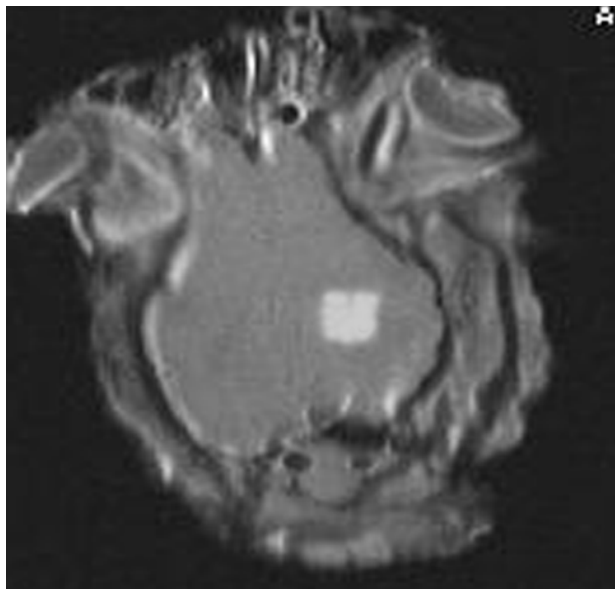


Figure 12. MRI image using T1-w FSE of large thermal lesion created *in vivo* using 2000 W/cm² for 20 s.

possibly re-planning the treatment protocol in the event of incomplete coverage of the target and 4) follow-up imaging, evaluating the effectiveness of HIFU ablation, several days after the treatment. The main goal in this paper was to develop methods for detecting lesions created at temperature below boiling point and lesions created above boiling using MRI techniques.

This paper enhances the role of MRI guidance in HIFU because it provides techniques to discriminate between non-boiling and boiling lesions.

In kidney the best MRI sequence to detect boiling lesions was T2-W FSE. T2-W FSE was evaluated further by plotting the CNR vs. TE for the three regions of interest (kidney, lesion and cavity). It was concluded that between TE's of 20 and 50 ms, the signal difference, and hence the contrast between the three regions of interest (kidney, lesion and cavity) is maximum (**Figure 5**). According to **Figure 5**, the cavity, which appears inside the lesion, has stronger signal and decays slower.

T1-weighted FSE and T1-weighted FSPGR do not consistently show boiling lesions in kidney, and even when cavities are visible the contrast is not very good.

In liver T2-W FSE with low TE (*i.e.* Proton density) is recommended as an MRI sequence to detect non-boiling lesions and boiling lesions.

Previous literature [36,37] demonstrated that lesions in the brain can be monitored with excellent contrast using T1-W FSE. However in the previous studies only thermal lesions were shown. In this paper we have explored extensively the use of MRI to image both lesions created under thermal mechanisms and under boiling.

With T1-w FSE the signal intensity of the brain tissue is homogeneous and therefore the contrast with thermal lesions or with bubbly lesions is excellent. In this study it was concluded that in brain T1-weighted FSE was the optimum MRI sequence not only to detect non-boiling lesions, but also boiling lesions.

It was observed that bubbly lesions appear darker than thermal lesions. Bubbly lesions appear dark, due to the air spaces resulting from cavities caused by boiling or sometimes by cavitation. In the brain tissue *in vitro* it was demonstrated that non-degassed excised tissue is a good model for easily initiating enhanced heating or cavitation since air is trapped in the vasculature of the brain. This model of cavitation might not be of any significant for clinical use since in live tissue cavitation will not occur with such exposure; however, this model of initiating cavitation is very useful for the purpose of studying the MRI appearance of bubbly lesions. The exposure of using 2000 W/cm² in brain results to temperatures of around 90°C (**Figure 12**) *in vivo*. However with the same exposure *in vitro* the resulting estimated maximum temperature was 110°C. This is probably due to enhanced heating or cavitation which results to tissue boiling. The enhanced heating due to bubbles was also noted in the studies by Fry *et al.* [51], by ter Haar [52], and by Chavier *et al.* [53].

This is the first paper demonstrating creation of large lesions in brain formed by scanning the transducer in grid formation. Both thermal and bubbly lesions were monitored successfully using T1-w FSE with excellent contrast, proving the potential of HIFU to treat reliably tumours in the brain in the future. The proposed system effectively creates large lesion in brain and on the same time these lesions are effectively monitored using MRI with strong confidence on the margins of these lesions especially using T1-w FSE.

Boiling bubbles scatter and reflect ultrasound. These reflections result in shielding the HIFU focus and thus increased prefocal heating is observed. Therefore boiling bubbles, similar to cavitation bubbles, result to distortion of the lesion from a cigar shape into a tadpole shape (**Figure 4**). In addition to this the growth of the lesion is shifted towards the transducer. This phenomenon which is attributed to bubbles, either due to ultrasound-induced cavitation or to boiling has been observed also in the study by ter Haar [53], and by Chavier *et al.* [52]. For the scanned lesions the focus is not shifted towards the transducer, because while boiling begins in a very short time in both single and scanned lesions, it cannot distort the lesion for scanned exposures because the focus of the transducer moves away from the boiling site. This speculation is also supported in the paper by Khokhlova [44].

This paper also showed by means of MRI images that focal beam is distorted during the occurrence of boiling. Initially low intensity was used (1000 W/cm^2) and the temperature elevation was monitored using T1-weighted FSPGR. The shortest acquisition time that we could achieve with our system was 5 s. Modifying any MRI parameter to decrease the time resulted to poor contrast or low signal to noise ratio (SNR). If we had achieved faster acquisitions (less than 5 s), then it would have possible to see more drastic changes. A decrease in the signal (black spot) demonstrated the increase in the temperature (also observed by Hynynen *et al.* [54]). The shape of the black spot was circular. The black spot increased gradually with increased temperature, and the shape remains circular at all times (**Figure 8**). When the intensity was increased to 3500 W/cm^2 , the shape of the black spot was irregular indicating that boiling occurred (**Figure 9**).

REFERENCES

- [1] Damianou, C. (2003) *In vitro* and *in vivo* ablation of porcine renal tissues using high intensity focused ultrasound. *Ultrasound in Medicine & Biology*, **29**(9), 1321-1330.
- [2] Damianou, C., Pavlou, M., Velev, O., Kyriakou, K. and Trimikliniotis, M. (2004) High intensity focused ultrasound ablation of kidney guided by MRI. *Ultrasound in Medicine & Biology*, **30**(3), 397-404.
- [3] Watkin, N.A., Morris, S.B., Rivens, I.H. and Ter Haar, G.R. (1997) Highintensity focused ultrasound ablation of the kidney in a large animal model. *Journal of Endourology*, **11**(3), 191-196.
- [4] Roberts, W.W., Hall, T.L., Ives, K., Wolf, J.S., Jr., Fowlkes, J.B. and Cain, C.A. (2006) Pulsed cavitation ultrasound: A noninvasive technology for controlled tissue ablation (histotripsy) in the rabbit kidney. *Journal of Urology*, **175**(2), 734-738.
- [5] Vallancien, G., Chartier-Kastler, E., Harouni, M., Chopin, D. and Bougaran, J. (1993) Focused extracorporeal pyrotherapy: Experimental study and feasibility in man. *Seminars in Urology*, **11**(1), 7-9.
- [6] Susani, M., Madersbacher, S., Kratzik, C., Vingers, L. and Marberger, M. (1993) Morphology of tissue destruction induced by focused ultrasound. *European Urology*, **23**(1), 34-38.
- [7] Wu, F., Wang, Z.B., Chen, W.Z., Bai, J., Zhu, H. and Qiao, T.Y. (2003) Preliminary experience using high intensity focused ultrasound for the treatment of patients with advanced stage renal malignancy. *Journal of Urology*, **170**(6), 2237-2240.
- [8] Marberger, M., Schatzl, G., Cranston, D. and Kennedy, J.E. (2005) Extracorporeal ablation of renal tumours with high-intensity focused ultrasound. *British Journal of Urology International*, **95**(2), 52-55.
- [9] Hacker, A., Michel, M.S., Marlinghaus, E., Kohrmann, K.U. and Alken, P. (2006) Extracorporeally induced ablation of renal tissue by high-intensity focused ultrasound. *British Journal of Urology International*, **97**(4), 779-785.
- [10] Klingler, C., Susani, M., Seip, R., Mauermann, J., Sanghvi, N. and Marberger, M. (2008) A novel approach to energy ablative therapy of small renal tumours: Laparoscopic high-intensity focused ultrasound. *European Urology*, **53**(4), 810-818.
- [11] Taylor, K.J. and Connolly, C.C. (1969) Differing hepatic lesions caused by the same dose of ultrasound. *Journal of Pathology*, **98**(4), 291-293.
- [12] Linke, C.A., Carstensen, E.L., Frizzell, L.A., Elbadawi, A. and Fridd, C.W. (1973) Localized tissue destruction by high-intensity focused ultrasound. *Archives of Surgery*, **107**(6), 887-891.
- [13] Frizzell, L.A. (1988) Threshold dosages for damage to mammalian liver by high intensity focused ultrasound. *IEEE Transactions on Ultrasonics, Ferroelectrics and Frequency Control*, **35**(5), 578-581.
- [14] Ter Haar, G. and Robertson, D. (1993) Tissue destruction with focused ultrasound *in vivo*. *European Urology*, **23**(1), 8-11.
- [15] Chen, L., Ter Haar, G., Hill, C.R., Dworkin, M., Carnochan, P., Young, H. and Bensted, J.P. (1993) Effect of blood perfusion on the ablation of liver parenchyma with high-intensity focused ultrasound. *Physics in Medicine and Biology*, **38**(11), 1661-1673.
- [16] Sibille, A., Prat, F., Chapelon, J.Y., Abou el Fadil, F., Henry, L., Theillere, Y., Ponchon, T. and Cathignol, D. (1993) Extracorporeal ablation of liver tissue by high-intensity focused ultrasound. *Oncology*, **50**(2), 375-379.
- [17] Moore, W.E., Lopez, R.-M., Mathews, D.E., Sheets, P.W., Etchison, M.R., Hurwitz, A.S., Chalian, A.A., Fry, F.J., Vane, D.W. and Grosfeld, J.L. (1989) Evaluation of high-intensity therapeutic ultrasound irradiation in the treatment of experimental hepatoma. *Journal of Pediatric Surgery*, **24**(1), 30-33.
- [18] Yang, R., Reilly, C.R., Rescorla, F.J., Faught, P.R., Sanghvi, N.T., Fry, F.J., Franklin, T.D., Jr., Lumeng, L. and Grosfeld, J.L. (1991) Highintensity focused ultrasound in the treatment of experimental liver cancer. *Archives of Surgery*, **126**(8), 1002-1010.
- [19] Sibille, A., Prat, F., Chapelon, J.Y., Abou el Fadil, F., Henry, L., Theillere, Y., Ponchon, T. and Cathignol, D. (1993) Characterization of extracorporeal ablation of normal and tumor-bearing liver tissue by high intensity focused ultrasound. *Ultrasound in Medicine & Biology*, **19**(9), 803-813.
- [20] Prat, F., Centarti, M., Sibille, A., Abou el Fadil, F.A., Henry, L., Chapelon, J.Y. and Cathignol, D. (1995) Extracorporeal high-intensity focused ultrasound for VX2 liver tumors in the rabbit. *Hepatology*, **21**(3), 832-836.
- [21] Ter Haar, G., Rivens, I., Chen, L. and Riddler, S. (1991) High intensity focused ultrasound for the treatment of rat tumours. *Physics in Medicine and Biology*, **36**(11), 1495-1501.
- [22] Ter Haar, G., Clarke, R.L., Vaughan, M.G. and Hill, C.R. (1991) Trackless surgery using focused ultrasound: Technique and case report. *Minimally Invasive Therapy and Allied Technologies*, **1**(1), 13-19.
- [23] Vallancien, G., Harouni, M., Veillon, B., Mombet, A., Prapotnich, D., Brisset, J.M. and Bougaran, J. (1992) Focused extracorporeal pyrotherapy: Feasibility study in man. *Journal of Endourology*, **6**, 173-181.

- [24] Wu, F., Chen, W. and Bai, J. (1999) Effect of high-intensity focused ultrasound on patients with hepatocellular cancer—preliminary report. *Chinese Journal of Ultrasonog*, **8**, 213-216.
- [25] Li, C.X., Xu, G.L., Jiang, Z.Y., Li, J.J., Luo, G.Y., Shan, H.B., Zhang, R. and Li, Y. (2004) Analysis of clinical effect of high-intensity focused ultrasound on liver cancer. *World Journal of Gastroenterology*, **10**(15), 2201-2204.
- [26] Wu, F., Wang, Z.B., Chen, W.Z., Zou, J.Z., Bai, J., Zhu, H., Li, K.Q., Jin, C.B., Xie, F.L. and Su, H.B. (2005) Advanced hepatocellular carcinoma: Treatment with high-intensity focused ultrasound ablation combined with transcatheter arterial embolization. *Radiology*, **235**(5), 659-667.
- [27] Gedroyc, W.M. (2006) Magnetic resonance guided focused ultrasound (MRgFUS) treatment of liver tumours. In: Coussios, C.C., Ed., *6th International Symposium on Therapeutic Ultrasound*, Oxford, 30 August-2 September 2006, 539-547.
- [28] Fry, W., Mosberg, W., Barnard, J. and Fry, F. (1954) Production of focal destructive lesions in the central nervous system with ultrasound. *Journal of Neurosurgery*, **11**(2), 471-478.
- [29] Lele, P.P. (1962) A simple method for production of trackless focal lesions with focused ultrasound. *Journal of Physiology*, **160**(3), 494-512.
- [30] Fry, F. and Johnson, L.K. (1978) Tumor irradiation with intense ultrasound. *Ultrasound in Medicine & Biology*, **4**(4), 337-341.
- [31] Britt, R.H., Lyons, B.E., Pounds, D.W. and Prionas, S.D. (1983) Feasibility of ultrasound hyperthermia in the treatment of malignant brain tumors. *Medical Instrumentation*, **7**(2), 172-177.
- [32] Guthkelch, A.N., Carter, L.P., Cassady, J.R., Hynynen, K.H., Iacono, R.P., Johnson, P.C., Obbens, E.A., Roemer, R.B., Seeger, J.F. and Shimm, D.S. (1991) Treatment of malignant brain tumors with focused ultrasound hyperthermia and radiation: results of a phase I trial. *Journal of Neuro-Oncology*, **10**(3), 271-284.
- [33] Vykhodtseva, N.I., Hynynen, K. and Damianou, C. (1994) Pulse duration and peak intensity during focused ultrasound surgery: Theoretical and experimental effects in rabbit brain *in vivo*. *Ultrasound in Medicine & Biology*, **20**(9), 987-1000.
- [34] Hynynen, K., Vykhodtseva, N.I., Chung, A.H., Sorrentino, V., Colucci, V. and Jolesz, F.A. (1997) Thermal effects of focused ultrasound on the brain: Determination with MR imaging. *Radiology*, **204**(1), 247-253.
- [35] Vykhodtseva, N., Sorrentino, V., Jolesz, F.A., Bronson, R.T. and Hynynen, K. (2000) MRI detection of the thermal effects of focused ultrasound on the brain. *Ultrasound in Medicine & Biology*, **26**(5), 871-880.
- [36] Hynynen, K., McDannold, N., Vykhodtseva, N. and Jolesz, F. (2001) Noninvasive MR imaging-guided focal opening of the blood-brain-barrier in rabbits. *Radiology*, **220**(3), 640-646.
- [37] Hynynen, K., McDannold, N., Martin, H., Jolesz, F., Vykhodtseva, N. (2003) The threshold for brain damage in rabbits induced by bursts of ultrasound in the presence of an ultrasound contrast agent (optison). *Ultrasound in Medicine & Biology*, **29**(3), 473-481.
- [38] Hynynen, K., McDannold, N., Sheikov, N., Jolesz, F., Vykhodtseva, N. (2005) Local and reversible blood-brain barrier disruption by noninvasive focused ultrasound at frequencies suitable for trans-skull sonications. *NeuroImage*, **24**(1), 12-20.
- [39] Jolesz, F.A. and Jakab, P.D. (1991) Acoustic pressure wave generation within a magnetic resonance imaging system: Potential medical applications. *Magnetic Resonance Imaging*, **1**(5), 609-613.
- [40] Hynynen, K., Darkazanli, A., Damianou, C., Unger, E. and Schenck, J.F. (1992) MRI-guided ultrasonic hyperthermia. 1992 *Radiological Society of North America Annual Meeting*, September 1992.
- [41] Hynynen, K., Damianou, C., Darkazanli, A., Unger, E. and Schenck, J.F. (1993) The feasibility of using MRI to monitor and guide noninvasive ultrasound surgery. *Ultrasound in Medicine & Biology*, **19**(1), 91-92.
- [42] Hynynen, K., Darkazanli, A., Damianou, C.A., Unger, E. and Schenck, J.F. (1993) Tissue thermometry during ultrasound exposure. *European Urology*, **23**(1), 12-16.
- [43] Hynynen, K., Freund, W.R., Cline, H.E., Chung, A.H., Watkins, R.D., Vetro, J.P. and Jolesz, F.A. (1996) A clinical, noninvasive, MR imaging-monitored ultrasound surgery method. *Radiographics*, **16**(1), 185-195.
- [44] Khokhlova, V., Bailey, M., Reed, J., Cunitz, B., Kaczowski, P. and Crum, L. (2006) Effects of nonlinear propagation, cavitation, and boiling in lesion formation by high intensity focused ultrasound, in a gel phantom. *Journal of the Acoustical Society of America*, **119**(3), 1834-1848.
- [45] Coussios, C., Farny, C., Ter Haar, G. and Roy, R. (2007) Role of acoustic cavitation in the delivery and monitoring of cancer treatment by high-intensity focused ultrasound (HIFU). *International Journal of Hyperthermia*, **23**(2), 105-120.
- [46] Chung, A.H., Hynynen, K., Colucci, V., Oshio, K., Cline, H.E. and Jolesz, F.A. (1996) Optimization of spoiled gradient-echo phase imaging for *in vivo* localization of a focused ultrasound beam. *Magnetic Resonance in Medicine*, **36**(5), 745-752.
- [47] Vykhodtseva, V., Sorrentino, V., Jolesz, F., Bronson, R. and Hynynen, K. (2000) MRI detection of the thermal effects of focused ultrasound on the brain. *Ultrasound in Medicine & Biology*, **26**(5), 871-880.
- [48] Quesson, B., Zwart, J. and Moonen, C. (2000) Magnetic resonance temperature imaging for guidance of thermotherapy. *Journal of Magnetic Resonance Imaging*, **12**(4), 525-533.
- [49] Salomir, R., Palussière, J., Vimeux, F.C., de Zwart, J.A., Quesson, B., Gauchet, M., Lelong, P., Pergrale, J., Grenier, N. and Moonen, C.T.W. (2000) Local hyperthermia with MR-guided focused ultrasound: Spiral trajectory of the focal point optimized for temperature uniformity in the target region. *Journal of Magnetic Resonance Imaging*, **12**(4), 571-583.
- [50] McDannold, N., Hynynen, K. and Jolesz, F. (2000) MRI monitoring of the thermal ablation of tissue: Effects of long exposure times. *Journal of Magnetic Resonance Imaging*, **13**(3), 421-427.
- [51] Fry, F.J., Kossoff, G., Eggleton, R.C. and Dunn, F. (1970) Threshold ultrasound dosages for structural changes in

- the mammalian brain. *Journal of the Acoustical Society of America*, **48(6)**, 1413-1417.
- [52] ter Haar, G. (1995) Ultrasound focal beam surgery. *Ultrasound in Medicine & Biology*, **21(9)**, 1089-1100.
- [53] Chavrier, F., Chapelon, Y., Gelet, A. and Cathignol, D. (2000) Modelling of high-intensity focused ultrasound-induced lesions in the presence of cavitation bubbles. *Journal of the Acoustical Society of America*, **108(1)**, 432-440.
- [54] Hynynen, K., Damianou, C.A., Colucci, V., Unger, E., Cline, H.H. and Jolesz, F.A. (1995) MR monitoring of focused ultrasonic surgery of renal cortex: Experimental and simulation studies. *Journal of Magnetic Resonance Imaging*, **5(3)**, 259-266.

Anisotropic WM conductivity reconstruction based on diffusion tensor magnetic resonance imaging: a simulation study*

Dandan Yan¹, Wenlong Xu¹, Jing Li²

¹College of Information Engineering, China JiLiang University, Hangzhou, China;

²Center for THz Research, China Jiliang University, Hangzhou, China.

Email: dandanyan@cjlj.edu.cn

Received 18 May 2010; revised 8 June 2010; accepted 11 June 2010.

ABSTRACT

The present study aims to estimate the *in vivo* anisotropic conductivities of the White Matter (WM) tissues by means of Magnetic Resonance Electrical Impedance Tomography (MREIT) technique. The realistic anisotropic volume conductor model with different conductivity properties (scalp, skull, CSF, gray matter and WM) is constructed based on the Diffusion Tensor Magnetic Resonance Imaging (DT-MRI) from a healthy human subject. The Radius Basic Function (RBF)-MREIT algorithm of using only one magnetic flux density component was applied to evaluate the eigenvalues of the anisotropic WM with target values set according to the DT-MRI data based on the Wolter's model, which is more physiologically reliable. The numerical simulations study performed on the five-layer realistic human head model showed that the conductivity reconstruction method had higher accuracy and better robustness against noise. The pilot research was used to judge the feasibility, meaningfulness and reliability of the MREIT applied on the electrical impedance tomography of the complicated human head tissues including anisotropic characteristics.

Keywords: Magnetic Resonance Electrical Impedance Tomography; Radius Basic Function Neural Network; Diffusion Tensor Magnetic Resonance Imaging; Anisotropic Conductivity; WM

1. INTRODUCTION

Knowledge of the electrical conductivity distribution in human body is important to many biomedical applications [1]. Brain disease and brain function activities always accompany with changing conductivities of human

head tissues. In the electroencephalography (EEG) or magnetoencephalography (MEG) based source localization or imaging, the conductivity distribution is often assumed to be isotropic and piece-wise homogeneous. However, this assumption is not entirely accurate since the conductivity is highly anisotropic within the WM [1]. The more accurate conductivity distribution of the WM volume is needed for accurate source localization from EEG/MEG.

The cerebral WM is considered as glia and axons bathing in the interstitial fluid. WM shows obvious anisotropy due to its much complicated nerve fiber distribution. Some methods have been reported to get the anisotropic WM conductivity [2,3], which are based on Basser's [4] theory to infer the electrical conductivity tensor from the water self-diffusion tensor measured by diffusion tensor magnetic resonance imaging (DT-MRI). Self-consistent differential effective medium approach (EMA) [2,5] was used to deduce the anisotropic conductivity of the WM tissue: $\sigma_{WM} = k dW$ ($k = 0.736S \cdot s/mm^3$) where dW denoted the eigenvalues of the water diffusion tensor and σ_{WM} was the eigenvalue of the WM conductivity. Wolters [6] has done some study to infer the eigenvalues of the WM considering the nerve fiber structure using the volume constraint and Wang's constraint. Wang [7] proposed a new algorithm to derive the anisotropic conductivity of the cerebral WM from the diffusion tensor magnetic resonance imaging data.

The lack of techniques for robust measurement of the electrical conductivity tensor *in vivo* has discouraged the inclusion of anisotropic conductivity information in the electromagnetic source imaging forward model [8]. Tuch's and other methods all fell back on to deduce the anisotropic WM model directly, which were faced with the difficulties to validate. The research on the electrical characteristic of the head tissues is performed through two ways. *In vivo* and *in vitro* measurements of the con-

*This work was supported by grants from the Zhejiang Provincial Natural Science Foundation of China (No. Y1080215 and No. Y2090966).

ductivities, especially the brain and skull tissues have been published in some literatures [8,9]. Noninvasive MREIT imaging modality has been developed to reconstruct high-resolution conductivity distribution images for the biological tissues.

In this new imaging modality, the traditional Electrical Impedance Tomography (EIT) is combined with magnetic resonance-current density imaging (MR-CDI) technique to solve the well-known ill-posedness of the image reconstruction problem in traditional EIT due to the less effectiveness caused by the low skull conductivity. In MREIT, currents are injected into the subject through pairs of surface electrodes. A Magnetic Resonance Imaging (MRI) scanner is used to measure the induced magnetic flux density inside the subject and the current density distribution can be calculated according to the Ampere's law. The conductivity distribution image can be reconstructed based on the relationship between the conductivity and the measured magnetic flux density combined with the current density. MREIT reconstruction algorithms fall into two categories [10]: those utilizing internal current density [10-14] and those making use of measured magnetic flux density [15-22]. Considering the rotation problem of the object in the MRI system, the latter has the advantage of avoiding the object rotation over the former. Recently, the algorithm based on only one component of the magnetic flux density gains more attention. Several MREIT algorithms have been proposed, which utilize only one component of magnetic flux density, such as the harmonic B_z algorithm [14,23], the gradient B_z decomposition algorithm [19], the algebraic reconstruction algorithm [18] and an anisotropic conductivity reconstruction algorithm [24].

For the head tissue conductivity, the relatively novel and concise Radial Basis Function (RBF) and Response Surface Methodology (RSM) MREIT algorithms [20,21] have been proposed to focus on the piece-wise homogeneous head tissue conductivity reconstruction. Therefore, RBF-MREIT approach was extended to realize the estimation of anisotropic WM conductivity distribution of the head tissues in this paper. In the present study, a computer simulation study was performed on a five-layer (scalp, skull, CSF, gray matter and WM) realistic geometry head finite element method (FEM) model. The results showed that the only one component magnetic flux density used could get the same or even better results and confirmed the potential application of the MREIT technology on more complex conductivity distribution reconstruction of human body as well as clinic experiment. The MREIT method could offer a means to the more sophisticated conductivity model including anisotropic tissue.

2. METHODS

For the present approach, some assumptions should be given. For the realistic head model, the isotropic conductivities of the scalp, skull, gray matter and CSF were set according to the in-vivo measured value of the literatures [8,9,25]. Conductivity tensor of the WM was obtained from the DT-MRI data measurements acquired from a healthy human subject and shared the same eigenvectors with the water diffusion tensors based on Basser's hypothesis [4]. In this simulation study, the target conductivity distribution was set based on the measured tensor data of the WM with the eigenvalue set according to Wolters' [6]. The conductivity tensor map derived from the diffusion tensor image provided the anisotropic conductivity values for each element. The RBF-MREIT [20] algorithm was used to perform the computer simulations on a realistic head model. In the algorithm realization, the current density data and magnetic flux density data were used to estimate the anisotropic conductivity, respectively.

A five-layer (scalp, skull, CSF, gray matter and WM) realistic FEM head model was constructed based on a three-layer FEM head model [26] and T1-MRI data (see **Figure 1**). FEM was used to solve the forward problem of the MREIT, and then the anisotropic conductivity of the WM was reconstructed by the extended RBF-MREIT algorithm.

2.1. Realistic FEM Head Model

An appropriate and sophisticated head model is essential to localize equivalent sources of bioelectric activity of the human brain from the electroencephalogram (EEG). A realistic head model can describe the shape of tissues more accurately.

We first reconstruct a 3D solid model from BEM model and then generate the FEM mesh on the constructed

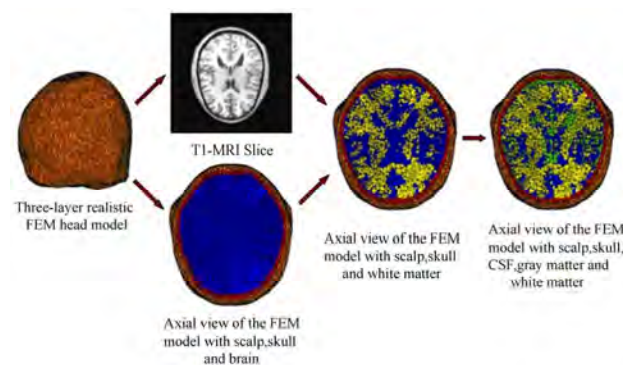


Figure 1. Head model with yellow represents the WM, dark blue the gray matter, green the CSF, red the skull, and brown the skin.

3D model. The tissue interfaces are described by many surface elements in the BEM model thus the 3D solid model of tissue can be built simply by joining the surface elements into a closed surface. Once given the 3D solid model, the 3D FEM model can be obtained easily by dividing the solid model of the tissue. A CAD software Rhino and a FEM software ANSYS are used.

Based on the T1-weighted MRI data, a realistic five-layer head model was constructed by FEM and boundary element method (BEM) with 351386 quadratic tetrahedral elements and 485767 nodes. ANSYS 10.0 was used in the finite element modeling and the forward problem calculation based on the EFM realistic head model.

The diffusion distribution of the conductivity could be denoted by a 3×3 symmetric positive definite matrix:

$$\sigma = \begin{bmatrix} \sigma_{11} & \sigma_{12} & \sigma_{13} \\ \sigma_{21} & \sigma_{22} & \sigma_{23} \\ \sigma_{31} & \sigma_{32} & \sigma_{33} \end{bmatrix}. \text{ When } \sigma_{11} = \sigma_{22} = \sigma_{33} \text{ were con-}$$

stants and other components were zero, the matrix could be rendered as isotropic diffusion conductivity for the grey matter and CSF tissues. For the anisotropic WM, the diffusion distribution of the conductivities in each element (voxel) of the FEM model were written as $\sigma = S\Lambda_{WM}S^T$, where $S = [S_1 \ S_2 \ S_3]$ denoted the three unit length orthogonal eigenvectors of the measured diffusion tensor at the center of a WM finite element and $\Lambda_{WM} =$

$$\begin{bmatrix} \lambda_{long} & 0 & 0 \\ 0 & \lambda_{trans} & 0 \\ 0 & 0 & \lambda_{trans} \end{bmatrix} \text{ was the eigenvalue. } \lambda_{long} \text{ and } \lambda_{trans}$$

were the eigenvalue parallel (longitudinal) and perpendicular (trans-verse) to the fiber directions, respectively. The target conductivity distributions of the scalp, skull, CSF, gray matter and WM were set according to the measured data of corresponding tissues [9,25]. The WM was set with anisotropic conductivity distribution based on some existing measured data [2,6] and its anisotropic characteristics.

2.2. Conductivity Reconstruction

MREIT imaging modality has been developed to reconstruct high-resolution conductivity distribution images for the biological issues. In this new imaging modality, currents are injected into the subject through pairs of surface electrodes. A Magnetic Resonance Imaging (MRI) scanner is used to measure the induced magnetic flux density \mathbf{B} inside the subject and the current density distribution \mathbf{J} can be calculated according to the Ampere's law. The conductivity distribution images can be reconstructed based on the relationship between the conductivity and the measured magnetic flux density combined with the current density. MREIT is used to image the conductivities of the human tissues, especially

in the human head. The advantages lie in that the magnetic signals tend to penetrate into the inner brain through the low conductivity skull. MREIT reconstruction algorithms mainly fall into two categories: those utilizing internal current density \mathbf{J} and those making use of only one component of measured magnetic flux density \mathbf{B} . Due to the fact that only one component of the magnetic flux density which parallels to the direction of the main magnetic field of the MRI scanner can be measured once, the rotation of the object is required, which is impractical for MRI scanner. Considering the rotation problem, the latter has the advantages over the former of avoiding the object rotation dilemma. MREIT algorithms that are based on current density require knowledge of the magnetic flux density vector $\mathbf{B} = [B_x, B_y, B_z]$.

MREIT reconstruction consists of the forward problem and the inverse problem. With given conductivity and boundary condition, the calculation of peripheral voltage values, current density distribution and/or magnetic flux density is referred to as the forward problem of MREIT. The inverse problem deals with the reconstruction of conductivity using the measured magnetic flux density and computed current density information.

2.2.1. Forward Problem

Under the quasi-static conditions, the relation between the conductivity and the electrical potential $U(r)$ induced by the injected current is given by Poisson's equation together with the Neumann boundary conditions as:

$$\nabla \cdot [\sigma(r) \nabla U(r)] = 0, \quad r \in \Omega \quad (1)$$

$$\sigma \frac{\partial U}{\partial n} = \begin{cases} J_{inj} & \text{on positive current electrode} \\ -J_{inj} & \text{on negative current electrode} \\ 0 & \text{elsewhere} \end{cases}$$

where $\sigma(r)$ is the electrical conductivity, Ω , the imaging subject space, J_{inj} , the amount of injected current and ∇ , the gradient operator. For complex conductivity distributions, analytical solution to the forward problem expressed in Eq.1 does not exist. Therefore, a numerical method must be applied. Finite element method (FEM) is used to calculate the electrical potential and corresponding magnetic flux density distribution for a given conductivity distribution and boundary condition.

After obtaining the electric potential distribution $U(r)$ from solving Eq.1, the electric field and the interior current density distribution are given as:

$$\begin{aligned} E &= -\nabla U \\ J &= \sigma E \end{aligned} \quad (2)$$

Then the magnetic flux density can be calculated using the Biot-Savat law:

$$B(r) = \frac{\mu_0}{4\pi} \int_{\Omega} J(r') \times \frac{r-r'}{|r-r'|^3} dv' \quad (3)$$

where $B(r)$ is the magnetic flux density at the measurement point, $J(r')$ the current density at the source point and μ_0 the magnetic permeability of the free space. In order to avoid the singularity occurring when $r = r'$, $B(r)$ is treated as a node variable and $J(r')$ is used at the centre of each finite element in Eq.3. The comparison between the analytical solution and the numerical solution by FEM method was performed [20,21] to indicate the feasibility of solving the forward problem using the FEM.

2.2.2. Inverse Problem

For the inverse problem, the Radius Basic Function (RBF) Neural Network system was used to seek the optimal estimation eigenvalues of the target conductivities: λ_{long} and λ_{trans} of the WM, respectively. The conductivity of the gray matter σ_{GM} and CSF σ_{CSF} were assumed to be isotropic, thus each conductivity tensor has the same value in three directions. The eigenvector data of each element got from the DT-MRI measuring were combined with the initial sample eigenvalues belong to a certain range to perform the forward calculation. Based on the sample data $\delta = \{B, J\}$ and the measured data " $\delta^* = \{B^*, J^*\}$ " from the forward calculation, the objection function was set up and the RBF-MREIT algorithm was used to reconstruct the anisotropic conductivity eigenvalues of the WM.

In the RBF-MREIT algorithm description, the relationship between the estimated target values [λ_{long}^{target} , λ_{trans}^{target}] and the measured data " $\delta^* = \{B^*, J^*\}$ " was considered as a "black box". The Radius Basic Function neural network was used herein to rebuild the input-output relation system. After the system was trained by the sample sets including the inputs and outputs couple data, the optimal parameters of the system were found through the optimization algorithm. Then the target values of the eigenvalues were reconstructed finally. There were two processes in the realization of the RBF-MREIT algorithm: the function set up and the function optimization (See Figure 2).

2.2.3. The Function Set Up

The inputs of the function were assumed as the sample values of the unknown anisotropic eigenvalues [λ_{long} , λ_{trans}] of the WM conductivity. The output was defined as the objective function $f(\sigma^*, \sigma)$ between the measured data " $\delta^* = \{B^*, J^*\}$ " and the computed sample data $\delta = \{B, J\}$.

$$f(\sigma^*, \sigma) = (1 - CC(\delta^*, \delta))^2 + RE(\delta^*, \delta)^2 \quad (4)$$

where $CC(\delta^*, \delta)$ and $RE(\delta^*, \delta)$ denoted the correlation coefficient and relative error, respectively.

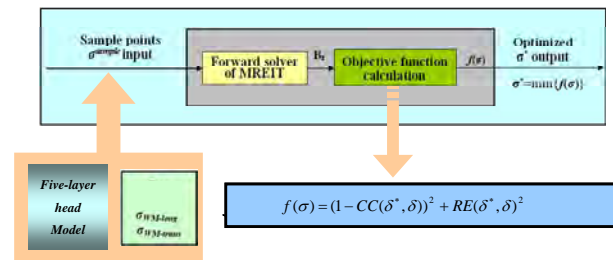


Figure 2. Flowchart of the RBF-MREIT algorithm frame.

2.2.4. The Function Optimization

Once the function between the input σ and the output $f(\sigma)$ is obtained, optimization method, herein the simplex method, could be used to find the optimum point where the objective function $f(\sigma)$ is minimum and the measured data " $\delta^* = \{B^*, J^*\}$ " were most close to the computed sample data set $\delta = \{B, J\}$ as well as the target σ^* to the estimated σ .

In conclusion, the inverse problem of the present RBF-MREIT algorithm could be realized as follows: *Step 1*: According to certain rules, some sampling input points σ were chosen in the region of interest, and the corresponding objective functions $f(\sigma)$ were calculated by solving the forward problem. *Step 2*: The sampling input-output pairs were used to train the RBF network and the trained RBF network function $f(\sigma)$ was obtained. *Step 3*: Estimating the optimum input parameter σ^j that minimizes the output value using the simplex method. *Step 4*: Resetting the region of interest by shrinking the old region of interest to a new region and choosing the optimum input parameters as the centre of the new region. *Step 5*: If the new region of interest was small enough or $\|\sigma^{j+1} - \sigma^j\| \leq \varepsilon$, then stop, otherwise, go to step 1, where σ^{j+1} and σ^j were the estimated conductivity distribution at the $(i+1)$ th and i th iterations, respectively, and ε was the allowable error.

3. SIMULATION STUDY

In order to test the performance of RBF-MREIT algorithm, numerical simulations were performed on a concentric five-layer human head model (consisting of the scalp, skull, CSF, gray matter and WM) to estimate the unknown anisotropic conductivity eigenvalues of the WM. The results of the RBF-MREIT algorithm based on different data δ were compared and analyzed.

3.1. Simulation Parameters

5mA bipolarity square-wave electric currents of 20Hz frequency were injected into the head along the equator of the head model as shown in Figure 3, which allowed more signals flowing into the inner brain [20]. 7 electrode pair positions were chosen to inject the current in

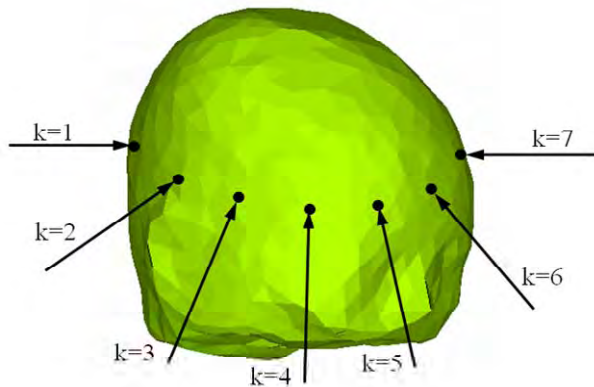


Figure 3. The locations of the electrodes and injected currents for MREIT on the five-layer FEM head model.

order to assess the effects of the injected current numbers to the imaging results under different SNR levels, MRI system was used to measure the magnetic flux density induced by the injected current, and further the current density distribution could be computed according to the electromagnetic theory. In our research, the measured data “ $\delta^* = \{B^*, J^*\}$ ” were all simulated according to the given target conductivity distribution through the forward problem.

To test the noise tolerance of the algorithm, noises of different levels were added to the “measured” B_z . The standard deviation of the added noise S_B was set [27] as:

$$S_B = \frac{1}{2\gamma T_c \text{SNR}} \quad (5)$$

$$S_J = \frac{1}{2\gamma\mu_0 T_c \text{SNR}} \sqrt{\left(\frac{1}{\Delta x}\right)^2 + \left(\frac{1}{\Delta y}\right)^2} \quad (6)$$

where $\gamma = 26.75 \times 10^7 \text{ radT}^{-1} \text{ s}^{-1}$ was the gyromagnetic ratio of hydrogen, T_c the duration of injection current pulse of 50ms and SNR the signal-to-noise ratio of the MR magnitude image. The SNR of the MR magnitude image with additive Gaussian White Noise (GWN) was set to be infinite, 90, 60, 30 and 15, respectively. Δx and Δy denoted the border of the element.

In this study, the relative error (RE) between the estimated and the target conductivity distributions was used to quantitatively assess the performance of the MREIT reconstruction algorithm. The RE was defined as:

$$RE(\sigma, \sigma^*) = \frac{\|\sigma^* - \sigma\|}{\|\sigma^*\|} \times 100\% \quad (7)$$

where σ^* was the target conductivity distribution and σ the estimated conductivity distribution. Given the pre-mised data and the known isotropic tissue conductivities of the scalp $\sigma_{\text{scalp}} = 0.33 \text{ s/m}$, the skull $\sigma_{\text{skull}} = 0.0165 \text{ s/m}$, the

CSF $\sigma_{\text{CSF}} = 1.75 \text{ s/m}$ and the gray matter $\sigma_{\text{GM}} = 1.75 \text{ s/m}$ [9, 25], the unknown eigenvalues of the WM conductivities were reconstructed with the proposed RBF-MREIT algorithm based on different data δ (See **Figure 4**).

The target eigenvalues $[\lambda_{\text{long}}^{\text{target}} = 0.6498, \lambda_{\text{trans}}^{\text{target}} = 0.06498]$ (See **Table 1**) for all the WM tissue elements of the FEM realistic head model were set according to [2, 6]. Sample values were selected in the domain: $[\lambda_{\text{long}}^{\text{WM}}, \lambda_{\text{trans}}^{\text{WM}}] \in (0, 10) \times (0, 1)$ as the eigenvalue of the WM tissue element. Then the “measured” $B^* = [B_x^*, B_y^*, B_z^*]$ and calculated $J^* = [J_x^*, J_y^*, J_z^*]$ were calculated through the forward problem computation. Finally, the objective function was set up to search for the optimum value to minimize the function.

3.2. Results

Given the parameters assumed above, the inverse problem was solved by the RBF-MREIT to search for the optimum conductivity values. The reconstructed results based on the one component magnetic flux density B_z under different SNR levels were listed in **Table 1**, where $k = 1, \dots, 7$ denoted the number of the injected currents.

Based on the data $\delta = [B_z]$ with five noise levels, the REs of the two estimated variables were less than 11%. When SNR=15, the RE of the estimated eigenvalues of the two directions was about 10%. In ideal situation without noise, the RE was about 7%. **Table 1** showed that the present algorithm could reconstruct the conductivity distributions well even with the increase of the noise levels. The present simulation results demonstrated that the RBF-MREIT algorithm could reconstruct well the eigenvalues of the anisotropic conductivity image and was robust to the measurement noise.

Figure 5 showed the section of the target and reconstructed anisotropic WM conductivities, which gave more direct description. **Figure 6** further illustrated the reconstruction results with various SNR when the number k of the current injected changed from 1 to 7. From the results, we can see that the REs do not decrease when the number of the current injected increasing.

Figure 6 displayed that the accuracy was not propor-

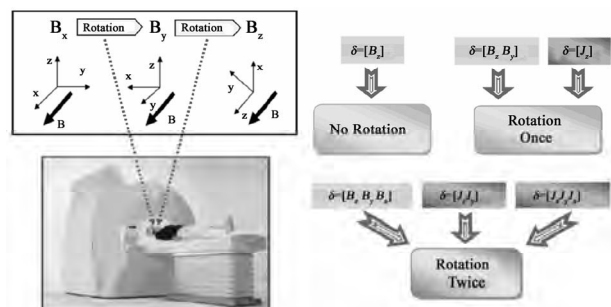


Figure 4. The composing of the objective function set up data δ .

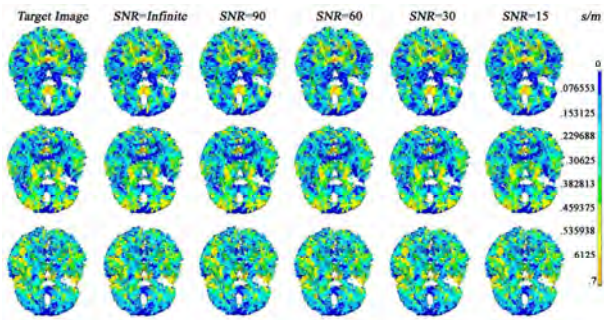


Figure 5. The target and the reconstructed conductivity image with different noise levels in three directions ($\delta = [B_z]$, $k = 1$).

tional to the numbers of the injected current for the reconstructed anisotropic conductivity image based on the RBF-MREIT algorithm. The same results could be got

as well as the data $\delta = [B_z B_y]$, $\delta = [B_z B_y B_x]$, $\delta = [J_z]$, $\delta = [J_z J_y]$ and $\delta = [J_z J_y J_x]$ were used to reconstruct the unknown eigenvalues of the WM tissue.

Figure 7 depicted the REs between the estimated and target conductivity distributions through different data $\delta = \{B, J\}$ with different noise levels. **Figure 7** indicated that the REs of the reconstructed results based on $\delta = [B_z]$ and $\delta = [J_z]$ are basically the same, as well as in the cases $\delta = [B_z B_y]$ and $\delta = [J_z J_y]$, $\delta = [B_z B_y B_x]$ and $\delta = [J_z J_y J_x]$. The reconstruction method using $\delta = [B_z B_y]$, $\delta = [J_z J_y]$, $\delta = [B_z B_y B_x]$ and $\delta = [J_z J_y J_x]$ needed to rotate the human head at least once to twice in order to acquire the magnetic flux density and current density data. Especially, the method based on $\delta = [J_z J_y J_x]$ required the rotation which was not impractical in the clinic experiment.

Table 1. Reconstructed results of the WM for the realistic head model ($\delta = [B_z]$)

SNR	Current Inject	$\lambda_1^{target} = 0.64890$		$\lambda_4^{target} = 0.06489$	
		λ_1	RE	λ_4	RE
Infinite	k = 1	0.6479 ± 0.0112	0.0790 ± 0.0181	0.0649 ± 0.0012	0.0760 ± 0.0177
	k = 2	0.6413 ± 0.0025	0.0691 ± 0.0073	0.0647 ± 0.0002	0.0659 ± 0.0010
	k = 3	0.6581 ± 0.0040	0.0608 ± 0.0047	0.0638 ± 0.0004	0.0688 ± 0.0181
	k = 4	0.6328 ± 0.0033	0.0754 ± 0.0012	0.0652 ± 0.0000	0.0502 ± 0.0002
	k = 5	0.6443 ± 0.0011	0.0753 ± 0.0066	0.0649 ± 0.0000	0.0661 ± 0.0069
	k = 6	0.6582 ± 0.0002	0.0726 ± 0.0028	0.0647 ± 0.0003	0.0699 ± 0.0067
	k = 7	0.6426 ± 0.0042	0.0619 ± 0.0105	0.0647 ± 0.0005	0.0687 ± 0.0078
90	k = 1	0.6499 ± 0.0133	0.0792 ± 0.0182	0.0650 ± 0.0013	0.0774 ± 0.0185
	k = 2	0.6582 ± 0.0077	0.0835 ± 0.0127	0.0654 ± 0.0004	0.0660 ± 0.0111
	k = 3	0.6424 ± 0.0070	0.0615 ± 0.0056	0.0663 ± 0.0016	0.0772 ± 0.0026
	k = 4	0.6415 ± 0.0105	0.0797 ± 0.0056	0.0639 ± 0.0001	0.0688 ± 0.0016
	k = 5	0.6357 ± 0.0037	0.0763 ± 0.0105	0.0643 ± 0.0002	0.0745 ± 0.0078
	k = 6	0.6495 ± 0.0019	0.0831 ± 0.0037	0.0657 ± 0.0010	0.0712 ± 0.0090
	k = 7	0.6414 ± 0.0083	0.0665 ± 0.0108	0.0641 ± 0.0012	0.0738 ± 0.0080
60	k = 1	0.6469 ± 0.0133	0.0810 ± 0.0183	0.0648 ± 0.0014	0.0813 ± 0.0186
	k = 2	0.6426 ± 0.0103	0.0859 ± 0.0157	0.0654 ± 0.0005	0.0665 ± 0.0126
	k = 3	0.6491 ± 0.0083	0.0666 ± 0.0122	0.0632 ± 0.0021	0.0795 ± 0.0120
	k = 4	0.6492 ± 0.0115	0.0802 ± 0.0080	0.0650 ± 0.0002	0.0874 ± 0.0018
	k = 5	0.6545 ± 0.0077	0.0863 ± 0.0136	0.0657 ± 0.0010	0.0786 ± 0.0153
	k = 6	0.6324 ± 0.0051	0.0884 ± 0.0060	0.0654 ± 0.0017	0.0765 ± 0.0135
	k = 7	0.6348 ± 0.0179	0.0688 ± 0.0109	0.0645 ± 0.0012	0.0825 ± 0.0111
30	k = 1	0.6510 ± 0.0151	0.0853 ± 0.0194	0.0650 ± 0.0015	0.0820 ± 0.0194
	k = 2	0.6473 ± 0.0140	0.0876 ± 0.0169	0.0647 ± 0.0006	0.0712 ± 0.0154
	k = 3	0.6633 ± 0.0166	0.0672 ± 0.0278	0.0652 ± 0.0025	0.0897 ± 0.0006
	k = 4	0.6380 ± 0.0164	0.0973 ± 0.0164	0.0641 ± 0.0005	0.0878 ± 0.0068
	k = 5	0.6518 ± 0.0140	0.0878 ± 0.0171	0.0658 ± 0.0011	0.0836 ± 0.0154
	k = 6	0.6445 ± 0.0106	0.1006 ± 0.0061	0.0636 ± 0.0017	0.0896 ± 0.0372
	k = 7	0.6446 ± 0.0180	0.0812 ± 0.0112	0.0664 ± 0.0016	0.0882 ± 0.0190
15	k = 1	0.6454 ± 0.0155	0.0855 ± 0.0212	0.0651 ± 0.0016	0.08561 ± 0.02057
	k = 2	0.6208 ± 0.0203	0.1067 ± 0.0244	0.0624 ± 0.0017	0.09077 ± 0.04168
	k = 3	0.6390 ± 0.0178	0.1027 ± 0.0311	0.0652 ± 0.0025	0.09318 ± 0.01034
	k = 4	0.6521 ± 0.0231	0.1020 ± 0.0174	0.0652 ± 0.0009	0.09352 ± 0.01016
	k = 5	0.6523 ± 0.0229	0.0989 ± 0.0310	0.0657 ± 0.0013	0.08864 ± 0.01785
	k = 6	0.6383 ± 0.0160	0.1038 ± 0.0531	0.0642 ± 0.0021	0.10713 ± 0.05581
	k = 7	0.6502 ± 0.0189	0.0839 ± 0.0257	0.0640 ± 0.0031	0.09791 ± 0.02531

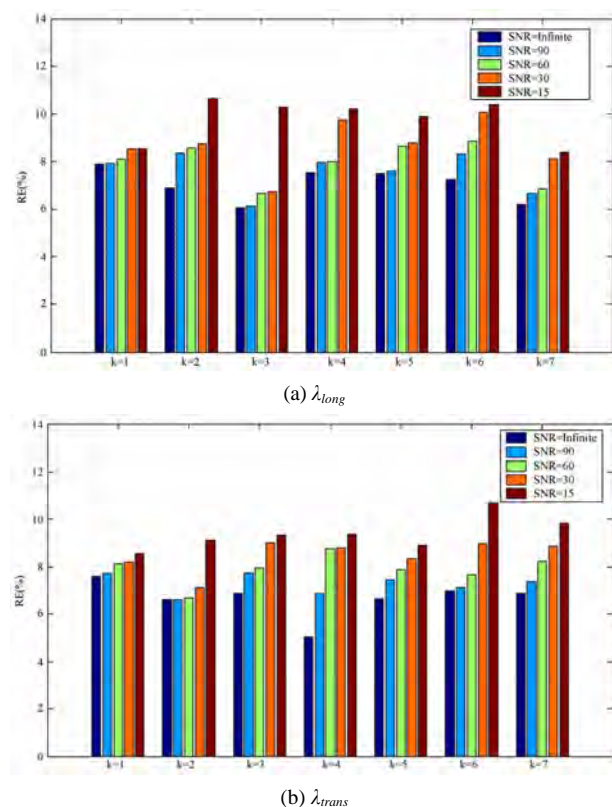


Figure 6. The REs at different current injected numbers with different noise levels ($\delta = [B_z]$).

Comparing the REs of results based on $\delta = \{B\}$ with five SNR noise levels, we can see that the REs using $\delta = [B_z]$ were relatively smaller than the other two results using $\delta = [B_z B_y]$ and $\delta = [B_z B_y B_x]$. Even under the condition that number k of the injected currents changed from 1 to 7, the same conclusion could be gained.

Figure 7 showed that the RBF-MREIT based on $\delta = [B_z]$ could accurately detect the eigenvalues of the anisotropic WM conductivity in the deep brain region. This was a desired outcome of RBF-MREIT algorithm applied on the human head tissues. The RBF-MREIT algorithm based on $\delta = [B_z]$ without rotation was practical in further experimental study and provided a potential means for reconstructing the complex conductivities of the human brain and clinic application.

4. DISCUSSION

The RBF-MREIT algorithm, which was used to reconstruct the piece-wise homogeneous conductivity of three layer head model in [20], was extended to estimate the eigenvalues of the WM. Viewed from the microscopic angle, the conductivities of the human head are different everywhere and anisotropic characteristic exists everywhere, even for the same tissue. Some research [6,28-30]

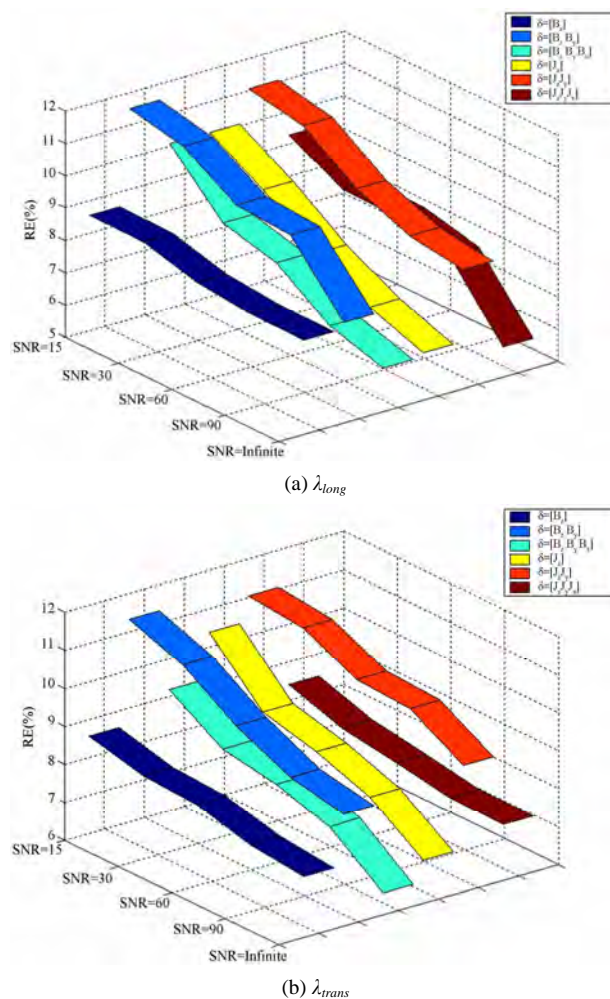


Figure 7. The REs based on different data $\delta = \{B, J\}$ with different noise levels ($k = 1$).

showed that the realistic head model with anisotropic and inhomogeneous conductivity could improve the accuracy of the source location in EEG/MEG analysis. Presently, the MREIT algorithms [20,21] were used in human head only under the condition of the piece-wise homogeneous conductivities of the tissues. Some other MREIT algorithms were not suitable to reconstruct the conductivities of the complex head tissues.

RBF-MREIT algorithm based on one component magnetic flux density solved the rotation problem in the MREIT research and had strong usability in the future clinic experiment. With different noise levels, all the REs of the reconstructed WM based on one component magnetic flux density B_z were less than 11%, which was acceptable for the resolution requirement of the EEG/MEG analysis. The simulation results suggested that the algorithm was insensitive to the measurement noise. The present simulation results demonstrated the feasibility of the RBF-MREIT algorithm for anisotropic conductivity

reconstruction of the human head tissues.

In summary, simulation results given above showed that the RBF-MREIT algorithm [20] extended to detect the eigenvalues of the anisotropic conductivity could reconstruct anisotropic WM conductivity distribution of the FEM human head model with high accuracy. The target anisotropic conductivity of the WM was set up based on the DT-MRI data according to the physical experiment measurement performed on a healthy human object. DT-MRI provides a noninvasive imaging modality to give more precise description of the human head tissues with anisotropic characteristic. So in our simulation, the head model considering the anisotropic tissues and based on the DT-MRI was reliable.

The target anisotropic conductivity defined in our research was based on Wolters' model [3,6], in which the eigenvalues of the anisotropic WM conductivity were assumed to be homogeneous. The model set up by Tuch [2,5] was more complicated than Wolters', the eigenvalues of the anisotropic conductivity at every element being not identical. Wang [7] proposed a multi-compartment anisotropic WM model incorporating the partial volume effects of the CSF and the intra-voxel fiber crossing structure, which gave more refined description through the physiology angle. All these models could be the target values of the anisotropic conductivity reconstruction for our next work.

The RBF-MREIT algorithm has certain limitations on the application for the reconstruction of the inhomogeneous conductivities, especially on the complex human head tissues. More unknown values will increase the complexity and extend the training time of the Radius Basic Function Neural Network for the inhomogeneous conductivity reconstruction. All these will have impacts on the accuracy and efficiency of the RBF-MREIT algorithm. So the new MREIT algorithm, which is applied to reconstruct the inhomogeneous conductivity including the anisotropic conductivities of the human head tissue, is our future research focus.

In the simulation, a current of 5 mA was used, which is thought to be the upper safe limit for human beings (IEC criterion). And for human head, it is a little higher. So it would be desirable to utilize a better MRI scanner, some denoising techniques and improved methods. The information of the electrical properties of head tissues is used for electroencephalographic source localization and functional mapping of brain activities and functions. It has been proved that the information about *vivo* tissue conductivity values impacts the solution accuracy of bioelectrical field problems [28-30]. In our future studies, researches will focus on the study of continuous conductivity distribution reconstruction of the head tissues and the experimental validation of the algorithm on the hu-

man head phantom experiment, as well as ways to reduce the amount of the injection current to less than 1mA for human security consideration in clinical experiment.

5. CONCLUSIONS

We proposed the extended RBF-MREIT approach [20] based on one component measured magnetic flux density to avoid the rotation procedure for the noninvasive imaging of the three-dimensional conductivity distribution of the brain tissues with anisotropic characteristic. In this paper, the FEM method was used to build a five-layer head model constructed from DT-MRI data. Simulations were performed on the FEM model to reconstruct the conductivities of anisotropic tissues. A series of computer simulation results demonstrate the feasibility, the fast convergence ability and the improved robustness against measurement noise of the algorithm. Therefore, it is potential to provide a more accurate estimate of the WM anisotropic conductivity, and may have important applications to neuroscience research or clinical applications in neurology and neurophysiology.

However, the anisotropic conductivity estimation of the WM tissue is more useful to obtain high resolution source localization and mapping results. EEG/MEG inverse solution provides a unique tool to localize neural electrical activity of a human brain from noninvasive electromagnetic measurements. And it has been proved that information about the *vivo* tissue conductivity values improves the solution accuracy of bioelectrical field problems. Moreover, literatures [3, 6] show that the anisotropic conductivities of the skull and WM may have impact on EEG/MEG analysis and sensitivity of the source location in the Early Left Anterior Negativity (ELAN) usage of the language processing.

REFERENCES

- [1] He, B. (2005) Neural engineering. Kluwer Academic Publishers, Norwell.
- [2] Haueisen, J., Tuch, D.S., Ramon, C., Schimpf, P.H., Wedeen, V.J., George, J.S. and Belliveau, J.W. (2002) The influence of brain tissue anisotropy on human EEG and MEG. *NeuroImage*, **15**(1), 159-166.
- [3] Wolters, C.H., Anwander, A., Tricoche, X., Weinstein, D., Koch, M.A. and MacLeod, R.S. (2006) Influence of tissue conductivity anisotropy on EEG/MEG field and return current computation in a realistic head model: A simulation and visualization study using high-resolution finite element modeling. *NeuroImage*, **30**(3), 813-826.
- [4] Basser, P.J., Mattiello, J. and Lebihan, D. (1994) MR diffusion tensor spectroscopy and imaging. *Biophysical Journal*, **66**(1), 259-267.
- [5] Tuch, D.S., Wedeen, V.J., Dale, A.M., George, J.S. and Belliveau, J.W. (1999) Conductivity tensor mapping of

- the human brain using diffusion MRI. *Annals of the New York Academy of Sciences*, **888**, 314-316.
- [6] Wolters, C.H. (2002) Influence of tissue conductivity inhomogeneity and anisotropy on EEG/MEG based source localization in the human brain. Leipzig University, Leipzig.
 - [7] Wang, K., Zhu, S.A., Mueller, B., Lim, K., Liu, Z.M. and He, B. (2008) A new method to derive WM conductivity from diffusion tensor MRI. *IEEE Transactions on Biomedical Engineering*, **55**(10), 2481-2486.
 - [8] Goncalves, S., de Munck, J.C., Heethaar, R.M. and da Silva, F.L. (2003) *In vivo* measurement of the brain and skull resistivities using an EIT-based method and realistic models for the head. *IEEE Transactions on Biomedical Engineering*, **50**(6), 754-767.
 - [9] Lai, Y., van Drongelen, W., Ding, L., Hecox, K.E., Towle, V.L., Frim, D.M. and He, B. (2005) Estimation of *in vivo* human brain-to-skull conductivity ratio from simultaneous extra- and intra-cranial electrical potential recordings. *Clinical Neurophysiology*, **116**(2), 456-465.
 - [10] Birgül, Ö., Eyüboğlu, B.M. and İder, Y.Z. (2003) Current constrained voltage scaled reconstruction (CCSVR) algorithm for MR-EIT and its performance with different probing current patterns. *Physics in Medicine and Biology*, **48**, 653-671.
 - [11] İder, Y.Z. and Birgül, Ö. (1998) Use of the magnetic field generated by the internal distribution of injected currents for electrical impedance tomography (MR-EIT). *Elektrik, Turkish Journal of Electrical Engineering and Computer Sciences*, **6**(3), 215-225.
 - [12] Khang, H.S., Lee, B.I., Oh, S.H., Woo, E.J., Lee, S.Y., Cho, M.H., Kwon, O., Yoon, J.R. and Seo, J.K. (2002) J-substitution algorithm in magnetic resonance electrical impedance tomography (MREIT): Phantom experiments for static resistivity images. *IEEE Transactions on Medical Imaging*, **21**(6), 695-702.
 - [13] Kwon, O., Lee, J.Y. and Yoo, J.R. (2002) Equipotential line method for magnetic resonance electrical impedance tomography (MREIT). *Inverse Problems*, **18**(2), 1089-1100.
 - [14] Özdemir, M.S., Eyüboğlu, B.M. and Özbek, O. (2004) Equipotential projection-based magnetic resonance electrical impedance tomography and experimental realization. *Physics in Medicine and Biology*, **49**(20), 4765-4783.
 - [15] Seo, J.K., Yoon, J.R., Woo, E.J. and Kwon, O. (2003) Reconstruction of conductivity and current density imaging using only one component of magnetic field measurements. *IEEE Transactions on Biomedical Engineering*, **50**(9), 1121-1124.
 - [16] Oh, S.H., Lee, B.I., Woo, E.J., Lee, S.Y., Cho, M.H., Kwon, O. and Seo, J.K. (2003) Conductivity and current density image reconstruction using harmonic Bz algorithm in magnetic resonance electrical impedance tomography. *Physics in Medicine and Biology*, **48**(19), 3101-3116.
 - [17] Oh, S.H., Lee, B.I., Woo, E.J., Lee, S.Y., Kim, T.S., Kwon, O. and Seo, J.K. (2005) Electrical conductivity images of biological tissue phantom in MREIT. *Physiological Measurement*, **26**(2), S279-S288.
 - [18] İder, Y.Z. and Onart, S. (2004) Algebraic reconstruction for 3D magnetic resonance-electrical impedance tomography (MREIT) using one component of magnetic flux density. *Physiological Measurement*, **25**(1), 281-294.
 - [19] Park, C., Kwon, O., Woo, E.J. and Seo, J.K. (2004) Electrical conductivity imaging using gradient Bz decomposition algorithm in magnetic resonance electrical impedance tomography (MREIT). *IEEE Transactions on Medical Imaging*, **23**(3), 388-394.
 - [20] Gao, N., Zhu, S.A. and He, B. (2005) Estimation of electrical conductivity distribution within the human head from magnetic flux density measurement. *Physics in Medicine and Biology*, **50**(11), 2675-2687.
 - [21] Gao, N., Zhu, S.A. and He, B. (2006) A new magnetic resonance electrical impedance tomography (MREIT) algorithm: the RSM-MREIT algorithm with applications to estimation of human head conductivity. *Physics in Medicine and Biology*, **51**(12), 3067-3083.
 - [22] Gao, N. and He, B. (2008) Noninvasive imaging of bioimpedance distribution by means of current reconstruction magnetic resonance electrical impedance tomography. *IEEE Transactions on Biomedical Engineering*, **55**(5), 1530-1539.
 - [23] Birgül, Ö. and İder, Y.Z. (1998) Use of magnetic field generated by the internal distribution of injected currents for electrical impedance tomography (MREIT). *Elektrik*, **6**(3), 215-225.
 - [24] Seo, J.K., Pyo, H.C., Park, C., Kwon, O. and Woo, E.J. (2004) Image reconstruction of anisotropic conductivity tensor distribution in MREIT: Computer simulation study. *Physics in Medicine and Biology*, **49**(18), 4371-4382.
 - [25] Zhang, Y.C., van Drongelen, W. and He, B. (2006) Estimation of *in vivo* brain-to-skull conductivity ratio in humans. *Applied Physics Letters*, **89**(22), 223903-223903.
 - [26] Yao, Y., Zhu, S.A. and He, B. (2005) A method to derive FEM models based on BEM models. *IEEE 27th Annual International Conference, Engineering in Medicine and Biology Society (EMBS)*, Shanghai, 1-4 September 2005, 1575-1577.
 - [27] Scott, G.C., Joy, M.L.G. and Armstrong, R.L. (1992) Sensitivity of magnetic-resonance current-density imaging. *Journal of Magnetic Resonance*, **97**(2), 235-254.
 - [28] Awada, K.A., Jackson, D.R., Baumann, S.B., Williams, J.T., Wilton, D.R., Fink, P.W. and Prasky, B.R. (1998) Effect of conductivity uncertainties and modeling errors on EEG source localization using a 2-D model. *IEEE Transactions on Biomedical Engineering*, **45**(9), 1135-1145.
 - [29] Ferree, T.C., Eriksen, K.J. and Tucker, D.M. (2000) Regional head tissue conductivity estimation for improved EEG analysis. *IEEE Transactions on Biomedical Engineering*, **47**(12), 1584-1592.
 - [30] Gençer, N.G. and Acar, C.E. (2004) Sensitivity of EEG and MEG measurements to tissue conductivity. *Physics in Medicine and Biology*, **49**(5), 707-717.

Categorizing HIV-1 subtypes using an ant-based clustering algorithm

David King*, Wei Hu

Department of Computer Science, Houghton College, Houghton, USA.
Email: David.King@Houghton.edu

Received 28 May 2010; revised 17 June 2010; accepted 22 June 2010.

ABSTRACT

Human Immunodeficiency Virus (HIV) is especially difficult to treat due to its rapid mutation rate. There are currently eleven different genomic subtypes of HIV-1, as well as a number of recombinant subtypes. An area of study in bioinformatics is the development of algorithms to identify the subtypes of HIV-1 genomes. Ant-based algorithms have the ability to find global solutions in optimizations problems, and are also able to process complex data efficiently. We proposed a new technique named Ant Colony Anchor Algorithm (ACAA), using anchors of training data on a topographic map to categorize HIV-1 sequences based on ant-based clustering. We used three sets of sequences from the POL region of the HIV-1 genome. We categorized these three dataset with the Subtype Analyzer (STAR), a current HIV-1 categorization algorithm, and the ACAA. We found that the ACAA returned higher accuracy values of 83.2%, 67.1%, and 53.5% for our three datasets respectively, than the STAR's 47.3%, 49.4% and 18%. The results of the ACAA are the average results of 20 runs of the algorithm. We also observed the performance of the algorithm on specific subtypes, and observed that while the STAR and ACAA performed with similar accuracy on several subtypes (A, B, and C in particular), the ACAA had a significant advantage over the STAR in others, especially in categorizing recombinant subtypes.

Keywords: Ants; Clustering; HIV; Classification; Subtype; STAR; ATTA; Bioinformatics

1. INTRODUCTION

1.1. HIV-1 Subtype Categorization

Human Immunodeficiency Virus (HIV), which causes Acquired Immunodeficiency Syndrome (AIDS), falls into two broad categories: HIV-1 and HIV-2. HIV-2 is largely constrained to West Africa, and has a relatively

lower transmission rate. HIV-1, on the other hand, has a very high transmission rate, and accounts for most HIV infections on a global scale.

Treatment of HIV-1 is a difficult process because of the virus' exceptionally high mutation rate. When DNA is replicated in the reproductive cycle of the virus, anywhere between 1 in 1000 and 1 in 10000 nucleotides will be improperly transcribed. This has lead to an exceptionally diverse pool of viruses, genetically speaking. HIV-1 has been classified into 11 subtypes based on genomic patterns and variations (subtypes A-H, J, N, and O).

Additionally, there are recombinant types of these viruses, which contain combined DNA from two or more viruses. These recombinant subtypes are caused by the infection of a single cell by multiple viruses [1].

There is neither a cure for HIV-1 nor a preventative vaccine. Antiretroviral drugs have been shown to be an effective treatment. These drugs interfere with the DNA of the virus. As such, the genetic makeup of the virus has tremendous effect on its resistance to the treatments. Because the subtype has such a significant impact on the effectiveness of the drugs, categorization of different subtypes of HIV-1 is critical to the treatment process.

The development of an algorithm to effectively categorize HIV-1 is of prime interest in this area of study. One current categorization algorithm is the STAR (Subtype Analyzer), developed by University College London Centre for Virology. The STAR functions by maintaining profiles of these 11 categories. These profiles are calculated based on aligned training sequence data. Each profile is a two-dimensional frequency matrix, where the number of rows in the matrix is the length of the training sequences in amino acid positions, and the number of columns is 20—one for each possible amino acid. These profiles are calculated based on training sequence data, where each position in a subtype profile is the frequency of that particular amino acid at that position in all training sequences of that subtype. A global profile matrix is

also calculated, using the amino acid frequency from all training sequences rather than just a single subtype [1].

Each test sequence to be categorized receives a Z-score based on each subtype profile. The test sequence is categorized as the subtype which gives the score closest to the mean. If the sequence is not within 1.5 standard deviations of the mean for any of the subtypes, the virus is categorized into the lump category, 'unassigned' [1]. This is not an innately helpful category; however neither is it innately harmful. It is preferred to leave a sequence unclassified rather than misclassified.

There are other algorithms, similar in nature to the STAR, which have also been turned towards the purpose of subtype categorization. The SUDI algorithm¹, developed by Los Alamos National Laboratory, uses phylogenetic analysis to determine subtype. The HIV Genotyping algorithm², developed by NCBI uses both a similarity search as well as a bootscanning similarity process to categorize subtypes. Stanford's HIVseq³ algorithm categorizes based only on a simple similarity search [2].

1.2. Ant-Based Clustering Algorithms

Ant-based algorithms fall under a category of algorithms which model their behavior from ants in the wild. These algorithms have found effective applications in bioinformatics because of their ability to find global solutions in optimization problems, as well as for their ability to efficiently process complex data quickly [3].

Ant-based clustering algorithms refer specifically to those algorithms which model the clustering behavior of ants in the wild. The behavior of these social insects displays a high level of swarm intelligence. In this instance, the habits of many relatively simple individuals form a pattern of behavior with distinct order and purpose. In the same way that real ants will cluster objects into like piles within a space (e.g., within a colony, eggs will be clustered into one chamber, while food will be clustered into another), the algorithm will cluster like pieces of data into the same area on a two-dimensional topographic map, forming clusters. Clustering data on a two dimensional map can greatly reduce the dimensionality which needs to be analyzed, allowing for much more efficient analysis and evaluation than would be possible with the raw data [4].

Ant-based clustering algorithms were originally proposed in 1991 by Deneubourg *et al.* [5], and were designed to emulate the sorting and clustering behaviors of

ants. Early algorithms of this variety were ineffective, but showed enough potential for clustering data that new improvements continued to occur [3].

One such improvement, called ATTA (Adaptive Time-dependent Transporter Ants), was proposed by Julia Handl [3], and is effective at clustering like data points on a two dimensional map. A sample output of the ATTA can be seen in **Figure 1**. The ATTA utilized formulae which were altered from those used in previous algorithms. Several other changes were made to the process of the algorithm which increased the ability of the algorithm to produce a distinct clustering [6].

The goal of this study is to develop a new algorithm based on the ATTA to categorize HIV-1 subtypes, and to compare the performance of our algorithm with that of the STAR (<http://www.vgb.ucl.ac.uk/starn.shtml>).

2. DATA

2.1. HIV-1 Sequence Data

An analysis of the STAR algorithm used sequence data which includes the entire protease region of the HIV-1 genome and 340 amino acids of the reverse transcriptase (RT), making for a total sequence length of 439. The protease and RT regions of HIV-1 play a role in the reproductive cycle of the virus. Common antiretroviral treatments interfere with the functions of these regions. Because of their medical significance, sequence data of

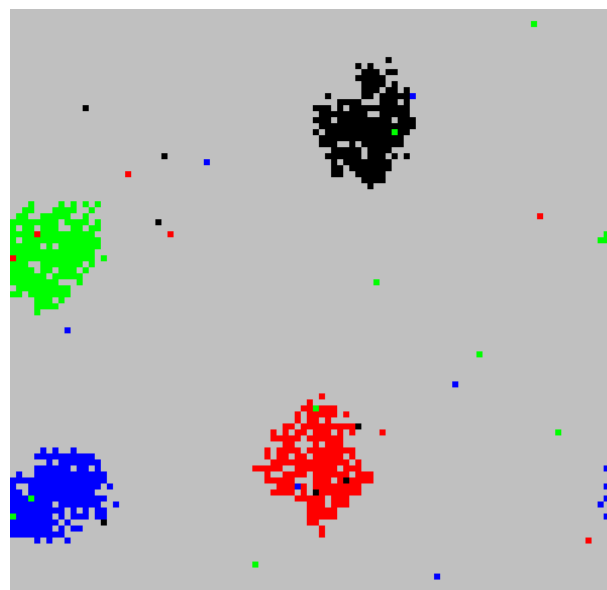


Figure 1. ATTA. This is visual representation of the ATTA. To generate this plot, 800 two-dimensional vectors were generated, each containing values close (within a vector distance of 1) to one of the points [2, 2], [2, 8], [8, 2] or [8, 8]. The points were assigned colors based on which of the four points they were associated with, then clustered using the ATTA.

¹<http://www.hiv.lanl.gov/content/hiv-db/SUDI/sudi.html>

²<http://www.ncbi.nih.gov/projects/genotyping/>

³<http://hivdb.stanford.edu/>

protease and RT has a high availability, making them prime for use in categorization algorithms [1]. In this study, we used three datasets, each covering different subtypes and different portions of these genomic regions.

Dataset 1 contained sequences of the same 439 amino acid region as in Myers *et al.* [1]. We include data from 8 subtypes (**Table 1**). We obtained these sequences from the Los Alamos National Laboratory HIV Sequence Database. Each subtype contained no more than 50 sequences and no less than 35.

Dataset 2 contained sequences of a shorter length: 99 amino acids from the protease, and only 240 amino acids from the RT (339 amino acids total, nucleotide positions 2253 to 3270). These were also downloaded from the Los Alamos National Laboratory HIV Sequence Database. 10 subtypes were covered, with sequence numbers between 35 and 50 (**Table 1**).

Dataset 3 contained sequences of the protease genomic region (99 amino acids, ranging from nucleotide positions 2253 to 2550). These were downloaded from the Stanford drug resistance database. This dataset contained 10 subtypes (**Table 1**). Again, each data type had no more than 50 and no less than 35 sequences.

Because misaligned sequences can significantly reduce the effectiveness of sequence analysis, we performed a multiple alignment on all sequences in each dataset using the ClustalW2 algorithm.

In each dataset, every subtype was separated into training and test data. For the purposes of consistency, we used 30 sequences as training data for every subtype. All other sequences (between 5 and 20 in number) were used as test data to be categorized.

All datasets are available on request from the author.

2.2. HIV-1 Sequence Encoding

Each dataset was a collection of sequenced HIV-1 genomes. Each sequence consisted of a list of amino acids. In order to properly analyze these sequences, we converted each into a binary vector. Because there are twenty different possible amino acids, we mapped each amino acid to a unique twenty-dimensional binary vector. For example, we mapped the amino acid Alanine to the point [1, 0, 0, 0, 0...], while we mapped Arginine to [0, 1, 0, 0, 0...]. After all the amino acids in a sequence were converted, we concatenated these individual vectors into

an ordered, high-dimensional sequence vector, with dimensionality of 20N, where N is the number of amino acids in the sequence. In this manner, each unique amino acid was represented in the sequence vector.

3. METHODS

3.1 The ATTA Algorithm

The ATTA takes as input a collection of vectors, called documents—a term used by the ATTA. These documents are distributed randomly across a two dimensional grid called a topographic map. The vector data of the documents bears no relation to their initial coordinates on the topographic map. The goal of the algorithm is to cluster the documents on the topographic map such that the documents which are similar to one another will be located near one another on the map.

The ants are simple entities which have the ability to wander freely across the map. They are able to pick up, carry, and drop documents as the algorithm runs. The probability that a document is picked up or dropped by an ant is dependent on the nearby documents.

For each iteration of the algorithm, a random ant from the colony is chosen. The ant moves to a different location on the map within a user-defined distance (our maximum movement distance was 50). At the beginning of the algorithm, this movement is randomly generated, but later is based partially on previous movements of that ant. The ant attempts to drop the document it is carrying based on a probability calculated from the *pdrop* formula. If the drop action is successful, the ant will choose a new document at random, and attempt to pick with a probability calculated from the *ppick* formula. If this operation is unsuccessful, the ant will choose another document at random, and try again. This continues until the ant has successfully picked a new document [3].

The *ppick* and *pdrop* formulae are defined as:

$$ppick = \begin{cases} 1.0 & \text{if } f^*(i)^2 \leq 1 \\ \frac{1}{f^*(i)^2} & \text{else} \end{cases}$$

$$pdrop = \begin{cases} 1.0 & \text{if } f^*(i)^2 \geq 1 \\ f^*(i)^4 & \text{else} \end{cases}$$

Table 1. This table contains the subtypes used for each dataset, as well as the number of test data sequences for each subtype. Any subtype with the heading N/A was not included in that dataset.

Subtype	A	B	C	D	F	F1	G	J	K	O	U	AE	AG
Dataset 1	20	20	20	20	N/A	7	19	N/A	N/A	N/A	N/A	20	20
Dataset 2	20	20	20	20	N/A	20	20	N/A	N/A	8	10	20	20
Dataset 3	20	20	20	20	20	N/A	20	20	20	N/A	N/A	20	20

where

$$f^*(i) = \begin{cases} \frac{1}{\sigma^2} \sum_J \left(1 - \frac{\delta(i, j)}{\alpha}\right) & \text{if } f^*(i) > 0 \wedge \forall j \left(1 - \frac{\delta(i, j)}{\alpha}\right) > 0 \\ 0 & \text{otherwise} \end{cases}$$

where i is the candidate document, σ is the neighborhood size, J is the set of documents in the neighborhood, j is the current document in J , $\delta(i, j)$ is the vector distance between document i and document j , and α is a user-defined constant. It is important to note that since the vector information of all documents is constant, $\delta(i, j)$ need only be calculated once for all possible document pairs. Because the algorithm merely references pre-calculated values, it is able to process even high dimensional vectors very efficiently.

The value of f^* becomes larger as i becomes more similar with the other elements in J . As such, $ppick$, which has an inverse relation to f^* , becomes smaller as f^* increases, leading to a dramatically decreased likelihood that the element is picked up when it is nearby similar elements. By contrast, $pdrop$ skyrockets when f^* increases, leading to a very high likelihood that an element will be dropped amongst like elements. These formulae are specific to the ATTA, and are revised from those used in previous ant-based clustering algorithms [7].

In this manner, after a large number of successive iterations, the documents with similar vectors are likely to have similar Euclidian positions, forming clusters of like documents on the map.

The output of the ATTA is a clustering of the input vectors. The quality of these clusters is measured by a Pearson Correlation, which evaluates the correlation between the distances of two documents on the topographic map and the distances between the vectors of the two documents [7].

3.2 Modifications to the ATTA

The ATTA is a clustering algorithm, not originally intended for categorization purposes. Where the ATTA takes in all documents at once, and clusters them all in the same manner, categorization algorithms build a classifier based on training data, and then apply the classifier to the test data to categorize. Using the ATTA as a base, we built a categorization algorithm to categorize input test sequences using a classifier build from training sequences.

Our classifier takes the form of anchors of training data in fixed positions on the topographic map. We assign each subtype of training data a unique square region on the topographic map, called the anchor area. The

Euclidian positions of the training documents are fixed.

This anchoring technique ensures that the training documents of each subtype are well separated, and will not move through the clustering phase of the algorithm. As a result, the ants will tend to drop test documents of a given subtype near the pre-defined anchor of the same subtype. We call this the Ant Colony Anchor Algorithm (ACAA). A sample output of the ACAA is visible in **Figure 2**. The pseudo-code for the ACAA is available in Section 1 of the supplementary file.

3.3 Subtype Categorization Based on Clustering

When running the ACAA on HIV-1 sequences, we converted each sequence to a binary vector as in Subsection 2.2. Each document in the ACAA represents one HIV-1 sequence.

After the clustering process of the ACAA is finished, we defined a local area for each test document. The radius of this local area was one half the width of the anchor areas. Each test document was classified as the subtype which has the highest representation of training documents within the test document's local area. This is a modified version of the classification strategy used in the study by Lee *et al.* [8].

Because the ACAA is non-deterministic, we utilized repetition to stabilize the results of the categorization. We recorded each test sequence's predicted subtype in each repetition of the ACAA. There are a total of 20 repetitions in our experiment—further repetitions did not

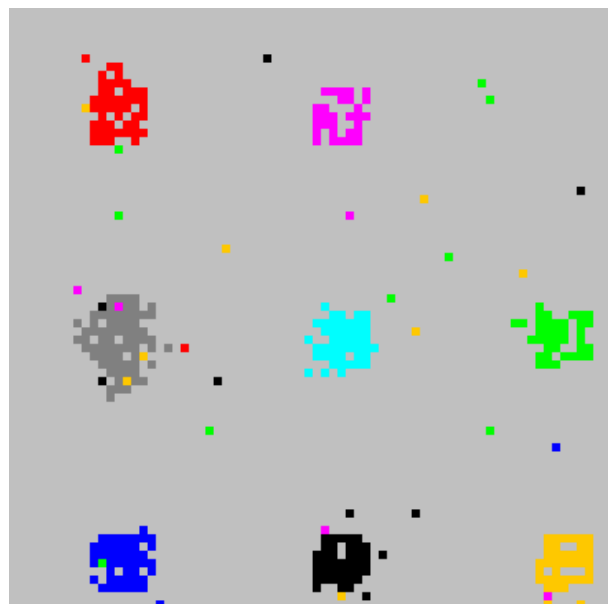


Figure 2. ACAA. This figure clearly shows the anchors of training data on the topographic map, with test data clustering around the training anchors of appropriate type.

improve performance significantly. The final categorization is based on majority votes.

4. RESULTS

We categorized our test data using the ACAA and the STAR's online interface. For each dataset, we maintained a record of the number of sequences correctly classified, the number incorrectly classified, and the number left unclassified.

The STAR is deterministic in nature, and so the categorization was only run a single time. Because the ACAA is non-deterministic in nature, we ran the algorithm on each dataset twenty times, taking the average values of the twenty runs. We also recorded the individual run which produced the highest rate of correct categorization (**Table 2**).

The ACAA yields a more accurate classification than the STAR for all datasets. For the ACAA, the lengthier Dataset 1 yields the best results, while Dataset 2 still gives reasonable accuracy. The STAR was able to categorize both Datasets 1 and 2 with approximately the same level of accuracy. In both the STAR and the ACAA, the categorization of Dataset 3 was not very successful, although the ACAA did categorize with a much higher accuracy than the STAR.

In all datasets, we observe that the ratio of inaccuracy to unclassified sequences is higher in our algorithm than in the STAR. In addition, in Datasets 2 and 3, we observe a higher number of misclassified sequences in the ACAA than in the STAR.

The statistical significance of these results is undeni-

able—every accuracy rating of the ACAA had a P-value of 0.0. The accuracies generated by the STAR had P-values of 0.0 for Datasets 1 and 2, and 0.004 for Dataset 3.

The statistical significance was determined by generating 10,000 randomized classification predictions for each dataset, and comparing the accuracy of each against the accuracy of the prediction generated by the ACAA. The statistical significance was the percentage of randomly generated predictions with accuracies greater than those produced by the ACAA.

In addition to analysis on each specific dataset, we also observed distinct differences in the ability of both algorithms to categorize specific subtypes. To measure this, we maintained records of the accuracy for each specific subtype in each dataset (**Table 3**).

In so doing, we observed that there are clear differences in how certain subtypes categorize. Typically the subtypes A-D are easier to categorize than others. The ACAA gives a more accurate classification on recombinant subtypes, especially AE. Other subtypes, particularly J, K, and U were problematic to classify in both instances.

We observed in both algorithms that, while the accuracy for some subtypes increased as sequence length increased, there were some subtypes which were more accurately categorized when the sequence length was shorter—the G subtype, for instance.

Overall, however, we find that the ACAA gives a more consistently accurate categorization for the subtypes used in this study than the STAR gives for all sequence lengths.

Table 2. Results of Analysis. This table shows a synopsis of the performance of the ACAA and STAR. Accuracy is the percentage of sequences correctly classified, inaccuracy is the percentage incorrectly classified, and unclassified is the number of sequences which were not assigned a category. The ACAA results are the average values from 20 runs of the algorithm, with the values in parentheses being the results of the run which.

	<i>STAR accuracy</i>	<i>STAR inaccuracy</i>	<i>STAR unclassified</i>	<i>ACAA accuracy</i>	<i>ACAA inaccuracy</i>	<i>ACAA unclassified</i>
Dataset 1	47.3%	16.4%	36.3%	83.2% (85.6%)	6.9% (6.1%)	10.1% (8.2%)
Dataset 2	49.4%	16.9%	33.7%	67.1% (70.2%)	19.9% (16.9%)	13.0% (12.9%)
Dataset 3	18%	17%	65%	53.5% (57%)	27.3% (30.5%)	19.2% (19.5%)

Table 3. Subtype specific Results. This table shows the accuracy for each subtype for both the ACAA and the STAR. Results of the ACAA are the average of the same twenty runs as used in **Table 2**.

Subtype	A	B	C	D	F	F1	G	J	K	O	U	AE	AG
Dataset 1													
ACAA	86.7%	97.7%	95%	78.2%	N/A	6.4%	46.8%	N/A	N/A	N/A	N/A	100%	100%
STAR	55%	95%	100%	5%	N/A	0%	21%	N/A	N/A	N/A	N/A	0%	80%
Dataset 2													
ACAA	82%	94.7%	49.5%	71.7%	N/A	55%	4.5%	N/A	N/A	100%	1%	100%	99%
STAR	75%	80%	55%	75%	N/A	0%	25%	N/A	N/A	100%	0%	0%	90%
Dataset 3													
ACAA	56.5%	91.2%	85.5%	37%	17.2%	N/A	75.7%	27.2%	8%	N/A	N/A	65%	71.2%
STAR	60%	0%	80%	15%	0%	N/A	25%	5%	0%	N/A	N/A	0%	0%

5. SUMMARY

We proposed to use ant-based clustering as a method to categorize HIV-1 sequences according to subtype. We developed the ACAA algorithm to utilize the approach of anchoring test data on a topographic map in order to categorize test data.

We ran our algorithm on three distinct datasets, containing varied HIV-1 subtypes and sequence lengths. For comparison, we also ran the STAR algorithm, a previously developed algorithm for HIV-1 subtype classification, on each dataset.

We have demonstrated increased accuracy of the ACAA algorithm over the STAR algorithm based on HIV-1 subtype classification. Our results imply that the ACAA is a viable alternative for the algorithmic classification of binary vector-based data.

6. ACKNOWLEDGEMENTS

We would like to thank Julia Handl for providing the original java code of the ATTA, and also for her quick and helpful responses to our enquiries about the code.

We would also like to thank Thomas Leitner of the Los Alamos National Laboratories HIV Database, who also responded to queries in an expedient and helpful manner.

REFERENCES

- [1] Myers, E.R., *et al.* (2005) A statistical model for HIV-1 sequence classification using the subtype analyzer (STAR). *Bioinformatics*, **21**(17), 3535-3540.
- [2] Oliveira, T., *et al.* (2005) An automated genotyping system for analysis of HIV-1 and other microbial sequences. *Bioinformatics*, **21**(19), 3797-3800.
- [3] Handl, J. (2003) Ant-based methods for tasks of clustering and topographic mapping: Improvements, evaluation and comparison with alternative methods. Ph.D. Thesis, Friedrich-Alexander University, Erlangen-Nürnberg.
- [4] Chen, L., *et al.* (2004) An adaptive ant colony clustering algorithm. *Proceedings of the 3rd International Conference on Machine Learning and Cybernetics*, Shanghai, 26-29 August 2004, 1387-1392.
- [5] Deneubourg, J.L., *et al.* (1991) The dynamics of collective sorting: Robot-like ants and ant-like robots. *Proceedings of the 1st International Conference on Simulation of Adaptive Behavior: From Animals to Animats*, MIT Press, Cambridge, **1**, 356-365.
- [6] Handl, J., *et al.* (2004) Strategies for increased robustness of ant-based clustering. *Engineering Self-Organising Systems (Lecture Notes in Computer Science)*, **2977**, 90-104.
- [7] Handl, J., *et al.* (2004) Ant-based clustering and topographic mapping. *Artificial Life*, **12**(1), 35-61.
- [8] Lee, M., *et al.* (2007) An ant-based clustering system for knowledge discovery in DNA chip analysis data. *Proceedings of World Academy of Science, Engineering and Technology*, **32**, 261-266.

Innovative data mining approaches for outcome prediction of trauma patients

Eleni-Maria Theodoraki¹, Stylianos Katsaragakis², Christos Koukouvinos³, Christina Parpoula³

¹Department of Statistics and Actuarial-Financial Mathematics, University of the Aegean, Samos Island, Greece;

²First Propaedeutic Surgery Clinic, Hippocratio Hospital, Athens, Greece;

³Department of Mathematics, National Technical University of Athens, Athens, Greece.

Email: parpoula.ch@gmail.com

Received 7 June 2010; revised 17 June 2010; accepted 23 June 2010.

ABSTRACT

Trauma is the most common cause of death to young people and many of these deaths are preventable [1]. The prediction of trauma patients outcome was a difficult problem to investigate till present times. In this study, prediction models are built and their capabilities to accurately predict the mortality are assessed. The analysis includes a comparison of data mining techniques using classification, clustering and association algorithms. Data were collected by Hellenic Trauma and Emergency Surgery Society from 30 Greek hospitals. Dataset contains records of 8544 patients suffering from severe injuries collected from the year 2005 to 2006. Factors include patients' demographic elements and several other variables registered from the time and place of accident until the hospital treatment and final outcome. Using this analysis the obtained results are compared in terms of sensitivity, specificity, positive predictive value and negative predictive value and the ROC curve depicts these methods performance.

Keywords: Data Mining; Medical Data; Decision Trees; Classification Rules; Association Rules; Clusters; Confusion Matrix; ROC

1. INTRODUCTION

One of the most common and rapidly growing causes of death and disability worldwide, regardless of each country's development level, is traumatic injury [2]. Every day 16,000 people die [3] and trauma is the leading cause of death in the age of 44 years [4] and the fourth leading cause of all ages after cardiovascular, neoplastic, and respiratory diseases. In 1996 the National Academy of Sciences and National Research Council published a report which characterized the injury as the "neglected disease of the modern world".

Due to technological advancements in healthcare domain, an enormous amount of data has been collected over the last few years. This fact is followed by clinician's willingness to explore different technologies and methodologies to analyze these data because their assessment may lead to trends and patterns within the data previously unknown which could significantly enhance their understanding of disease management. Interest in developing prognostic models for binary outcomes has emerged as an essential tool for evaluation of medical treatment. Multiple models exist to assist with prediction of the outcome of injured patients and many comparisons between different methods exist [4]. Traditionally, researchers have used the regression techniques which are not ideal in handling multidimensional, complex biologic data stored in large databases and are time consuming. Therefore, due to the fact that there is no consensus as to an optimal method, it is interesting to explore different methods.

Data mining methods were developed to overcome these limitations. With these techniques, a priori knowledge of variable associations is unnecessary. In contrast to an a priori approach to the selection of predictor variables, data mining allows the discovery of previously unknown variable relationships by exploring a wide range of possible predictor variables. The process of data mining is to find hidden patterns and associations in the data. The utility of data mining methods to derive medical prognostic models from retrospective data, can contribute to increased availability and volume of medical data gathered through systematic use of laboratory, clinical and hospital information systems. Also, it can lead to construction of interpretable prognostic models, handling of noise and missing values, and discovery and incorporation of non-linear patterns and feature combinations.

This paper investigates the utility of machine learning techniques to construct outcome prediction models

for severe trauma patients and examines measures that will improve the quality of treatment and therefore survivability of patient through optimal management. The study is organized as follows. Section 2 introduces the dataset that was used to investigate the plausibility of modeling the outcome. Statistical methods used for that purpose were classification, association and clustering algorithms. The results of data analysis, and their evaluation according to their predictive ability are reported in Section 3. Section 4 summarizes the results and provides conclusion of the paper.

2. MATERIALS AND METHODS

2.1. Patient Population and Variables

Our database consisted of cases collected during the project, entitled "Report of the epidemiology and management of trauma in Greece", which was initiated in October 2005 and lasted for twelve months. Study included patients from a range of 30 teaching, and general hospitals who were admitted with a primary diagnosis of injury. Information was gathered for these trauma patients admitted for at least one day in hospital. To avoid biasing estimates, persons who arrived dead or died at the Emergency Room of each hospital were excluded from the analysis. The data and injury scoring was performed by a highly-trained coordinator.

Input variables which were extracted and included to the models concerned demographics, mechanism of injury, month of admission to hospital, whether the patient was referred from another hospital, prehospital care, hospital care and procedures, and outcomes at discharge. Various injury severity scores were also considered including Injury Severity Score (ISS) [5], Abbreviated Injury Scores (AIS) [6], and the Glasgow Coma Score (GCS) [7]. For all models, there was a single output variable: probability of death.

Trauma registry was followed by extensive correction and verification of the data. During preprocessing analysis missing data were also handled. Despite the challenges inherent when data are missing, information could be gained when a thoughtful and systematic analytical approach is used [8]. For that purpose Multiple imputation (MI) was an appropriate method that was used to handle Missing At Random Data in our dataset [9] in order to minimize bias and increase the validity of findings. In this method, multiple (m) versions (typical range 5-20) of the data set are created using available data to predict missing values. These data sets are then used to conduct m analyses, which are then combined into one inferential analysis. The particular appeal of this method is that once completed data sets have been developed, standard statistical methods can be used. Adjusting multiple imputation issues to data mining meth-

ods, derived datasets were compared in terms of performance (correctly classified datasets) and the one with the most correctly classified training and test sets was chosen.

The analysis was carried out using the SPSS 17.0 and SPSS Clementine 12.0 statistical software.

2.2. Data Mining Algorithms

In this section, we present the data mining methods that were applied to analyze the trauma data. These methods may be categorized according to their goal as feature selection methods, decision tree learners, binary classifier comparison metrics, clustering algorithms and generalized rule induction algorithms.

2.2.1. Feature Selection

In order to reduce data set size, minimize the computational time and improve model accuracy, a set of variables selection criteria may be used. Such criteria are the maximum percentage of records in a single category criterion, as fields which have too many records falling into the same category may be omitted and the maximum number of categories as a percentage of records criterion, as if a high percentage of the categories contains only a single case, the field may be ignored. There are two more variable selection criteria, the minimum standard deviation criterion and the minimum coefficient of variation criterion. According to these, fields with standard deviation or respectively coefficient of variance less than or equal to the specified minimum measure may be of limited use. The coefficient of variance is defined as the ratio of the predictor standard deviation to the predictor mean.

A common technique used in data mining is ranking the attributes based on the measure of importance which is defined as $(1-p)$, where p is the p -value of a chosen statistical test such as the Pearson's chi-square statistic, the Likelihood-ratio chi-square statistic, the Cramer's V or Lambda statistic. More details can be found among others in [10-12] and [13]. The Pearson's chi-square statistical test, is a test of independence between X , where X is a predictor with I categories, and Y , where Y is the target value with J categories, that involves the difference between the observed and the expected frequencies. The expected cell frequencies under the null hypothesis

of independence are estimated by $\hat{N}_{ij} = \frac{N_{i.} N_{.j}}{N}$, where

N is the total number of cases, N_{ij} is the number of cases with $X = i$ and $Y = j$, $N_{i.}$ is the number of cases

with $X = i$ ($N_{i.} = \sum_{j=1}^J N_{ij}$) and $N_{.j}$ is the number of cases

with $Y = j$ ($N_{.j} = \sum_{i=1}^I N_{ij}$).

Under the null hypothesis, Pearson's chi-square converges asymptotically to a chi-square distribution χ_d^2 with degrees of freedom $d = (I - 1)(J - 1)$. Now, the p-value based on Pearson's chi-square X^2 is calculated by $\text{p-value} = \text{Prob}(\chi_d^2 > X^2)$, where

$$X^2 = \sum_{i=1}^I \sum_{j=1}^J (N_{ij} - \hat{N}_{ij})^2 / \hat{N}_{ij}.$$

2.2.2. Decision Trees

Decision tree models are a structural description which gives the opportunity to develop classification models that may be used to predict or classify future data sets, according to a number of provided decision rules. Future data with unknown classification may be classified just by routing down the tree according to the tests in nodes and assigning the class of the reached leaf. Some of the advantages of this approach are that it is easy understandable, can be transformed into a set of rules (if-then rules) that interpret the data set and finally that the provided tree includes only the important attributes that really contribute to the decisions making. The Classification and Regression Tree (C&RT) is a method based on recursive partitioning to split the training set into subsets so as to obtain more homogeneous subsets than in the previous step. The split is based on the reduction in an impurity index, and in this study we used the Gini index. CHAID algorithm, or Chi-square Automatic Interaction Detection, is based on the significance level of a statistical test and is a non-binary tree method, that is, it can produce more than two categories at any particular level in the tree. C5.0 algorithm works for data sets where the target field is categorical and builds decision tree by splitting the sample based on the field that provides the maximum information gain at each level.

2.2.3. Clustering

Clustering is concerned with grouping records with respect to similarity of values for a set of input fields without the profit of prior knowledge about the form and the characteristics of the groups.

K-means is an iterative algorithm which tries to discover k clusters, where (k) is defined by the user, so that records within a cluster are similar to each other and distinct from records in other clusters. There are different distance measures, such as Euclidean distance, Manhattan distance and Mahalanobis distance, but in our application we used the Euclidean distance.

The TwoStep cluster method is a scalable cluster analysis algorithm designed to handle very large data sets and both continuous and categorical variables or attributes. It requires only one data pass. It has two steps 1) pre-cluster the cases (or records) into many small sub-clusters 2) cluster the sub-clusters resulting from

pre-cluster step into the desired number of clusters. The TwoStep algorithm uses an hierarchical clustering method in the second step to assess multiple cluster solutions and automatically determine the optimal number of clusters for the input data. To determine the number of clusters automatically, TwoStep uses a two-stage procedure that works well with the hierarchical clustering method. In the first stage, the BIC (distance measure) for each number of clusters within a specified range is calculated and used to find the initial estimate for the number of clusters. TwoStep can use the hierarchical clustering method in the second step to assess multiple cluster solutions and automatically determine the optimal number of clusters for the input data.

2.2.4. Association Rules

Association rule mining finds interesting associations and/or correlation relationships among large set of data items. Association rules show attribute value conditions that occur frequently together in a given data set. A typical and widely-used example of association rule mining is Market Basket Analysis. Association rules provide information of this type in the form of if-then statements. These rules are computed from the data and, unlike the if-then rules of logic, association rules are probabilistic in nature. In association analysis the antecedent and consequent are sets of items (called itemsets) that are disjoint (do not have any items in common). In addition to the antecedent (the if part) and the consequent (the then part), an association rule has two numbers that express the degree of uncertainty about the rule. The first number is called the support for the rule. The support is simply the number of transactions that include all items in the antecedent and consequent parts of the rule. (The support is sometimes expressed as a percentage of the total number of records in the database). The other number is known as the confidence of the rule. Confidence is the ratio of the number of transactions that include all items in the consequent as well as the antecedent (namely, the support) to the number of transactions that include all items in the antecedent. Clementine uses Christian Borgelt's Apriori implementation. Unfortunately, the Apriori [14] algorithm is not well equipped to handle numeric attributes unless it is discretized during preprocessing. Of course, discretization can lead to a loss of information, so if the analyst has numerical inputs and prefers not to discretize them, may choose to apply an alternative method for mining association rules: GRI.

The GRI methodology can handle either categorical or numerical variables as inputs, but still requires categorical variables as outputs. Rather than using frequent item sets, GRI applies an information-theoretic approach to determine the interestingness of a candidate association

rule using the quantitative measure J . GRI uses this quantitative measure J to calculate how interesting a rule may be and uses bounds on the possible values this measure may take to constrain the rule search space. Briefly, the J measure maximizes the simplicity, goodness-of-fit trade-off by utilizing an information theoretic based cross-entropy calculation. Once a rule is entered in the table, it is examined to determine whether there is any potential benefit to specializing the rule, or adding more conditions to the antecedent of the rule. Each specialized rule is evaluated by testing its J value against those of other rules in the table with the same outcome, and if its value exceeds the smallest J value from those rules, the specialized rule replaces that minimum- J rule in the table. Whenever a specialized rule is added to the table, it is tested to see if further specialization is warranted, and if so, such specialization is performed and this process proceeds recursively. The association rules in GRI take the form If $X = x$ then $Y = y$ where X and Y are two fields (attributes) and x and y are values for those fields. The advantage of association rule algorithm over a decision tree algorithm is that associations can exist between any of the attributes. A decision tree algorithm will build rules with only a single conclusion, whereas association algorithms attempt to find many rules, each of which may have a different conclusion. The disadvantage of association algorithms is that they are trying to find patterns within a potentially very large search space and, hence, can require much more time to run than a decision tree algorithm.

2.2.5. Model Performance

After categorizing the features and inducing outcome prediction models, different statistical measures can be used to estimate the quality of derived models. In present study discrimination and calibration were calculated. The discriminatory power of the model (Classification accuracy (CA)) measures the proportion of correctly classified test examples, therefore the ability to correctly classify survivors and nonsurvivors. In addition, models were assessed for performance by calculating the Receiver-Operating-Characteristic (ROC) curves, constructed by plotting true-positive fraction versus the false-positive fraction and comparing the areas under the curves. Sensitivity and specificity measure the model's ability to "recognize" the patients of a certain group. If we decide to observe the surviving patients, sensitivity is a probability that a patient who has survived is also classified as surviving, and specificity is a probability that a not-surviving patient is classified as not-surviving. The Area under ROC curve (AUC) is based on a non-parametric statistical sign test and estimates a probability that for a pair of patients of which one has survived and the other has not, the surviving patient is given a greater

probability of survival. This probability was estimated from the test data using relative frequencies. A ROC of 1 implies perfect discrimination, whereas a ROC of 0.5 is equivalent to a random model. The above metrics and statistics were assessed through stratified ten-fold cross-validation [15]. This technique randomly splits the dataset into 10 subgroups, each containing a similar distribution for the outcome variable, reserving one subgroup (10%) as an independent test sample, while the nine remaining subgroups (90%) are combined for use as a learning sample. This cross-validation process continues until each 10% subgroup has been held in reserve one time as a test sample. The results of the 10 mini-test samples are then combined to form error rates for trees of each possible size; these error rates are applied to the tree based on the entire learning sample, yielding reliable estimates of the independent predictive accuracy of the tree. The prediction performance on the test data using cross-validation shows the best estimates of the misclassification rates that would occur if the classification tree were to be applied to new data, assuming that the new data were drawn from the same distribution as the learning data. Misclassification rates are a reflection of undertriage and overtriage, while correct classification of injured patients according to their need for TC or NTC care reflects sensitivity and specificity, respectively. Of the two misclassification errors, undertriage is more serious because of the potential for preventable deaths, whereas overtriage unnecessarily consumes economic and human resources.

Given a classifier and an instance, there are four possible outcomes. If the instance is positive (P) and it is classified as positive, it is counted as a true positive (TP); if it is classified as negative (N), it is counted as a false negative (FN). If the instance is negative and it is classified as negative, it is counted as a true negative (TN); if it is classified as positive, it is counted as a false positive (FP).

Given a classifier and a set of instances (the test set), a two-by-two confusion matrix (also called a contingency table) can be constructed representing the dispositions of the set of instances. A confusion matrix contains information about actual and predicted classifications done by a classification system. Performance of such systems is commonly evaluated using the data in the matrix. This matrix forms the basis for many common metrics. We will present this confusion matrix and equations of several common metrics that can be calculated from it for each training, validation and test set in our study. The numbers along the major diagonal represent the correct decisions made, and the numbers of this diagonal represent the errors, the confusion, between the various classes.

The common metrics of the classifier and the additional terms associated with ROC curves such as

- Sensitivity = $TP/(TP + FN)$
- Specificity = $TN/(FP + TN)$
- Positive predictive value = $TP/(TP + FP)$
- Negative Predictive value = $TN/(FN + TN)$
- Accuracy = $(TP + TN)/(TP + FP + FN + TN)$

are also calculated for each training, test and validation set.

3. RESULTS

Altogether, 8544 patients were recorded with 1.5% mortality rate (128 intrahospital deaths). The models were therefore trained with a dataset heavily favoured towards survivor. For each of them the binary response variable y (death: 1, otherwise: 0) is reported. There were approximately 780.000 data points (92 covariates, 8544 cases). In order to reduce the dimension of the problem we followed the procedure of feature selection, to execute and detect the most statistically significant of them, according to Pearson's chi-square. The final data set which is used for further analysis, included all of the 8544 available patients and the 36 selected factors (fields for data mining). The data set was divided randomly into three subsets: the training set, containing 50% of cases (t.i 4272), the test set, containing 25% of cases (2136) and validation set with 25% of cases (2136). After medical advice, all of the factors were treated equally during the data mining approach, meaning that there was no factor that should be always maintained in the model. Defining maximum percentage of records in a single category equal to 90%, maximum number of categories as a percentage of records equal to 95%, minimum coefficient of variation equal to 0.1 and minimum standard deviation equal to 0.0, we removed some factors of low importance. Moreover, applying the Pearson's chi-square statistic with respect to the categorical type of the target field and significance level $\alpha = 5\%$, we finally identified the 36 important variables displayed in C. Koukouvinos webpage, <http://www.math.ntua.gr/~ckoukou>.

There were no clear results from C&RT algorithm because it could not generate a rule set (condition too complex). The summary of C5.0 and CHAID model's predictive ability measured by percentages of correct classified records is displayed in **Table 1**. The percentage of records for which the outcome is correctly predicted, represents the overall accuracy of the examined method.

Tables 2, 3 and **4** display the confusion matrix for each set for C5.0 algorithm.

The metrics for the training set were: Sensitivity (84.6%), Specificity (98.4%), Positive predictive value (45.8%), Negative Predictive value (99.8%), Accuracy (98.9%).

The metrics for the test set were: Sensitivity (72.7%), Specificity (98.9%), Positive predictive value (26.6%), Negative Predictive value (99.8%), Accuracy (98.83%).

The metrics for the validation set were: Sensitivity

(64.28%), Specificity (99.2%), Positive predictive value (36%), Negative Predictive value (99.76%), Accuracy (98.97%).

The C5.0 tree may be converted into set of rules which are listed in **Table 5**. In each rule assigned the major classification of the corresponding node. Ruleset for 0 (life) contains 4 rules and ruleset for 1 (death) contains 3 rules.

Table 1. C5.0 and CHAID model's predictive ability.

Algorithm	Correctly classified		
	Training set	Test set	Validation set
C5.0	98.94%	98.84%	98.97%
CHAID	98.31%	98.6%	98.79%

Table 2. The confusion matrix for the training set for C5.0 algorithm.

Outcome	Training set	
	0(-) life	1(+) death
0(-) life	4178	6
1(+) death	39	33

Table 3. The confusion matrix for the test set for C5.0 algorithm.

Outcome	Test set	
	0(-) life	1(+) death
0(-) life	2113	3
1(+) death	22	8

Table 4. The confusion matrix for the validation set for C5.0 algorithm.

Outcome	Validation set	
	0(-) life	1(+) death
0(-) life	2111	5
1(+) death	17	9

Table 5. Ruleset for C5.0 algorithm.

IF	THEN
$x3 \leq 8.203$ and $x27$ in [0 1 2 3 4] and $x71 = 1$ and $x9 > 8.755$	life
$x3 \leq 8.203$ and $x27$ in [0 1 2 3 4] and $x71$ in [2 4]	life
$x3 \leq 8.203$ and $x27 = 5$ and $x26$ in [12 25 28 31]	life
$x3 > 8.203$	life
$x3 \leq 8.203$ and $x27$ in [0 1 2 3 4] and $x71 = 1$ and $x9 \leq 8.755$	death
$x3 \leq 8.203$ and $x27$ in [0 1 2 3 4] and $x71$ in [3 6]	death
$x3 \leq 8.203$ and $x27 = 5$ and $x26$ in [15 24]	death

Also the CHAID tree may be converted into set of rules which are listed in **Table 6**. In each rule assigned the major classification of the corresponding node. Rules for 0 (life) contains 14 rules.

Finally, we evaluated the performance of the aforementioned classification algorithms by means of ROC curves methodology, complemented by determination of the areas under the curves, as presented in **Table 7**.

We observe from the results derived from ROC curves methodology that CHAID algorithm has the biggest AUC = 0.888 which indicates an excellent performance of classifiers and a very good discriminating ability about the patient's outcome (life or death). C5.0 algorithm has the biggest value for the overall accuracy and a very satisfactory AUC = 0.709 which indicates a good performance of classifiers and a satisfactory discriminating ability about the patient's outcome. The C&RT algorithm has AUC = 0.5 which indicates a random performance of classifiers and an unreasonable discriminating ability to diagnose patients with and without the disease/condition. It is therefore natural not to trust the results of C&RT algorithm, as expected, from our previous effort to build a decision tree and a ruleset for C&RT where we observed that there were no clear results from the Clementine because it could not generate a rule set (conditions too complex). Generally, Classification algorithms were successful on trauma data set. The classification accuracy was especially high, reaching accuracy of 99% of correct classifications.

In **Figure 1** we present the evaluation of testing set for all the classification algorithms by means of ROC curves.

Table 6. Ruleset for CHAID algorithm.

IF	THEN
x71 = 1 and x3 ≤ 13.081	life
x71 = 1 and x3 > 13.081	life
x71 = 2 and x19 ≤ 3 and x50 = 0	life
x71 = 2 and x19 ≤ 3 and x50 = 1	life
x71 = 2 and x19 > 3 and x19 ≤ 3.945 and x50 = 0	life
x71 = 2 and x19 > 3 and x19 ≤ 3.945 and x50 = 1	life
x71 = 2 and x19 > 3.945 and x19 ≤ 4	life
x71 = 2 and x19 > 4 and x19 ≤ 4.888 and x11 ≤ 17827.408	life
x71 = 2 and x19 > 4 and x19 ≤ 4.888 and x11 > 17827.408	life
x71 = 2 and x19 > 4.888	life
x71 = 3 or x71 = 4	life
x71 = 6 and x3 ≤ 11.447	life
x71 = 6 and x3 > 11.447 and x28 = 0	life
x71 = 6 and x3 > 11.447 and x28 = 1	life

At clustering we specified as minimum number of clusters 2 and as maximum number of clusters 15 where we received detailed clustering of the records (distribution of variables with a percentage > 85% for its values). The clusters are obtained automatically from the performance of TwoStep algorithm, using only the most significant fields of the Trauma data set as they have been derived from feature selection algorithm. The number of clusters was 5 grouping 336, 914, 1227, 1050, 729 number of records.

For the clustering analysis, we performed additionally the K-means algorithm and we determined 5 clusters as default so that records within a cluster are similar to each other and distinct from records in other clusters, where we also received detailed clustering of the records. Five clusters are obtained from the performance of K-means algorithm, using only the most significant fields of the Trauma data set as they have been derived from feature selection algorithm. Each cluster contained 1280, 1010, 379, 935, 652 records.

Hence, we achieved the first goal of clustering, that is the decomposition of the data set into categories of similar data. Clusters are defined by their centers, where a cluster center is a vector of values for the input fields. Results deriving from clustering analysis, are reported as following: for discrete fields the mean value for training records assigned to each cluster is presented. For continuous fields we present only the major value of the variable, the major percentage which belongs to each cluster. Both algorithms gave identical rules. The TwoStep created the most multitudinous cluster containing

Table 7. Performance of the classification algorithms.

Algorithm	Area Under the Curve	
	Overall accuracy	AUC
CHAID	98.602	0.888
C5.0	98.835	0.709
C&RT	98.602	0.500

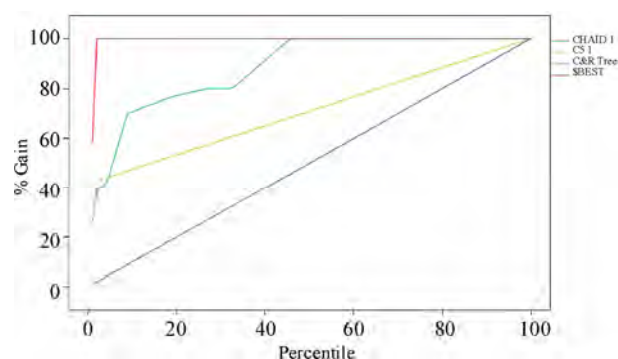


Figure 1. Evaluation of Testing set for CHAID, C5.0, C&RT algorithms.

1227 cases which were middle aged (50 years old on average, (o.a)), weighted 73.2 kg (o.a), had white cells 10537 (o.a), glucose levels 125 (o.a), creatinine 1.04 (o.a), urea 40 (o.a), good evaluation of disability (4.3, o.a), not severely injured (Injury Severity Score mean=6.2), high GCS (14.76, (o.a)), 84 pulses (o.a), systolic arterial pressure 130.5 (o.a), diastolic arterial pressure 77.5 (o.a), Ht 40 (o.a), Hb 13.4 (o.a). Additionally these patients were not pale (96.4%), had not epiphrosis (97.3%), had hydration with fluids (88.8%), had done radiography and CT (92.1%, 89.5% respectively), and were admitted to hospital clinic after the Emergency Room treatment (90.6%).

Using association rules, we performed the Generalized Rule Induction (GRI) algorithm in order to summarize patterns in the data using a quantitative measure for the interestingness of rules. The consequent (the “then” part of the rule) is restricted to being a single value assignment expression ($Y = 1$ death) while the antecedent (the “if” part of the rule) may be a conjunction of expressions of only the most significant fields of the Trauma data set as they have been derived from feature selection algorithm. Each rule in the final ruleset has associated support, confidence, based on the number of records for which the antecedent and the entire rule are true. Defining minimum antecedent support equal to 0%, minimum rule confidence equal to 50%, maximum number of antecedents equal to 3, maximum number of rules equal to 100 and choosing only true values for flags, resulted in the appearance only of the set of rules with consequent $y = 1$ death. Four association rules are obtained from the performance of GRI algorithm and this set of association rules is presented in **Table 8**.

According to the results derived from the implementation of GRI association rule, mortality is predicted with higher percent of support (1.03%) and confidence 60% when G.C.S (x3) is smaller than 6.

Moreover the model suggests with the highest confidence that people with a cutpoint of G.C.S under 6 although that are transferred to hospital with ambulance and they don't suffer from lower limbs injury they are predicted to die (Support: 0.96%, Confidence: 63.41%).

4. CONCLUSIONS

In conclusion, the selection of the most important factors

Table 8. Ruleset for GRI algorithm.

IF	THEN
$x3 < 5.97405$ and $x25 = 1$ and $x108 = 0$	death
$x3 < 5.97405$ and $x108 = 0$	death
$x3 < 5.97405$ and $x25 = 1$	death
$x3 < 5.97405$	death

determining the outcome of injured patients is critical, particularly when the problem is high dimensional. Therefore in order to detect the requested information, it is imperative to use expertise and cutting-edge statistical methods that would meet these needs. Data mining can be considered as an in-depth research to find information previously not seen in many of the collected data and has recently been used to medical data [16] often giving useful information for patterns. In our study, the results were encouraging because the implemented algorithms generated useful rules that are logical, consistent with the medical experience and provide more specific information which may assist as guidelines for trauma management. Specifically, we found that the CHAID and C5.0 algorithms offer an extensive knowledge of the classification of injuries including combinations of features that lead to death or good outcome. Also the K-mean and TwoStep algorithms produce casualties with common features and the classification is particularly interesting in the latter case where groups are not determined by the analyst. The comparison of data mining methods in terms of evaluation of medical diagnostic procedures for sensitivity, specificity, Positive Predictive value, Negative Predictive Value, confirmed that the extraction of data from a medical basis as this, may contribute to detect factors or combinations of factors that can predict reliably trauma patients outcome.

REFERENCES

- [1] The trauma audit and research network. <http://www.tarn.ac.uk/introduction/firstDecade.pdf>
- [2] Meyer, A. (1998) Death and disability from injury: A global challenge. *Journal of Trauma*, **44**(1), 1-12.
- [3] World Health Organization. <http://www.who.int/en/>
- [4] The trauma audit and research network. <http://www.tarn.ac.uk/content/downloads/36/firstdecade.pdf>
- [5] Baker, P., O'Neil, B., Haddon, W. and Long, B. (1974) The injury severity score: A method for describing patients with multiple injuries and evaluating emergency care. *Journal of Trauma*, **14**(3), 187-196.
- [6] Copes, W.S., Sacco, W.J., Champion, H.R. and Bain, L.W. (1990) Progress in characterising anatomic injury. *Proceedings of the 33rd Annual Meeting of the Association for the Advancement of Automotive Medicine*, Baltimore, 2-4 October 1989, 205-218.
- [7] Teasdale, G. and Jennett, B. (1974) Assessment of coma and impaired consciousness. A practical scale. *Lancet*, **2**(7872), 81-84.
- [8] Penny, K. and Chesney, T. (2006) Imputation methods to deal with missing values when data mining trauma injury data. *Proceedings of 28th International Conference on Information Technology Interfaces*, Cavtat, 19-22 June 2006, 213-218.
- [9] Donders, A.R., Van der Heijden, G.J., Stijnen, T. and Moons, K.G. (2006) Review: A gentle introduction to imputation of missing values. *Journal of Clinical Epi-*

- demology*, **59**(10), 1087-1091.
- [10] Cox, D.R. and Hinkley, D.V. (1974) Theoretical statistics. Chapman and Hall, London.
- [11] Cramer, H. (1946) Mathematical methods of statistics. Princeton University Press, Princeton.
- [12] Dobson, A. (2002) An introduction to generalized linear models. 2nd Edition, Chapman and Hall/CRC, London.
- [13] Pearson, R.L. (1983) Karl Pearson and the chi-squared test. *International Statistical Review*, **51**, 59-72.
- [14] Agrawal, R. and Srikant, R. (1994) Fast algorithms for mining association rules. *Proceedings of the 20th International Conference on Very Large Databases*, Santiago de Chile, 12-15 September 1994, 479-499.
- [15] Craven, P. and Wahba, G. (1979) Smoothing noisy data with spline functions: Estimating the correct degree of smoothing by the method of generalized cross-validation. *Numerische Mathematik*, **31**, 377-403.
- [16] Breault, J.L., Goodall, C.R. and Fos, P.J. (2002) Data mining a diabetic data warehouse. *Artificial Intelligence in Medicine*, **26**(1-2), 37-54.

Uncovering preferences from patient list data using benefit efficient models

Jan Ubøe, Jostein Lillestøl

The Norwegian School of Economics and Business Administration, Bergen, Norway.
Email: jan.uboe@nhh.no, jostein.lillestol@nhh.no

Received 11 September 2009; revised 1 June 2010; accepted 5 June 2010.

ABSTRACT

In this paper it is shown how the benefit efficient patient list model of Ubøe and Lillestøl [1] can be used to infer strength of preferences from patient list data. It is proved that the model allows the construction of unique sets of preferences replicating the observed allocations. To illustrate how this theory can be applied in practice, preferences are uncovered from a small data set, obtained from the Norwegian patient list system.

Keywords: Patient Lists; Efficient Welfare; Statistical Distributions

1. INTRODUCTION

In the Norwegian patient list system in general practice the patients can be assigned to a general practitioner that agrees to have the main responsibility for his or hers patients. As there are limited numbers of doctors of specific types, e.g. gender, it may happen that a significant number of patients are assigned to doctors of the wrong type, *i.e.* a type of doctor that they really do not want. This gives rise to several interesting research questions, among them: How can we characterize assignments that conform to reasonable criteria for total benefits to the patient-doctor community, when patients are individually competing for the scarce resource? Which changes in allocation can be expected when the availability of the scarce resource changes, e.g. by increased availability of female doctors? The latter is known to happen in many countries, and was precisely the question asked by the investigators on general practice and community medicine that posed the problem in the first place.

In [1] Ubøe and Lillestøl suggested a new statistical framework for this context, enable to answer questions of this kind, based on the concept of *benefit efficiency*. The next research challenge was then to see if the model allowed inferences, *i.e.*, to say something about the

preference structure based on an observed allocation. This turned out to involve some delicate theoretical problems, among them non-uniqueness, and the purpose of this paper is to present our solution to these problems. As an illustration of the theory we will consider a special case, using patient list data from the Norwegian patient list system in general practice. These data report the registered allocation of male and female patients to male and female doctors. While this is mainly a theoretical paper, the paper also offers some guidelines for practitioners that want to apply this kind of theory to real world data.

The theory of this paper follows from the idea of a *benefit efficient allocation*, which can be described as follows: Let A_1, A_2, \dots, A_T denote the sets of actions that agents of type 1, 2, ..., T can choose, let $U_i: A_i \rightarrow \mathbb{R}$ be the real number utilities of each choice, and let Q_1, Q_2, \dots, Q_T be a sequence of probability measures on A_1, A_2, \dots, A_T . Then $Q = Q_1 \times Q_2 \times \dots \times Q_T$ is called a *benefit efficient probability measure* if it satisfies the two conditions:

- Larger aggregated utility, *i.e.* sum of utilities of all agents, of an allocation implies larger probability of that allocation.
- As the number of agents of each type pass to infinity, the numbers of agents making each choice must satisfy a specified set of linear allocation constraints.

Quite surprisingly, there are extremely few probability measures of this type. In fact when utilities and constraints are given, these measures form a one parameter family. In the inverse problem we consider in this paper, the parameter can be set to 1 without loss of generality. Then the resulting allocation will be as given by Formula (1) in the theory section below, where we briefly recall the model construction in [1], and then show how we can obtain unique representations of preferences. To enhance readability, proofs and technical arguments are given in appendices.

The Norwegian patient list system in general practice

is described in some detail in [1], and we refer to this paper for a review of the system. Note that our modeling framework extends beyond the Norwegian patient list system and it can be understood without any particular knowledge of that system. Note also that our model is completely specified by Formula (1), and no further knowledge of the model will be needed to understand the issues we address in this paper.

In the application section we use our model to infer structure and strength of preferences from observed real world data. These data were collected from an official panel survey of Norwegian living conditions (Levekårsundersøkelsen 2003).

We believe that our basic approach to this problem is novel. It is fundamentally different from the theory of revealed preferences in consumer theory, see e.g. [2], and is not in any way related to the extensive economic literature on the design of matching system in health care, see e.g. [3]. Hence we will not enter into a discussion of other models in this area with a different scope.

2. METHODS

The model in [1] can be described briefly as follows: Assume that there are S groups of patients, T types of doctors, and let P_{ts} denote the number of patients in group s that has a doctor of type t , $s = 1, 2, \dots, S$, $t = 1, 2, \dots, T$.

● **Patients:** We assume that there is a total of E_s patients belonging to group s , $s = 1, 2, \dots, S$. A patient belonging to group s is assumed to have a utility U_{ts} of having a doctor of type t , $t = 1, 2, \dots, T$. It may sometimes happen that a patient prefer to wait for a vacancy of a suitable doctor rather than being assigned to a doctor of a type that the patient dislikes. We let $P_{t(s+S)}$ denote the number of patients of type s waiting for a doctor of type t (not being assigned to any doctor), and let $U_{t(s+S)}$ denote the utility of these patients.

● **Doctors:** Every doctor working within the system is assumed to have a certain list length, i.e., a maximum number of patients that he or she can serve. We assume that there are D_t doctors of type t , and that these doctors can serve a total of L_t patients, i.e., L_t is the sum of the list lengths of all doctors of type t . Some doctors may have vacancies, and we let $U_{t(2S+1)}$ denote the utility per vacancy incurred by a doctor of type t .

Thus we have defined P_{ts} and U_{ts} for $s = 1, 2, \dots, 2S + 1$, $t = 1, 2, \dots, T$, which can then be represented by $T \times (2S + 1)$ matrices P and U .

Utilities for vacancies and for being assigned to the wrong type of doctor may of course be negative, in which case we refer to these numbers as disutilities. Note that the word utility is used in a broad sense as a

quantification of strength of preferences. Utilities are hence not necessarily utilities in the von Neumann-Morgenstern sense.

Clearly the (E_1, \dots, E_S) patients can be allocated to the (D_1, \dots, D_T) doctors in many different ways. The basic hypothesis in [1], however, is to assume that the system is benefit efficient in the sense that states with large aggregate utility (sum of the utility of all patients and doctors) are more probable than states with smaller total utility. If the system is benefit efficient with a large number of patients in every group, it is possible to prove, see [1], that the allocation will settle at a statistical equilibrium given by the following explicit formula:

$$P_{ts} = \begin{cases} A_t B_s \exp(U_{ts}) & s = 1, \dots, S \\ D_t B_{s-S} \exp(U_{ts}) & s = S + 1, \dots, 2S \\ A_t \exp(U_{ts}) & s = 2S + 1 \end{cases} \quad (1)$$

$$\sum_{s=1}^S P_{ts} + P_{t(2S+1)} = L_t$$

$$\sum_{t=1}^T P_{ts} + P_{t(s+S)} = E_s$$

See Appendix 3 on how to compute the balancing factors $A_1, A_2, \dots, A_T, B_1, B_2, \dots, B_S$. Note that these allocations must not be confused with the allocation with *maximum total utility*. In fact, the allocation with maximum total utility can be obtained as special case if one multiplies the utilities in (1) with a constant and let that constant pass to infinity.

The basic problem we want to address in this paper can be formulated as follows: Assume that the system is benefit efficient and that we observe

- The total number of patients in each group, i.e. E_s , $s = 1, \dots, S$.
- The total number of doctors of each type, i.e. D_t , $t = 1, \dots, T$.
- The total list length of doctors of each type, i.e. L_t , $t = 1, \dots, T$.
- The final allocation of patients to doctors/waiting lists, i.e. P_{ts} , $s = 1, \dots, 2S + 1$, $t = 1, \dots, T$.

To what extent do these observations reveal the strength of the preferences

$$U_{ts}, s = 1, \dots, 2S + 1, t = 1, \dots, T?$$

It is easy to observe that there are always an infinite number of utility matrices leading to the same final allocation. To obtain uniqueness we hence have to impose some additional restrictions on specific utilities and/or the relationships between them. Such restrictions are typically based on prior knowledge of the context and on known empirics, and modeling issues of this kind are discussed in detail in Section 3. In Theorem 2.1 below, we single out one of the infinitely many representations, and refer to the representation in (2) as the canonical choice. This is useful for two main reasons: To

get insight to the degrees of freedom in modeling, and to provide a basis for numerical calculations.

2.1. Theorem 2.1

Assume that an observed patient list distribution \mathbf{P} can be replicated by a model that satisfies (1). Then we can find a unique utility matrix \mathbf{U} that replicates \mathbf{P} on the form (later referred to as (2)):

$$\begin{bmatrix} 0 & 0 & 0 & \dots & 0 & v_{11} & v_{12} & \dots & v_{1S} & 0 \\ 0 & u_{11} & u_{12} & \dots & u_{1(S-1)} & v_{21} & v_{22} & \dots & v_{2S} & w_1 \\ 0 & u_{21} & u_{22} & \dots & u_{2(S-1)} & \vdots & \vdots & & \vdots & w_2 \\ \vdots & \vdots & \vdots & \vdots & \vdots & \vdots & \vdots & & \vdots & \vdots \\ 0 & u_{(T-1)1} & u_{(T-1)2} & \dots & u_{(T-1)(S-1)} & v_{T1} & v_{T2} & \dots & v_{TS} & w_{T-1} \end{bmatrix} \quad (2)$$

PROOF: See Appendix 1.

The zeros in (2) can formally be interpreted as reference points and the corresponding groups as reference groups. Uniqueness is obtained when we specify how much more/less utility the other groups have in comparison to these reference groups. While the representation given by (2) has several favorable properties, results given on this form are quite hard to interpret. Hence it might be profitable to look for other representations offering more transparent interpretations. In general the position of the $S + T$ reference groups can be chosen in several different ways, and an important modeling issue is to specify natural reference groups for the given context.

We can also obtain alternative unique representations by assuming a utility structure with sufficient identities and/or symmetries. Nevertheless, it is convenient to use (2) as a canonical form, both for algorithmic programming and for resolving theoretical issues. One important issue is that of identification, *i.e.*, recovering the parameters of an assumed utility structure from its established canonical form. Equivalent structures are obtained by transformations of \mathbf{U} that leave \mathbf{P} invariant. These are:

- Add/subtract a fixed T -dimensional column vector \mathbf{a} to all columns of \mathbf{U} labeled $s = 1, \dots, S$ and $s = 2S + 1$ (*i.e.* except $s = S + 1, \dots, 2S$).
- Add/subtract a fixed $2S + 1$ -dimensional row vector of form $(\mathbf{b}, \mathbf{b}, 0)$, with \mathbf{b} S -dimensional, to all rows of \mathbf{U} .
- Add/subtract a constant c to column $s = 2S + 1$ of \mathbf{U} and at the same time subtract/add the same constant from all columns $s = S + 1, \dots, 2S$.

However, the easiest way to check identifiability may be to use the transform given by Formula (11) in Appendix 1 and check the uniqueness of the parameter recovery.

Note that the canonical form, as well as alternative models with the same number of (linear) restrictions, provides perfect fit to the available data. Hence any

inference does not lend itself to the usual statistical standard error computations.

3. RESULTS AND DISCUSSION

The Norwegian patient list system was introduced in year 2001 and is monitored by the authorities. Data on availability of doctors are made readily available to the public, and some aggregated data on list composition and vacancies are also available for research purposes. Reliable data on doctor preference are not readily available. However, some questions on the combination (gender of respondent, gender of assigned doctor, preferred gender of doctor) were included in the official panel survey of Norwegian living conditions (Levekårsundersøkelsen 2003). The questions asked relevant to our study were:

Q1: Do you want to relate to an assigned general practitioner, or do you want to use several general practitioners?

Q2: Do you mind whether your assigned general practitioner is male or female?

Q3: For those who answered “yes” on Q2: Do you want to have a male or a female assigned general practitioner, or do you want to use both a male and a female?

Unfortunately the response rate to the preference questions were low, and more so for males than females. Hence this part of the paper must be considered more as an illustration of the potential offered by the theory, and not so much as an empirical survey in its own right.

With the way of questioning above we were left with the problem of what to do with respondents who wanted both gender of doctors available. Since the system of a single assigned general practitioner was already firmly established with no opportunity of multiple assignments, we decided to split these relatively few respondents equally between the two preferences. The observed counts are shown in **Table 1**.

In this case $T = 2$, with types denoted M (male doctor) and F (female doctor), and $S = 4$ with groups denoted mm, mf, fm and ff, where the first letter is the gender of the patient and the second letter is the preferred gender of doctor.

A total of 3489 persons, 1736 men and 1753 women, were interviewed in the panel survey. As we can see from **Table 1**, the responses to the preference questions were very low, and more so for males than females. That partly explains the strong bias we observe in the data, *e.g.* 22% men, and we therefore scaled the data to adjust for this. Two issues are taken into account: First

Table 1. Observed counts in each group-original data.

Patient group	mm	mf	fm	ff
M-doctor	78	2	32	77
F-doctor	5	4	2	200

we have scaled the data so that there is an equal number of respondents of each sex, second we have scaled the data to get the marginal frequencies in accordance with the approximately known distribution of doctors at the time, namely 70% male doctors and 30% female doctors.

The results after these scalings are given in **Table 2** per 1000 respondents.

3.1. Missing Data and Partial Information

Officially there are no waiting lists, and data on this are hard to get. In Appendix 2, however, we prove that one can infer the correct preferences for the groups in **Table 2** even in the case where data on waiting lists and vacancies are missing. The crucial result, Theorem 5.4, states that these preferences are independent of the data for waiting lists and vacancies.

A survey made by the Norwegian Ministry of Health and Care Services (2004) reports a total of 2 026 doctors with vacancies, the average number of vacancies being 223. With the reported 4 563 751 patients served, this gives 99 vacancies per 1 000 patients. For illustrative purposes we round this in **Table 3** to 100 patients per 1000 served. We have no information on how this is distributed among the gender of doctors. If they are distributed evenly among the genders, the number will be as given in the parentheses in **Table 3**. Note that the number of patients who want a doctor of the same gender is higher for males than for females.

3.2. Inferring Canonical Utilities from Observed Data

The utility matrix corresponding to the types and groups in **Table 3** is

$$U = \begin{bmatrix} U_{11} & \cdots & U_{14} & U_{15} & \cdots & U_{18} & U_{19} \\ U_{21} & \cdots & U_{24} & U_{25} & \cdots & U_{28} & U_{29} \end{bmatrix} \quad (3)$$

where the row order is M, F and the column order is mm, mf, fm, ff, mm-w, mf-w, fm-w, ff-w, vacancy, where w indicates a waiting list state. According to Theorem 5.4 in Appendix 2, the missing data in **Table 3** can be chosen arbitrarily. Zero entries can be handled, but unless special care is taken such entries lead to serious numerical problems. For simplicity we have carried out all the calculations using the numbers reported in **Table 4**. We remark, however, that the numbers reported on waiting lists are fictitious but to some extent realistic.

To find replicating utilities, we use the construction described in Proposition 5.3 in Appendix 1. The result is shown in **Table 5**.

The numbers in parenthesis are based on the fictitious waiting list numbers. Hence the strength of preferences we can infer from the data in **Table 2** is given by **Table 6**.

If we take the canonical structure as our model, we may infer that that the patients with preference for the scarce gender (female doctors), have high utilities for correct matching compared with the reference groups, and that female patients wanting a male doctor while being assigned to a female doctor tend to have utilities slightly below the reference group zero.

Be aware, however, that this inference may be due to technical artifacts linked to the implicit assumptions caused by a special choice of reference groups. The canonical choice corresponds to an assumption where male patients wanting a male doctor are in effect indifferent to the gender of their doctor, and that may very well be an artificial assumption.

3.3. Modeling and Further Inference

We will now look into the modeling aspects of alternative representations. While the utilities reported in **Table 5** are the unique utilities on the form (2) that replicates the counts in **Table 4**, there are several other utility matrices that offer perfect replication. Also, observations of this type are subject to considerable amounts of randomness. Perfect replication is hence relatively unimportant, and models offering less than perfect fit may be superior if they carry more transparent information.

A main issue in this context is to quantify disutilities of incorrect patient/doctor matching. It is straightforward to verify that the solution of (1) is fixed if we add the same constant to all utilities within the same group, i.e., our model is sensitive to utility differences but does not depend on the general level of utility. Without loss of generality we can hence assume that all utilities for correct patient/doctor matching are equal to zero. These assumptions lead us to consider utility matrices on the form:

$$U = \begin{bmatrix} 0 & a_2 & 0 & a_4 & b_{11} & b_{12} & b_{13} & b_{14} & c_1 \\ a_1 & 0 & a_3 & 0 & b_{21} & b_{22} & b_{23} & b_{24} & c_2 \end{bmatrix} \quad (4)$$

Table 2. Adjusted data from **Table 1**.

Patient group	mm	mf	fm	ff
M-doctor	455	12	69	164
F-doctor	19	14	2	265
Total	474	26	71	429

Table 3. Scaled counts in each group per 1000 patients served.

Patient group	mm	mf	fm	ff	mm-w	mf-w	fm-w	ff-w	vac
M-doctor	455	12	69	164	-	-	-	-	(70)
F-doctor	19	14	2	265	-	-	-	-	(30)
Total	474	26	71	429	-	-	-	-	100

Table 4. Scaled counts with artificial waiting list data.

Patient group	mm	mf	fm	ff	mm-w	mf-w	fm-w	ff-w	vac
M-doctor	455	12	69	164	(8)	(4)	(9)	(1)	(70)
F-doctor	19	14	2	265	(2)	(6)	(4)	(6)	(30)
Total	474	26	71	429	(10)	(10)	(13)	(7)	100

Table 5. Canonical utilities according to (2) with Table 4 data.

P	mm	Mf	fm	ff	mm-w	mf-w	fm-w	ff-w	vac
M	0	0	0	0	(-7.7)	(-4.7)	(-5.7)	(-8.7)	0
F	0	3.3	-0.4	3.7	(-8.2)	(-3.7)	(-5.6)	(-6.1)	(2.3)

Table 6. Canonical utilities (2) inferred from Table 2.

Patient group	mm	mf	fm	ff	mm-w	mf-w	fm-w	ff-w	vac
M-doctor	0	0	0	0	-	-	-	-	0
F-doctor	0	3.33	-0.37	3.66	-	-	-	-	-

Here a_1, a_2, a_3, a_4 are the disutilities of incorrect patient/doctor matching. The question is now if it is possible to find utility matrices of the form (4) replicating the counts in **Table 4**. The transformation defined by Formula (11) in Appendix 1 transforms any utility matrix U to an equivalent matrix \tilde{U} on the form (2).

Equivalent means that the two matrices produce exactly the same counts when they are used in (1). Using (11) on the matrix in (4) we obtain Formula (5). We see that we do not have identifiability, unless we add restrictions. Nevertheless it is possible to infer some non-trivial relationships. If the utility matrix in (5) equals the matrix specified in **Table 5** or **6**, we get the equations

$$\begin{aligned} -a_2 - a_1 &= 3.33 \\ a_3 - a_1 &= -0.37 \\ -a_4 - a_1 &= 3.66 \end{aligned} \quad (6)$$

If we eliminate a_1 from the first and the third equation and rearrange the terms, we see that:

$$\begin{aligned} a_3 &= a_1 - 0.37 \\ a_4 &= a_2 - 0.33 \end{aligned} \quad (7)$$

By assumption, the utilities for correct patient/doctor matching are all equal to zero, and hence (by context) utilities for incorrect matching must all be negative (if they are not, agents must have been allocated to wrong groups). In (7) a_1, a_2 are the disutilities of incorrect matching for men, and a_3, a_4 are the disutilities of incorrect matching for women. From (7) we can draw

the conclusion that disutilities of incorrect matching are larger for women.

If we go one step further, we can introduce the additional assumptions: $a_1 = a_2 = a_m$ and $a_3 = a_4 = a_f$, *i.e.* that all men have the same disutility of incorrect matching, and all women have the same disutility of incorrect matching. In this case the system is overidentified, and perfect fit cannot be obtained. As mentioned above, perfect fit is relatively unimportant, however, and we can instead search for the best possible fit using utility matrices on the form

$$U = \begin{bmatrix} 0 & a_m & 0 & a_f & b_{11} & b_{12} & b_{13} & b_{14} & c_1 \\ a_m & 0 & a_f & 0 & b_{21} & b_{22} & b_{23} & b_{24} & c_2 \end{bmatrix} \quad (8)$$

The best replication, in the sense that we get an approximate solution to (6), is then

$$a_m = -1.66 \quad a_f = -2.02 \quad (9)$$

In this case all the relevant parameters are identified by our assumptions, and we maintain the conclusion from (7), *i.e.*, that disutilities of incorrect matching are larger for women. It is somewhat surprising that this rather crude approach produces the near perfect fit shown in **Table 7** (to be compared with observations in **Table 2**).

If we want to infer disutilities for vacancies or for being on waiting lists, we would have needed data for the allocation of these groups. Such data are missing. Nevertheless we will look into some general issues connected to these data.

If we compare the lower right corners in **Table 5** and **Eq.5**, we obtain the equation $c_2 - c_1 - a_1 = (2.33)$. This equation could in principle offer an alternative line to identification. If we assume that the disutilities for vacancies are equal for both gender of doctors, *i.e.*, that $c_1 = c_2$, we could infer the value $a_1 = (-2.33)$. This value could then have been inserted in (6) to identify the remaining disutilities in (6).

To proceed one step further, assume that all disutilities for being on waiting lists are equal, *i.e.*, that $b_{ij} = b$ for all $i = 1, 2$ and $j = 1, \dots, 4$, and that the disutilities for vacancies are equal for both gender of doctors, *i.e.*, that $c_1 = c_2 = c$. Then we could try to find the best possible fit using utility matrices on the form

$$U = \begin{bmatrix} 0 & a_m & 0 & a_f & b & b & b & b & c \\ a_m & 0 & a_f & 0 & b & b & b & b & c \end{bmatrix} \quad (10)$$

When modeling the utility structure with sufficient assumptions to get excess degrees of freedom, we essen-

$$\tilde{U} = \begin{bmatrix} 0 & 0 & 0 & 0 & b_{11} + c_1 & b_{12} + c_1 - a_2 & b_{13} + c_1 & b_{14} + c_1 - a_4 & 0 \\ 0 & -a_2 - a_1 & a_3 - a_1 & -a_4 - a_1 & b_{21} + c_1 & b_{22} + c_1 - a_2 & b_{23} + c_1 & b_{24} + c_1 - a_4 & c_2 - c_1 - a_1 \end{bmatrix} \quad (5)$$

tially have an estimation problem with an opportunity to judge the sampling error. It may then be helpful to bring the problem within the framework of conventional contingency table theory. In our application this may be done by lifting the 2×4 -block of waiting list patients up as a second layer on top of the 2×4 -block of assigned patients. On top of the block of vacancies we add a block of structural zeros. Thus we have a three-way table of size $2 \times 5 \times 2$ with the correct marginal features. By taking logarithms in the representation (1), we get a linear expression for the log-counts. Our modeling assumptions then give rise to a log-linear model with a specific parametric structure to be estimated, and for which readily available and applicable general theory exists. In the model (10), we have 4 parameters a_m , a_f , b and c , in addition to the 8 scaling constants A_i , D_i , $i = 1, 2$ and B_j , $j = 1, 2, 3, 4$. These parameters may then be estimated by maximum-likelihood principle, for which asymptotic theory is available and provides approximate standard errors of estimates, see, e.g. Bishop *et al* (1975).

Remark. To estimate the parameters in (10) we would have needed to make use of the artificial data in **Table 4**. These data were not available and were included for illustration only. To some extent the method suggested for (10) is also relevant for the analysis of (8). As shown in **Table 7**, a simplistic approach already produces near perfect fit, and alternative/more refined methods would not change this. For these reasons we will not pursue this further.

4. CONCLUSIONS

In [1] Ubøe and Lillestøl proposed a new type of statistical model to study the allocation of groups of patients to different types of doctors according to given preferences. This paper clarifies the inverse problem of how to identify preferences based a given allocation.

As an illustration of the theory we have applied the model to patient list data from the Norwegian patient list system in general practice. However, this type of model can be used to infer preferences from much more refined systems than the one we have studied here. We only

made use of two types of doctors and four groups of patients, while the model allows arbitrary many types of doctors and arbitrary many groups of patients.

The revealed preferences from the Norwegian patient list data turned out to be very reasonable, and mostly in accordance with prior beliefs. The main empirical finding that disutilities for incorrect matching are larger for women than for men appears to be a relatively robust conclusion that can be inferred from different model formulations.

Despite the weakness of our data, they may give some backing for the health authorities, e.g., when asking questions like: What changes are likely to happen when the fraction of female doctors is on the rise? This may be answered by using the model in the forward manner, as described in [1], and in more detail in [5]. Revealed disutilities are then used as input, representing the current preference status. It would clearly be of interest to have periodic updates on patient allocations and preferences to investigate the stability of disutilities.

5. ACKNOWLEDGEMENTS

The authors wish to thank Yngve Rønsen MD who proposed the patient list problem and Gry Henriksen at the Norwegian Social Science Services (NSD) for making the patient list data available to us.

REFERENCES

- [1] Ubøe, J. and Lillestøl, J. (2007) Benefit efficient statistical distributions on patient lists. *Journal of Health Economics*, **26**(4), 800-820.
- [2] Varian, H.R. (2006) Revealed preferences. in Szenberg, M., ed., *Samuelsonian Economics and the 21st Century*, Oxford University Press, 99-115.
- [3] Roth, A.E. and Peranson, E. (1999) The redesign of the matching market for American physicians: Some engineering aspects of economic design. *The American Economic Review*, **89**(4), 748-780.
- [4] Bishop, Y.M.M. Fienberg, S.E. and Holland, P.W. (1975) Discrete multivariate analysis: Theory and practice. The MIT Press, Cambridge Mass.
- [5] Lillestøl, J., Ubøe, J., Rønsen, Y. and Hjortdahl, P. (2007) Patient allocations according to circumstances and preferences. Discussion paper, Norwegian School of Economics and Business Administration, Bergen.
- [6] Bregman, L.M. (1967) The relaxation method of finding the common point of convex sets and its application to the solution of problems in convex programming. *USSR Computational Mathematics and Mathematical Physics*, **7**, 200-217.

Table 7. Counts using $a_m = -1.66$, $a_f = -2.02$.

Patient group	mm	mf	fm	ff
M-doctor	455	12	69	163
F-doctor	19	14	2	266
Total	474	26	71	429

APPENDICES

Appendix 1: Proof of Theorem 2.1

Consider the following matrix transformation

$$\tilde{U}_{ts} = \begin{cases} U_{ts} - U_{t1} - U_{1s} + U_{11} & s = 1, \dots, S \\ U_{ts} - U_{1(s-S)} + U_{1(2S+1)} & s = S+1, \dots, 2S \\ U_{ts} - U_{t1} - U_{1(2S+1)} + U_{11} & s = 2S+1 \end{cases} \quad (11)$$

LEMMA 5.1

Let $U = \{U_{ts}\}$ be given, let $\tilde{U} = \{\tilde{U}_{ts}\}$ be defined by (11) and let P and \tilde{P} denote the corresponding distributions of patients in (1) when we use U and \tilde{U} , respectively. Then $P = \tilde{P}$.

PROOF

Let $A_1, \dots, A_T, B_1, \dots, B_S$ denote the balancing factors solving (1) when we use U , and define

$$\begin{aligned} \tilde{A}_t &= A_t \exp(U_{t1} + U_{1(2S+1)} - U_{11}) \quad t = 1, \dots, T \\ \tilde{B}_s &= B_s \exp(U_{1s} - U_{1(2S+1)}) \quad s = 1, \dots, S \end{aligned} \quad (12)$$

If $s = 1, \dots, S$ we get

$$\tilde{A}_t \tilde{B}_s \exp(\tilde{U}_{ts}) = A_t B_s \exp(U_{ts}) \quad (13)$$

If $s = S+1, \dots, 2S$ we get

$$\begin{aligned} D_t \tilde{B}_{s-S} \exp(\tilde{U}_{ts}) &= D_t B_{s-S} \exp(U_{1(s-S)} - U_{1(2S+1)}) \\ &\times \exp(U_{ts} - U_{1(s-S)} + U_{1(2S+1)}) \quad (14) \\ &= D_t B_{s-S} \exp(U_{ts}) \end{aligned}$$

If $s = 2S+1$ we get

$$\begin{aligned} \tilde{A}_t \exp(\tilde{U}_{ts}) &= A_t \exp(U_{t1} + U_{1(2S+1)} - U_{11}) \\ &\times \exp(U_{ts} - U_{t1} - U_{1(2S+1)} + U_{11}) \quad (15) \\ &= A_t \exp(U_{ts}) \end{aligned}$$

which proves the lemma.

PROPOSITION 5.2

Let $U^{(1)}$ and $U^{(2)}$ denote two utility matrices, and assume that $P^{(1)} = P^{(2)}$ in (1). Using the transformation in (11) we have $\tilde{U}^{(1)} = \tilde{U}^{(2)}$.

PROOF

We have to prove that the balancing factors must be equal, and then it follows from (1) that all the utilities must be equal as well. It follows from Lemma 2.1 that $\tilde{P}^{(1)} = \tilde{P}^{(2)}$, and observe from (11) that $\tilde{U}_{1(2S+1)}^{(1)} = \tilde{U}_{1(2S+1)}^{(2)} = 0$ by definition. Since

$$\tilde{A}_1^{(1)} \exp(\tilde{U}_{1(2S+1)}^{(1)}) = \tilde{A}_1^{(2)} \exp(\tilde{U}_{1(2S+1)}^{(2)}) \quad (16)$$

it follows that $\tilde{A}_1^{(1)} = \tilde{A}_1^{(2)}$. Now put $t = 1$ and $s = 1, \dots, S$, and observe from (11) that $\tilde{U}_{1s}^{(1)} = \tilde{U}_{1s}^{(2)} = 0$ by definition. Hence from (1) we get

$$\tilde{A}_1^{(1)} \tilde{B}_s^{(1)} \exp(\tilde{U}_{1s}^{(1)}) = \tilde{A}_1^{(2)} \tilde{B}_s^{(2)} \exp(\tilde{U}_{1s}^{(2)}) \quad (17)$$

Since $\tilde{A}_1^{(1)} = \tilde{A}_1^{(2)}$ it follows that $\tilde{B}_s^{(1)} = \tilde{B}_s^{(2)}$ for all $s = 1, \dots, S$. We then put $s = 1$ and $t = 1, \dots, T$, and observe from (11) that $\tilde{U}_{t1}^{(1)} = \tilde{U}_{t1}^{(2)} = 0$ by definition. From (1) again we get

$$\tilde{A}_t^{(1)} \tilde{B}_1^{(1)} \exp(\tilde{U}_{t1}^{(1)}) = \tilde{A}_t^{(2)} \tilde{B}_1^{(2)} \exp(\tilde{U}_{t1}^{(2)}) \quad (18)$$

Since $\tilde{B}_1^{(1)} = \tilde{B}_1^{(2)}$ it follows that $\tilde{A}_t^{(1)} = \tilde{A}_t^{(2)}$ for all $t = 1, \dots, T$. We have hence proved the proposition.

Proof of Theorem 2.1

By assumption we can find a matrix U that replicates P . According to Lemma 5.1 \tilde{U} also replicates P . By construction \tilde{U} is on the special format given by (2). Hence there exists a matrix on the form (2) that replicates P . Conversely if a matrix is of the form given by (2), it does not change when we apply the transformation given by (11). Uniqueness then follows from Proposition 5.2.

PROPOSITION 5.3

Let $\{P_{ts}^{obs}\}$ be the observed numbers on the patient lists. The replicating matrix in Theorem 2.1 can then be constructed as follows. Put:

$$U_{ts} = \begin{cases} \ln(P_{ts}^{obs}) & \text{if } s = 1, \dots, S \\ \ln(P_{ts}^{obs} / D_t) & \text{if } s = S+1, \dots, 2S \\ \ln(P_{ts}^{obs}) & \text{if } s = 2S+1 \end{cases} \quad (19)$$

If we put $A_t = 1$, $B_s = 1$ in (1), it is easy to verify that the model in (1) replicates the observed pattern. The unique replicating matrix in Theorem 2.1 can then be found applying the transformation in (11) to the utilities in (19).

Appendix 2: Inference under Partial Information

Assume that we know the number of patients on the patient lists and the number of vacancies, but do not know how many patients that are waiting for a vacancy. Is it then possible to infer the strength of preferences of the patients on the patient lists? The answer is yes, and this can be demonstrated as follows:

Assume that $P_{ts}^{(0)}$ $s = 1, \dots, S$, $t = 1, \dots, T$ is given, and let $P_{ts}^{(1)}$ and $P_{ts}^{(2)}$ be arbitrary numbers for $s = S+1, \dots, 2S+1$, $t = 1, \dots, T$. Define the following aggregated quantities

$$L_t^{(0)} = \sum_{s=1}^S P_{ts}^{(0)}, E_t^{(0)} = \sum_{t=1}^T P_{ts}^{(0)},$$

$$L_t^{(i)} = \sum_{s=S+1}^{2S+1} P_{ts}^{(i)}, E_s^{(i)} = \sum_{t=1}^T P_{ts}^{(i)} \quad i=1, 2$$

THEOREM 5.4

For $i = 1, 2$ put $L_t = L_t^{(0)} + L_t^{(i)}, E_s = E_s^{(0)} + E_s^{(i)}$ and find a unique matrix $U^{(i)}$ of the form (2) such that the system given by (1) replicates the numbers

$$P_{ts} = \begin{cases} P_{ts}^{(0)} & \text{if } s=1, \dots, S, t=1, \dots, T \\ P_{ts}^{(i)} & \text{if } s=S+1, \dots, 2S+1 \end{cases} \quad (20)$$

If $K = P_{1(2S+1)}^{(2)} / P_{1(2S+1)}^{(1)}$ then the two utility matrices $U^{(1)}$ and $U^{(2)}$ are connected through the formula (here referred to as **Eq.21**):

$$U_{ts}^{(2)} = \begin{cases} U_{ts}^{(1)} & s=1, \dots, S, t=1, \dots, T \\ U_{ts}^{(1)} + \ln\left(\frac{P_{ts}^{(2)}}{P_{ts}^{(1)}}\right) + \ln(K) & s=S+1, \dots, 2S, t=1, \dots, T \\ U_{ts}^{(1)} + \ln\left(\frac{P_{ts}^{(2)}}{P_{ts}^{(1)}}\right) - \ln(K) & s=2S+1, t=1, \dots, T \end{cases}$$

PROOF

Define a new utility matrix \tilde{U} by the right hand side of (21) and let $A_t^{(1)}, t=1, \dots, T$ and $B_s^{(1)} s=1, \dots, S$ denote the balancing factors solving (1) using the replicating utilities $U^{(1)}$. Now put $A_t^{(2)} = A_t^{(1)} \cdot K$ and $B_s^{(2)} = B_s^{(1)} / K$.

If $s=1, \dots, S, t=1, \dots, T$ we get by (1)

$$A_t^{(2)} B_s^{(2)} \exp(\tilde{U}_{ts}) = A_t^{(1)} \cdot K \cdot B_s^{(1)} / K \exp(U_{ts}^{(1)})$$

$$= A_t^{(1)} B_s^{(1)} \exp(U_{ts}^{(1)}) = P_{ts}^{(0)}$$

If $s=S+1, \dots, 2S, t=1, \dots, T$ we get by (1)

$$D_t B_{s-S}^{(2)} \exp(\tilde{U}_{ts})$$

$$= D_t B_{s-S}^{(1)} / K \exp(U_{ts}^{(1)} + \ln\left(\frac{P_{ts}^{(2)}}{P_{ts}^{(1)}}\right) + \ln(K))$$

$$= P_{ts}^{(1)} \cdot \frac{P_{ts}^{(2)}}{P_{ts}^{(1)}} = P_{ts}^{(2)} \ln(K)$$

If $s=2S+1, t=1, \dots, T$ we get by (1)

$$A_t^{(2)} \exp(\tilde{U}_{ts}) = A_t^{(1)} \cdot K \exp(U_{ts}^{(1)} + \ln\left(\frac{P_{ts}^{(2)}}{P_{ts}^{(1)}}\right) - \ln(K))$$

$$= P_{ts}^{(1)} \cdot \frac{P_{ts}^{(2)}}{P_{ts}^{(1)}} = P_{ts}^{(2)}$$

The marginal constraints are automatically satisfied when the model replicates each entry in the matrix. Note that

$$\tilde{U}_{1(2S+1)} = U_{1s}^{(1)} + \ln\left(\frac{P_{1(2S+1)}^{(2)}}{P_{1(2S+1)}^{(1)}}\right) - \ln(K) = U_{1s}^{(1)} = 0$$

and that if $s=1, \dots, S$, then $\tilde{U}_{ts} = U_{ts}$. This proves that \tilde{U} is of the form (2). Hence if we put $U^{(2)} = \tilde{U}$ this matrix is the unique matrix on the form (2) that replicates the system in (20) when $i=2$.

As we can see from Theorem 6.1, the utilities U_{ts} $s=1, \dots, S, t=1, \dots, T$ do not depend on the values of P_{ts} for $s=S+1, \dots, 2S+1, t=1, \dots, T$. Hence we have the following corollary:

COROLLARY

Assume that $P_{ts} s=1, \dots, S, t=1, \dots, T$ are known, while data on P_{ts} for $s=S+1, \dots, 2S+1, t=1, \dots, T$ are missing. If we choose $P_{ts} > 0$ for $s=S+1, \dots, 2S+1, t=1, \dots, T$ arbitrarily, we can still infer the correct values on U_{ts} for $s=1, \dots, S, t=1, \dots, T$.

Remark. From the bottom line in Formula (21) we see that we can also obtain strength of preferences for vacancies in cases where information on the number of patients waiting for vacancies is missing. Clearly, however, it is impossible to infer strength of preferences for groups of patients waiting for vacancies unless we have data for these groups.

Appendix 3: Numerical Methods

How to find a numerical solution to (1) when utilities U and marginal constraints L and E are given? We need to find numerical values for the $S+T$ balancing factors $A_1, \dots, A_T, B_1, \dots, B_S$. This is done as follows:

Initially we put all the balancing factors equal to 1. Then for $t=1, \dots, T$ we update A_t using

$$A_t = \frac{L_t}{\sum_{s=1}^S B_s \exp(U_{ts}) + P_{t(2S+1)}} \quad (22)$$

Once these are updated, then for $s=1, \dots, S$ we update B_s using

$$B_s = \frac{E_s}{\sum_{t=1}^T (A_t \exp(U_{ts}) + D_t \exp(U_{t(s+S)}))} \quad (23)$$

We then repeat the updates in (22) and (23) until the system settles. The algorithm is a variant of the Bregman balancing algorithm, see Bregman (1967). Like the standard Bregman algorithm this algorithm is surprisingly efficient, and solves large systems in a very short time.

Study of the bones tissue reparation using nanostructured titanium implants with hydroxylapatite coatings by scanning electron microscopy

Tatiana V. Pavlova¹, Sergei Y. Zaitsev², Lubov A. Pavlova^{1,3}, Dmitriy A. Kolesnikov³

¹Department of Pathology, Belgorod State University, Belgorod, Russia;

²Department of Organic and Biological Chemistry, Moscow State Academy of Veterinary Medicine and Biotechnology named after K. I. Skryabin, Moscow, Russia;

³Center of Nanostructural Materials and Nanotechnologies, Belgorod State University, Belgorod, Russia.

Email: szaitsev@mail.ru

Received 28 April 2010; revised 21 May 2010; accepted 14 June 2010.

ABSTRACT

A method of medical implants (biocomposites) preparation based on nanostructured titanium with nanocrystalline bioactive hydroxylapatite coatings is developed. The operative treatment using these implants improves the regeneration of bone tissue for rats, as compared to the “false-operated” animals. The morphological data at 7, 14, 21, 45 days are obtained by means of scanning electron microscopy and discussed.

Keywords: Scanning Electron Microscopy; Implant; Regeneration; Nanostructures; Bone Tissue

1. INTRODUCTION

The application of nanostructured material such as implants with bioactive coatings in medicine is a rapidly growing research field that has considerable economical and social effect. The nanostructured material can be obtained by numerous techniques based on nanoparticles possessing unique properties. It is well-known that in such a nanoparticle compared to larger objects the percentage of surface atoms or molecules increases in comparison with total atoms (molecules). Surface, electric, magnetic, mechanic and some other properties of the material composed of such nanoparticles are no longer constant and begin depending on the size and form of the particles [1,2]. Sometimes the nanostructured materials show absolutely surprising qualities, which can find potential application in the various fields of science and technology, in particular, in medicine [3,4].

A special method of medical implants (biocomposites) preparation based on nanostructured titanium and its alloys with nanocrystalline bioactive calcium-phosphate

coatings is developed in the Belgorod State University [5]. The presence of such hydroxylapatite (HA) coating gives these implants valuable bioactive properties, that improves the implant ability to integrate bone cells and form bony tissue at the coatings surface as compared to the pure titanium implants [6,7].

The main aim of our research was the scanning electron microscopy study of biocompatibility and regenerative processes of bony tissue at operational interventions into bony tissue using materials with nanocrystalline hydroxylapatite coatings.

2. MATERIALS AND METHODS

Model implants of nanostructured technically pure titanium of the trademark BT1-0 were produced in the rod form. Using the “micro-arch” oxidizing method the implant was covered with a layer of 2-5 μm thick titanium dioxide with controlled porosity. At the last stage the nanocrystalline high-purity hydroxylapatite (HA) [1] with layer thickness of about 5 μm was applied to the surface [8].

Twenty laboratory animals (20 “V-star”-line rats) were used in the experiments. The animals were divided into the following groups: 15 rats were subjected to resection craniotomy in the right temporal region with the immobilization of a nanostructured titanium implant coated with nanocrystalline HA; 5 animals made the control group, operated without implantation (assigned as “false-operated”).

The implantation procedure was fulfilled by given ether narcosis to rats. The 0.8 cm length operative incision from soft tissues up to the bone was made after the treatment of the operative field in aseptic conditions. The wound edges were separated and in the region of the transitory fold a widowing was performed with an oph-

thalmic scalpel. The opening field was enlarged up to the implant size, i.e. to 0.3 cm × 0.5 cm. The implants were imbedded into the operation field without biostructures' entrapment. The wound was sewed tightly. The operation "toilette" was carried out by means of brilliant green solution. After the anaesthesia recovery all rats were active and performed the "toilette" of corresponding external fields of their bodies. Active movement retained in full. There were no pyramidal insufficiency signs registered.

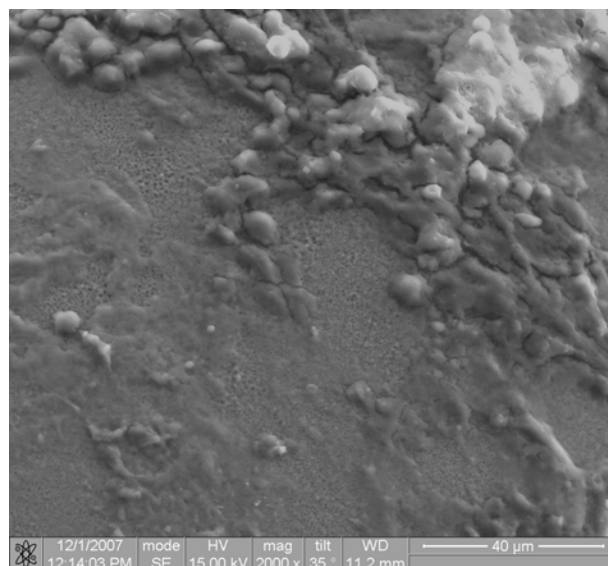
After the operation the rats were divided into 4 groups for the regeneration studies in 7 days (the 1st group), in 14 days (2 group), in 21 days (3 group), 45 days (4 group). At these time points the rats were by decapitated (beaten death at the humanitarian conditions, etherization, etc.). For the determination of possible implant toxicity the parenchymal organs (liver, kidneys, lungs, heart) were taken out for the (macro) pathology examination and (micro)histology study. The histological materials were colored with hematoxylin and eosin and subjected to a research under the optical microscope "TOPIS-T" CETI. The bone lamella was taken out together with the implant, examined and photographed through the scanning electron microscope FEI Quana 200 3D as described in the papers [9,10].

3. RESEARCH RESULTS

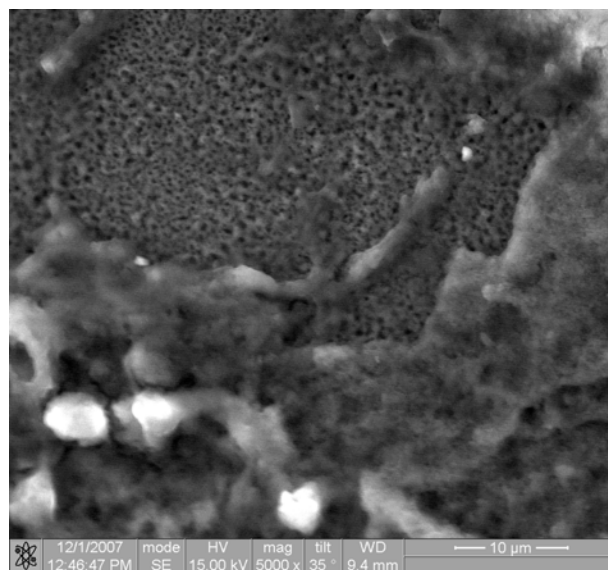
At the function study of all experimental animals it is evident that cognitive, as well as main neurophysic functions are not altered. The animals are active, vigorous in the open plain, all movements are retained in full. There are no changes registered in the cardiovascular, respiratory and digestive systems.

It is found by the microscopic examination of the animal samples that the operation incisions are healed by means of surface tension. By the 21st day the traumatic defect is not pronounce or visible at the general surface. It should be noted that in the animals, having been operated using experimental implants, the vascular pattern is more distinct than that of the "false-operated" ones. Besides, for the experimental animals the dura mater vessels' frank repletion in the region adjacent to the bone lamella is defined on the 7th and 14th days.

At the submicroscopic scanning the following processes were found. First, at 7th day we observed the filling of the defect between the retained bony tissue and the immobilized implant with "argyrophil" and collagen fibers that were already located on the lamella (implant) itself. Still we can observe a lot of empty space at the implant surface with only few fibers filling empty spaces between the regions with calcium-phosphate coating (Figure 1). Second, studying the animals at 14th day, the covering of the main parts of the lamella (implant) from



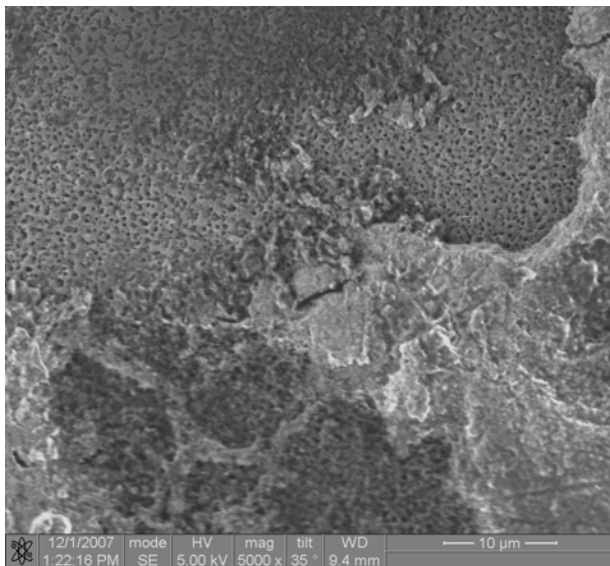
(a)



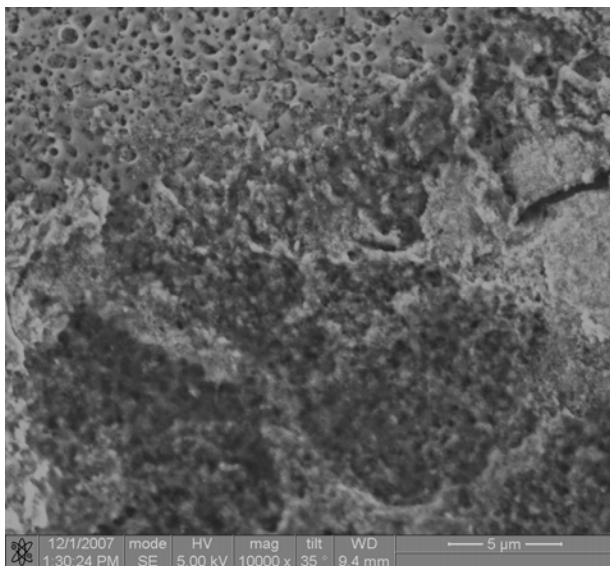
(b)

Figure 1. SEM images of the titanium implant fragment with nanostructured hydroxylapatite coating after immobilization into the rat's skull bony tissue (7 days after operation): image (a) PM (power magnification) × 2000; image (b) Fragment of the image 1(a) by PM × 5000.

the outside with a thin monolayer of collagen and elastic fibers occurs. The fibroblasts with deviating collagen fibers are clearly seen (Figure 2). Only relatively small regions with the calcium-phosphate coating implant still baring or partly covered with "argyrophil" fibers, as analogous to the samples at the 7th day regeneration stage (Figure 1). Third, studying the reparation processes in 21st day, a panniculus, which is a rough fibrous tissue represented by thick layers of the collagen



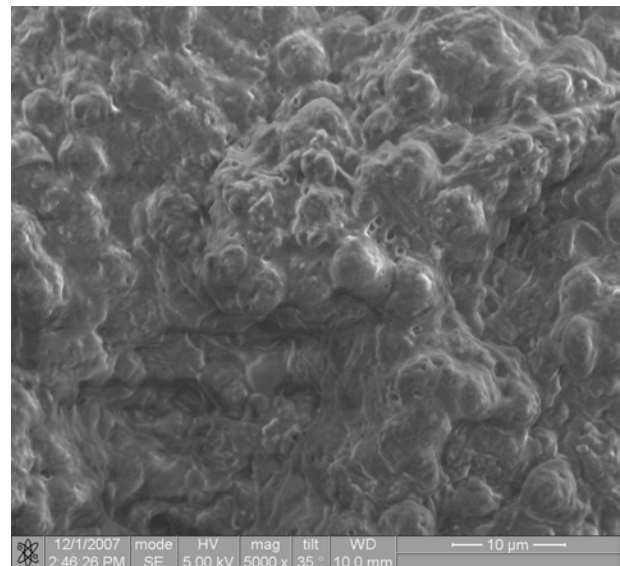
(a)



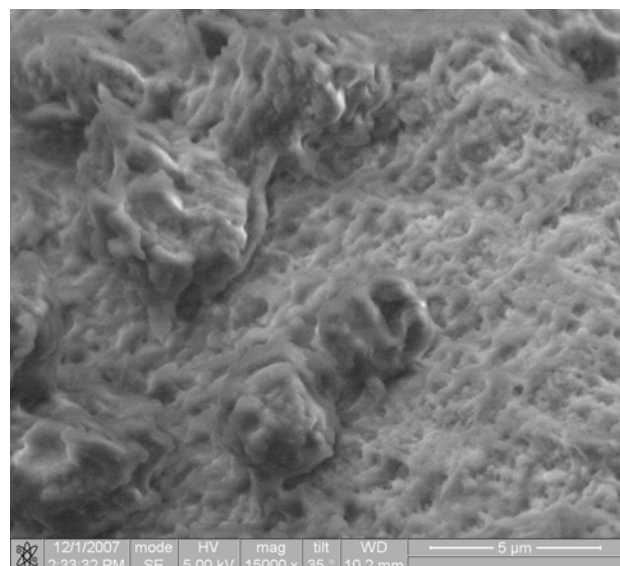
(b)

Figure 2. SEM images of the titanium implant fragment with nanostructured hydroxylapatite coating after immobilization into the rat's skull bony tissue (14 days after operation): image (a) PM $\times 5000$; image (b) Fragment of the image 2(a) by PM $\times 10000$.

fibers located disorderly with the intercellular matrix was observed (**Figure 3**). A lamellar bony tissue, wherein collagen fibers are located in parallel rows (bone lamella), but the orientation of the fibers in the neighboring layers is different. The lamellar bony tissue forms “compact” and “spongy” bone layers. The “compact” layer defines the mechanical strength of the bone and consists of lamellar bone tissue, where blood vessels and nerves begin being formed (as osteons). The



(a)



(b)

Figure 3. SEM images of the titanium implant fragment with nanostructured hydroxylapatite coating after immobilization into the rat's skull bony tissue (21 days after operation): image (a) PM $\times 5000$. image (b) Fragment of the image 3(a) by PM $\times 15000$.

“spongy” layer, which is inside the bone, was only at the beginning of formation. The lamellar bone tissue fibroblasts with greater amount of collagen and elastic fibers gradually exchanged by the cells of the osseous system process layer: osteoblasts, osteocytes and osteoclasts.

There are numerous processes helping to make contacts with neighboring cells, in particular, in the osteoblasts. Secreted by practically all the cell's surface,

procollagen contacts actively with the nanocoating. There are two types of osteoblasts (active and inactive) in the most cases in our study. The active forms, which are responsible for the synthesis of collagen and other proteins being part of the organic bone matrix, deposit and exchange of calcium and other ions, occur for the most part. Very few osteocytes occurred at this stage. The tissue was not yet fully structured and almost no "lacunes" visible. The osteocytes represented round shape cells with long fine processes. The osteocytes in the basal region contained nuclei, many mitochondria, granular endoplasmic reticulum elements, Golgi complex. Moreover, a lamellar bone tissue formed by bone lamellas was defined in the preparations, it forming "compact" and "spongy" substance in the bone.

It should be remarked that during the first and third days the formation and growth of a haematoma in the implant place was observed. Then, by the 7th-14th days together with mildly expressed inflammation we observed the migration and proliferation of mesenchymal cells, the formation of fibrovascular tissue round the implant. After that the vascular invasion into the implant surface layer, osteoplastic resorption of the last and formation of a neoformed bone on the implant's surface took place. It is important to underline that by examination of the rats in 45th day, the most part of the lamella was substituted by the tissue analogous to bone one located near the region of trepanation.

A study of the parenchymal organs (liver, kidneys, lungs, heart) in a week after the implant introduction mainly normal states with only mildly expressed repletion were defined that was indicative at the same stage for the "false-operated" animal group as well. There were no changes registered at 14th and 21st days.

4. CONCLUSIONS

Thus, the operative treatment using titanium implants with calcium-phosphate nanocrystalline coatings improves the regeneration of bone tissue, as compared to the "false-operated" animals. The intoxication phenomena and nanopathology development being not observed. The use of such innovation implant technology makes possible fast and noninvasive repair of the animal bony

structures.

5. ACKNOWLEDGEMENTS

This work was supported by the Russian Foundation for Basic Research and the Russian Ministry of Science (contract N. 02.740. 11.5013).

REFERENCES

- [1] Drago, C.J. and Peterson, T. (2007) Treatment of an edentulous patients with CAD/CAM technology: A clinical report. *Journal of Prosthodontics*, **16**(3), 200-208.
- [2] Griffin, T.J. and Cheung, W.S. (2004) The use short, wide implants in posterior areas with reduced bone height: A retrospective investigation. *Journal of Prosthetic Dentistry*, **92**(2), 139-144.
- [3] Heydenrijk, K., Raghoobar, G.M., Maijer, H.J. and Steganga, B. (2003) Clinical and radiologic evaluation of 2-stage IMZ implants placed in a single-stage procedure: 2-year results of a prospective comparative study. *International Journal of Oral & Maxillofacial Implants*, **18**(3), 424-432.
- [4] Heydecke, G., McFarland, D.H., Feine, J.S. and Lund, J.P. (2004) Speech with maxillary implant prostheses: Ratings of articulation. *Journal of Dental Research*, **83**(3), 236-240.
- [5] Volkovnyak, N.N., Ivanov, M.B., Kolobov, Y.R., Buzov, A.A. and Chuyev, V.P. (2007) Method of nanosized bone-salt obtaining. Patent Application RF No. 2007130861.
- [6] Martini, D., Fini, M., Franchi, M., *et al.* (2003) Detachment of titanium and fluorohydroxyapatite particles in unloaded endosseous implants. *Biomaterials*, **24**(7), 1309-1316.
- [7] Keller, J.C. (1998) Tissue compatibility to different surface of dental implants: *In vitro* studies. *Implant Dentistry*, **7**(4), 331-337.
- [8] Leontyev, V.K. (1996) Biologically active synthetic calcium-phosphate-containing materials for oral medicine. *Stomatology*, **5**, 4-6.
- [9] Pavlova, T.V., Pavlova, L.A. and Pavlov, I.A. (2007) Response of living cells tissues to titanium-aluminium-vanadium alloys implantation. *System Analysis and Management in Biomedical Systems*, **6**(2), 364-365.
- [10] Pavlova, T.V., Kriveckii, V.V. and Pavlova L.A. (2009) Innovation methods of bones tissue reparation in case of titanium implants with nanohydroxylapatite coatings. *System Analysis and Management in Biomedical Systems*, **8**(2), pp. 314-317.

Shoulder joint flexibility in top athletes

Hassan Daneshmandi*, Farhad Rahmaninia, Hossein Shahrokhi, Pegah Rahmani, Saeid Esmaeili

Guilan University, Rasht, Iran.

Email: Danesh@guilan.ac.ir, Daneshmandi_ph@yahoo.com

Received 17 April 2010; revised 17 May 2010; accepted 22 May 2010.

ABSTRACT

Joint range of motion (ROM) is very important in daily activities, sport and in clinical diagnosis. Many factors have been reported to influence joint ROM. Musculoskeletal adaptation and some special side effects due to his or her physical demands and movement patterns in professional athletes are very important subjects in sport sciences. The present study is a comparison of shoulder joint ROM in elite athlete and non-athlete groups and its relationship to their age, post and years of their tournament play. The subjects in this study included 106 men with mean age (23.65 ± 3.45) and mean years of tournament play (5.60 ± 2.23). The groups of subjects included 26 handball players, 25 volleyball players, 25 soccer players and 30 non-athletes. Data were collected through questionnaires and inspection, and subjects' ROM was measured by "Leighton flexometer" ($r = 0.90 - 0.99$) in external rotation and abduction of shoulder joint in dominant and non-dominant hands. Data were analyzed by correlation coefficient, t - test, ANOVA and post hoc Schaffe test. The results showed that an increase in age and years of tournament play reduced the shoulder ROM of subjects ($p \leq 0.05$). There were significant differences in shoulder ROM among athletic groups. Additionally, there are significant differences between dominant and non-dominant hands ($p \leq 0.05$). It can be concluded that more specific stretching exercises and warm-up for shoulder in all athletes and especially in older and experienced players should be performed by coaches. The results also emphasized routine screening, corrective exercise programs and a design of preventing strategies by athletic trainers and coaches.

Keywords: Range of Motion; Shoulder Joint; Handball; Volleyball; Soccer; Age; Years of Tournament Play; Playing Post

1. INTRODUCTION

Joint range of motion (ROM) data is a very important

reference in job and workplace design as well as in clinical diagnosis. Many factors have been reported to influence joint ROM. With an increase in age, the degeneration in these tissues becomes progressively more apparent, and results in a reduction in joint ROM. Other factors such as pain, dominant side, and the time of day may also have effects on joint ROM [1]. The physical demands of sport performance on the athletes' body cause certain musculoskeletal adaptation. Professional athletes spend most of their sporting life in training and competition [2]. Load placed on the musculoskeletal system may be generally classified as tensile or compressive. Repeated demands on a musculotendinous unit may cause it to shorten, decreasing normal joint range of motion [3]. Musculoskeletal adaptation and some special side effects due to his or her physical demands and movement patterns in professional athletes are very important subjects in sport sciences. The musculoskeletal adaptation at this point is called maladaptation, reducing joint range of motion, changing biomechanical patterns, decreasing the efficiency of force production, and increasing the chance of injuries to the musculoskeletal system [4]. Faulty posture could be also the result of that adaptation [5]. However, faulty posture does not necessarily indicate a disorder but it could cause a loss of optimum body mechanics [6].

There is a general agreement that the appropriate amount of exercise is important for the healthy growth and optimal development of the body [7]. By contrast, too much or too little exercise and inappropriate training may have some adverse effects [8]. Overtraining is an imbalance between training and recovery. This term is not new. The symptoms of prolonged fatigue, loss of motivation, burn out and staleness have been described in athletes for many decades. They are the maladaptive responses to the stimulus of training and an extended period of overload. Maladaptation flexibility due to frequent and old injuries has been recognized for some time [9]. Each sport has specific patterns of movement which has an effect on related joint range of motion (ROM) because skeletal tissue possesses an intrinsic ability to

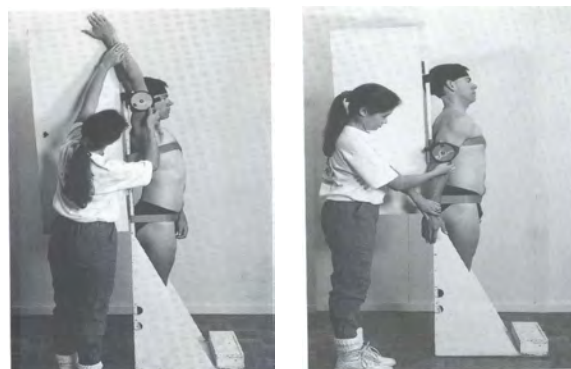
adapt to these physical activities. Adaptations take place in response to exercise training and those specific patterns of movements. In general, exercise programs usually include strength, power, endurance and flexibility training. In shoulder researches, measurements of range of motion (ROM) have been used as outcome measures in the vast majority of reported trials [10]. Therefore, the present study was proposed to compare the range of motion of shoulder joint (ROM) in elite athlete and non-athlete groups and its relationship to their age, post and years of tournament play.

2. METHODOLOGY

The subjects of this study were members of league teams with more than 2 years of play in league competitions. These subjects included 106 men with mean age (23.65 ± 3.45) and mean of participation in tournament play (5.60 ± 2.23). The groups of subjects included 26 handball players (mean age 23.57 ± 2.67 , mean playing history 6.38 ± 2.07), 25 volleyball players (mean age 22.8 ± 4.31 , mean playing history 4.56 ± 2.43), 25 soccer players (mean age 25.08 ± 2.53 , mean playing history 5.84 ± 1.84) and 30 non-athletes (mean age 23.23 ± 3.71).

The players completed questionnaires about age, playing post, past or current shoulder injuries, duration of dominant and non-dominant glenohumeral joints were made by Leighton flexometer ($r = 0.90 - 0.99$) in standard position. Goniometric measurement of the glenohumeral joint is difficult because of the multi-joint nature of the shoulder complex. In general, the literature would appear to indicate that the Leighton flexometer is a reliable measuring tool, especially when used by a single experienced tester.

All ROMs of subjects were measured in the morning and before play or participating in warm-up drills. No goniometric measurements were taken in the afternoon or after participating in play or warm-up drills to minimize the effect of intense activity or play on range of motion. All testing took place with the subject in a standard position in special bar and plastic cast and stabilized scapula by three special wide tapes on the hip, chest and head areas. Shoulder external and internal rotations were measured with the arm positioned in 90° of glenohumeral abduction and 90° of elbow flexion. During testing, the subjects were asked to actively move the joint as far as possible through the range of motion (**Graph 1**). For each direction, three measurements were taken and the mean measurements were calculated. We performed t- test on dominant versus non-dominant hands of subjects for all measurements. Correlation coefficients were computed to determine the strength of the relationships among variables. We analyzed these groups



Graph 1. Flexion & hyper extension measurements position (photo from Ackland *et al.* [6]).

and the relationship between shoulder ROM and age, post and history of play were analyzed by ANOVA and Post hoc Scheffe test.

2.1. Reliability of the Measuring Method

The commonly used clinical methods for detecting muscle tightness, described by Kendall [11] are subjective. When precision and objectivity are needed, estimation of range of motion by eye (eyeballing) is too inaccurate and therefore a goniometer was used in this research. Also, standardized methods of joint motion measurement by American academy of orthopedic surgeons (AAOS) 1966 and others were advised [12]. The measuring device is always important. In addition to the accuracy of a measuring device, an instrument should be easy to be used by the tester and comfortable for the subjects. Certain joint movements, especially axial rotations are more difficult to measure than others and that with a standard universal goniometer, axial measurements are only approximates [13].

In this study all ROMs were measured with the Leighton flexometer, model WA, Spokane because it was valid, reliable, easy to use and it has been frequently used by other researchers. There are sufficient studies to prove the reliability of the Leighton flexometer: Leighton [14], Bloomfield *et al.* [6], and Daneshmandi [3]. The reliability and validity of this device were proved by the researchers. Ekstrand *et al.* [15] also used the Leighton flexometer to measure the hip ROM in soccer players.

3. RESULTS

The results of the present study showed that the volleyball players were also less flexible than other soccer players and non-athlete groups for internal rotation ($p \leq 0.05$).

The results of this study showed significant differences of ROM of medial rotation of the shoulder in the four

groups of subjects included non-athletes, volleyball players, handball players and soccer players ($p \leq 0.05$) (Table 1 and Figure 1). Additionally, the results of this study showed that the ranges of motion of medial rotation of handball players were less than the other groups ($p \leq 0.05$).

The findings of this research showed significant differences between dominant and non-dominant hands of players ($p \leq 0.05$) (Figures 2 & 3).

The amplitudes of motion of the dominant and non-dominant shoulder joints in all groups were not similar and statistically there was a significant relationship between shoulder's ROMs of the dominant hand and shoulder's ROMs of the non-dominant hand. In other words, there are significant differences in external rotation between dominant and non-dominant hands of handball players ($p \leq 0.05$).

Table 1. Glenohumeral range of motions for all groups

	Flexion	Extension	Int. rotation	Ext rotation	Abduction
Handball	185.03 \pm 8.84	56.63 \pm 10.05	56.5 \pm 10.78	117.92 \pm 9.12	184.03 \pm 7.77
Volleyball	185.48 \pm 7.38	58.36 \pm 5.67	58.52 \pm 7.24	118.44 \pm 9.18	178.60 \pm 8.44
Soccer	181.72 \pm 6.54	57.04 \pm 8.86	59.44 \pm 4.95	108.20 \pm 11.84	178.84 \pm 8.97
Non athletic	184.70 \pm 7.88	57.63 \pm 8.28	63.66 \pm 10.12	116.26 \pm 7.97	183.80 \pm 6.84

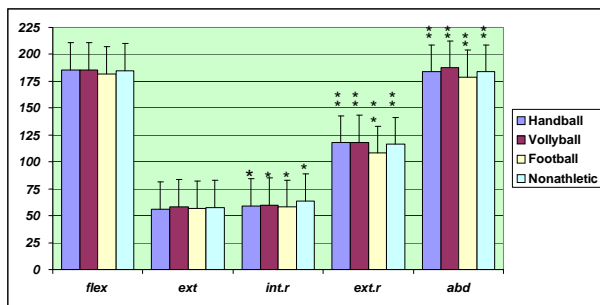


Figure 1. Glenohumeral range of movements for all groups.

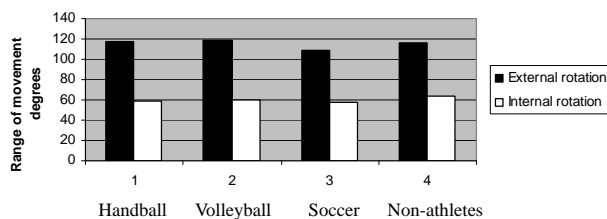


Figure 2. Glenohumeral joint rotation of dominant hand.

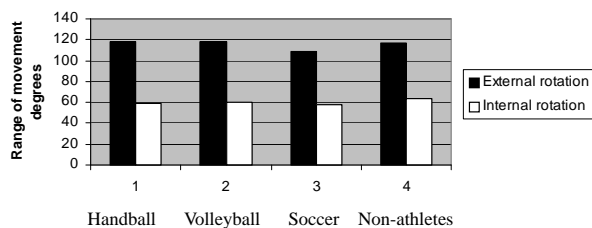


Figure 3. Glenohumeral joint rotation of non-dominant hand.

The results also showed that by increasing age, the external rotation of soccer players and non-athletes were reduced (Figure 4) and also by increasing year of tournament play, shoulder ROM decreased but this deficit not significant. There are significant differences of shoulder external and internal rotation between groups of subject and between different playing post of athletes: internal rotation in handball players ($p \leq 0.05$), internal and external rotation in volleyball players ($p \leq 0.01$) and external rotation in soccer players ($p \leq 0.05$).

4. DISCUSSION

The physiologic adaptations of athletes appear to be sport specific [16]. This study was designed to measure glenohumeral range of motion, which has been implicated as a possible etiologic factor in increased glenohumeral translation. Measurement of glenohumeral flexion, extension and abduction were not reported because they have not been implicated as factors in increased glenohumeral translation and because abduction also involves motion in joints other than the glenohumeral joint [17].

The results of this study showed that by increasing age and years of tournament play, internal and external rotations of shoulder in all groups were reduced. But this reduction in all groups was not significant, because range of age and years of tournament play as well as sets and time of training per week were less in the elite athletes in some countries. Increasing age and years of tournament play in athletes caused the changes in musculoskeletal structure. This adaptation may be positive or negative, for example an increase in force and masse of muscles or a change in range of motion of joints always obtained by training. Flexibility and tightness of soft tissues around joints and finally reduce range of motion

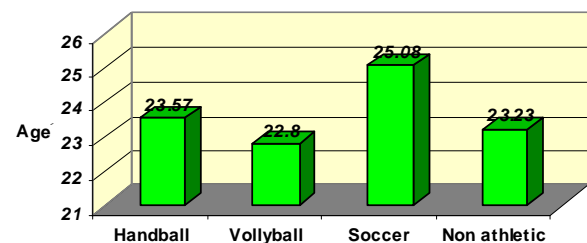


Figure 4. ROM and age.

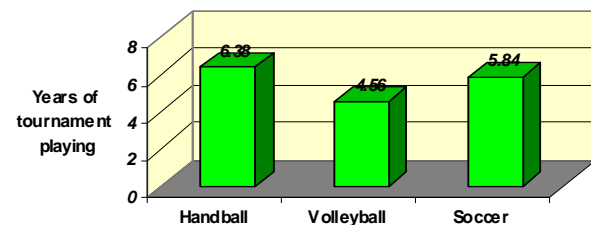


Figure 5. Mean years of history playing.

of joints as well [18,19]. If the normal flexibility of the surrounding tissue of a joints is not maintained, over a period of time a decrease in joint range of motion could happen leading to a possible decrease in performance or an increase in chance of injury [4,5].

In this study, the range of external and internal shoulder rotations was different in sports and in playing posts of athletes, which can be related to their specific sport demands and emphasizes this point that flexibility is very specific in any joint, playing post and sport field. Glenohumeral internal rotation of handball and volleyball players was less than other groups in this study. A reduction in shoulder internal rotation, particularly in the dominant side, can be explained as an adaptation of the posterior shoulder musculature and capsular structure to the handball and volleyball stroke. The increase in external rotation of shoulder in these athletes is also a likely adaptation to the overhead movement in these sports. The occurrence of an excessive range of external rotation may be a product of a successful training program to increase movement and thus the range over which force can be applied to throwing or stroke [19,20].

The implication of this point is that excessive external shoulder rotation can create excessive anterior humeral head displacement [17,21,22]. Current research has convincingly showed that deficits of internal rotation of shoulder occur as the athlete adapts to the demands of the sport. It is unclear whether these are normal adaptations that are beneficial, either locally or throughout the kinetic chain, or whether these are mal-adaptations that create potentially harmful local or kinetic chain biomechanics. Also, the role this adaptation may play in injury causation or risk is unclear. Several recent papers suggest that decreased internal rotation and total rotation may adversely affect shoulder performance, and this effect may increase the risk of injury [22,23].

There are studies which show that inflexibility is a risk factor for further injury [24,25]. Achievement of full range of motion is one of the first goals in rehabilitation programs [20,22]. Most shoulder rehabilitation protocols now emphasize on a corrective exercise for internal rotation of shoulder of athletes.

The study of water polo players showed that special repetitive movement in water polo is the same as baseball and handball throwing, volleyball service and stroke and other sports with overhead movements. All these sports emphasize shoulder adduction and internal rotation that cause force, torque and mass of adductor and internal rotator muscles can lead to reduction of these ROMs [2,26].

The study of shoulder movement suggests that decreased internal and total rotation may not be optimal

conditions to allow the best athletic performance with minimal risk of injury. From a performance standpoint, these conditions create inefficient biomechanics that interfere with normal coupled motion and may decrease optimal arm momentum. This paper showed degrees of asymmetry in dominant and non-dominant hands of handball and volleyball players. If we do not note it carefully and do not use correct stretch exercise program, this imbalance in musculature of shoulder girdle leads the athletes to decrease their performance or an increase in the chance of injury. For example, Young *et al.* [27] reported a prevalence imbalance in musculature of shoulder girdle and scoliosis in volleyball players rather than in non-athletic groups. Improvement of imbalance musculature due to hard training created scoliosis in volleyball players. Therefore, if handball and volleyball players train more and harder bilaterally, this maladaptation will be rapid.

5. CONCLUSIONS

Once again the results of this research showed the limitation of shoulder ROM in athletes. On the basis of this study and other investigations, it could be suggested that the specific demands, poor training, particularly lack of adequate flexibility exercises and inadequate warm-up exercises for shoulder, may be responsible for such problems. Exercising muscles without an appropriate stretching exercise program tends to decrease the motion in shoulder joints.

Very importantly, the overall (contact or non-contact sports), hard and stressful competitions, over-training, exhausting repeated movements, faulty techniques, previous injuries and probably anthropometric characteristics of players can be also considered as other factors involved in the limitation of shoulder flexibility. However, each factor will need more research.

Also, it can be recommended that more stretching exercises should be considered for older and experienced players and specific stretching exercises are recommended for different sports and playing posts. Based on the demands of any sport, coaches and athletes should apply corrective exercise programs to prevent muscular imbalance in shoulder girdle.

Much more work is needed to study the exact implications of our findings. Several directions for future study are raised by this study. Can these deficits be modified and, if so, what is the most efficient method of modification? If they are modified, what is the relationship between performance and risk of injury? Do these deficits continue to decline in a linear direction, or is there a curvilinear pattern with an absolute maximum? Were these deficits compounded by variables such as the amount of weight training exercises and previous childhood activities?

REFERENCES

- [1] Chung, M.-J. and Wang, M.-J.J. (2009) The effect of age and gender on joint range of motion of worker population in Taiwan. *International Journal of Industrial Ergonomics*, **39**(4), 596-600.
- [2] Crockett, H.C. (2002) Osseous adaptation and range of motion at the glenohumeral joint in professional baseball pitchers. *American Journal of Sports Medicine*, **30**(1), 20-26.
- [3] Hassan, D. and Shacklady, C. (2002) Hip rotation flexibility in professional athletes. *International Journal of Collected Academic Articles*, **1**, 81.
- [4] Hall, S.J. and Martin, M. (2002) Sport injury management. Williams & Wilkins, Philadelphia.
- [5] Chandler, T.J., Kibler, W.B., Uhl, T.L., Wooten, B., Kiser, A. and Stone, E. (1990) Flexibility comparisons of junior elite tennis player to other athletes. *American Journal of Sports Medicine*, **18**(2), 134-136.
- [6] Ackland, T.R., Elliott, B.C. and Bloomfield, J. (1995) Applied anatomy and biomechanics in sport. Human Kinetics Publishers, Champaign.
- [7] Holland, G.J., *et al.* (2002) Flexibility and physical functions of older adults: A review. *Journal of Aging and Physical Activity*, **10**(2), 169-206.
- [8] Kugler, A., Krüger-Franke, M., Reininger, S., Trouillier, H.H. and Rosemeyer, B. (1996) Muscular imbalance and shoulder pain in volleyball attackers. *British Journal of Sports Medicine*, **30**(3), 256-259.
- [9] Alter, M.J. (1996) Science of stretching. Human Kinetics Publishers, Champaign.
- [10] Tveitå, E.K., *et al.* (2008) Range of shoulder motion in patients with adhesive capsulitis; Intra-tester reproducibility is acceptable for group comparisons. *BMC Musculoskeletal Disorders*, **9**, 49.
- [11] Kendall, F., *et al.* (2005) Muscle testing and function with posture and pain. 5th Edition, Lippincott Williams & Wilkins Publisher, Philadelphia.
- [12] Norkin, C.C. and White, D.J. (1995) Measurement of joint motion: A guide to goniometry. 2nd Edition, F. A. Davis Company, Philadelphia.
- [13] Ellenbecker, T.S., *et al.* (1996) Glenohumeral joint internal and external rotation range of motion in elite junior tennis players. *Journal of Orthopaedic & Sports Physical Therapy*, **24**(6), 336-341.
- [14] Leighton, J.R. (1957) Flexibility characteristics of three specialized skill groups of champion athletes. *Archives of Physical Medicine and Rehabilitation*, **38**(9), 580-583.
- [15] Ekstrand, J., *et al.* (1982) Lower extremity goniometric measurement: A study to determine their reliability. *Archives of Physical Medicine and Rehabilitation*, **63**(4), 171-175.
- [16] Harryman, D.T., *et al.* (1992) The role of the rotator interval capsule in passive motion and stability of the shoulder. *The Journal of Bone and Joint Surgery*, **74**(1), 53-66.
- [17] Reagan, K.M., *et al.* (2002) Humeral retroversion and its relationship to glenohumeral rotation in the shoulder of college baseball player. *American Journal of Sports Medicine*, **30**(3), 354-360.
- [18] Leatt, P., *et al.* (1987) Specific muscular development in under-18 soccer player. *Journal of Sports Sciences*, **5**(2), 165-175.
- [19] Herington, L., *et al.* (1998) Glenohumeral joint: Internal and external rotation range of motion in javelin throwers. *British Journal of Sports Medicine*, **32**(3), 226-228.
- [20] Silliman, J.F. and Hawkins, R.J. (1991) Current concepts and recent advances in the athlete's shoulder. *Clinics in Sports Medicine*, **10**(4), 693-705.
- [21] Wilk, K.E., *et al.* (2002) Current concepts in the rehabilitation of the overhead throwing athlete. *American Journal of Sports Medicine*, **30**(1), 136-151.
- [22] Wilk, K.E., *et al.* (1997) Current concept: The stabilizing structures of the glenohumeral joint. *Journal of Orthopaedic & Sports Physical Therapy*, **25**(6), 364-379.
- [23] Kibler, W.B. (1995) Clinical examination of the shoulder: Athletic injuries of the shoulder. McGraw-Hill, Inc., New York.
- [24] Kibler, W.B., Chandler, T.J. and Pace, B.K. (1992) Principles of rehabilitation after chronic tendon injuries. *Clinics in Sports Medicine*, **11**(3), 661-671.
- [25] Pieper, H.G. (1998) Humeral torsion in the throwing arm of handball players. *American Journal of Sports Medicine*, **26**(2), 247-253.
- [26] McMaster, W.C., *et al.* (1992) Shoulder torque changes in the swimming athlete. *American Journal of Sports Medicine*, **20**(3), 323-327.
- [27] Kim, Y.K., *et al.* (2003) The relationship between humeral retroversion and shoulder rotation in maggot league baseball pitchers. 5th Asian Federation of Sports Medicine Congress, Seoul, 15 September 2003.

Use of instantaneous energy of ABR signals for fast detection of wave V

Adeela Arooj, Mohd Rushaidin Muhamed, Sheikh Hussain Shaikh Salleh, Mohd Hafizi Omar

Center for Biomedical Engineering, Faculty of Biomedical and Health Science Engineering, University Technology Malaysia, UTM Skudai, Johor, Malaysia.

Email: dradeelaarooj@yahoo.com

Received 16 December 2009; revised 28 January 2010; accepted 31 May 2010.

ABSTRACT

Brainstem evoked response audiometry is a powerful diagnostic technique in audiology, otology and neurology. ABR(Auditory Brainstem Response) machine has been very useful and popular in past two decades for detection of hearing defects and pathologies in newborns and children. In ABR, wave V is the most prominent and robust wave that has been used as indicator of hearing loss. However, a fast detection of the wave V is necessary in order to implement newborn hearing screening. Researchers have introduced different kind of signal processing technique in order to achieve this target and one of this is Fast Fourier Transform (FFT) and Wavelet Transform. In this study, the instantaneous energy of ABR signal had been introduced as a marker to identify the ABR waves. Study showed that the instantaneous energy of auditory brainstem response can be used as a marker to identify the ABR waves. This study had proposed a platform for fast hearing screening system.

Keywords: Auditory Brainstem Response; Neonate; Hearing Screening; Instantaneous Energy

1. INTRODUCTION

1.1. Newborn Hearing Screening

Hearing screening of neonates is the key to prevent the most serious consequences of hearing loss. One of the most common neurosensory handicaps in newborns and children is congenital hearing loss [1,2]. Hearing plays a basic role in speech, intellectual and language development. The importance of early detection and rehabilitation of infants with hearing impairment cannot be overstated. Unfortunately, the average time between birth and the detection of congenital sensorineural (SN) hearing loss is 2.5 years. The American Joint Committee on Infant Hearing recommended that audio logical reha-

bilitation should begin within the first 6 months of life (3). In cases with pronounced hearing loss even no speech ability will be developed at all causing serious communication problems and impaired intellectual and emotional development. The consequences of being deaf-mute are the needs of special schools and care, social isolation and no development of potential skills. Thus there are serious medical and economical consequences for the entire society due to this problem [1].

According to the World Health Organization, 5 per 1,000 neonates are born with significant hearing loss. Data on prevalence of congenital Permanent Childhood Hearing Impairment (PCHI) differs from country to country. The prevalence of PCHI has been estimated to be 1.1-1.5 for every 1000 live births in Estonia, 1 in 900 in the UK to 1 in 2500 newborns in Atlanta, Georgia. The prevalence of Hearing loss is variable among different races, birth weight and other pregnancy risk factors. It is 10-20 times higher in high risk babies as compared to normal babies.

In Malaysia, there is no published data on the actual prevalence of hearing impairment in children. Estimated figures obtained from the Statistics Division, United Nations Economic and Social Commission for Asia and the Pacific (ESCAP) (2002) indicate that Malaysia with a total population of 23.8 million and birth rate of 23.5 per 1000 population has about 559,000 babies born in a year. If the prevalence of hearing loss of 1.5 in every 1000 live births is applied in our population, a rough estimate is that about 840 babies with hearing loss are born each year in this country [2]. However, one study case have been done to determine the prevalence of hearing loss among newborns delivered at Hospital University Malaya shows that the prevalence is 0.42% (16/3,762) [3].

All over the world, strategies used in UNHS are based on otoacoustic emissions (OAE) and auditory brainstem response (ABR). Particularly, methods based on ABR are well-considered due to their high specificity and

sensitivity rates, and their high correlation between impairment and alteration in the ABR pattern [4]. OAE testing evaluates the integrity of the inner ear (cochlea). In response to noise, vibrations of the hair cells in a healthy inner ear generate electrical responses, known as otoacoustic emissions. The absence of OAEs indicates that the inner ear is not responding appropriately to sound [5]. There are two types of OAE screening techniques, Transient Evoked Otoacoustic Emissions (TEOAEs) and Distortion Product Otoacoustic Emissions (DPOAEs) [5,6].

The Auditory Brainstem Response (ABR) is one of the most widely used auditory evoked potentials (AEP). The ABR is a far-field, differentially averaged, electrophysiologically recorded signal. It represents the summed and averaged responses of thousands of nerve fibres to repeated acoustic stimulation [7]. The stimulus is delivered via earphones or an inserted ear probe and scalp electrodes are used to pick up the signal. ABR evaluates the integrity of the peripheral auditory system and the auditory nerve pathways up to the brainstem and is able to identify infants who have normal cochlear function but abnormal eighth-nerve function (auditory neuropathy) [5]. Detection of wave V in the ABR measurements is the most reliable objective diagnosis and quantification of hearing loss in children [8-11]. Due to a poor signal-to-noise ratio, 2000-4000 sweeps have to be averaged to obtain a meaningful, visually noticeable signal at a particular stimulation level [12].

Usually in Malaysia, Hearing Screening is done when babies are brought to the Maternal Child Health Clinics or private clinics for their routine immunization using the Infant Distraction Test or when children fail to attain normal language milestones (personal communication). Recently, newborn hearing screening has been introduced in a few hospitals on a regular basis in the Klang Valley. In other centers, babies with high risk factors such as prolonged NICU stay, craniofacial anomalies or previous history of meningitis are usually referred earlier for a full audiological assessment. Typically, screening programs use a 2-stage screening approach, either OAE repeated twice, OAE followed by ABR, or ABR repeated twice, or use a 3-stage screening approach, OAE repeated twice and followed by ABR [13,14]. NHS programs are commonly conducted as multiple stage procedures. **Figure 1** shows the implementation of universal NHS in the state of Saarland, Germany [6].

1.2. ABR Recording System

In 1984, an automated electric response audiometry recording system has been developed [15]. It uses Nascom 2, an 8 bit microcomputer with a Z80A processor running at 4 MHz, 32 KB RAM and 8 input/

output ports, 12 bit analog to digital converter, low noise differential amplifier, optically isolated amplifier and DC to DC converter. An electro-sensitive printer has been used to record the patient information and the ABR result. The gain of the amplifier depends on the full-scale voltage range of the A-D converter and minimum voltage input requirements [16]. Typical gain values for evoked response systems range from 10,000-500,000 [16-22]. Taking care of the gain of the amplifier is important. It must be low enough to avoid saturation [23].

Frequency bandwidth is important in order to get the correct range for the signal. The frequency bandwidth of the ABR signal, typically range from 20 Hz-5 kHz [24-26]. This bandwidth will pass the wave V and slow SN10 components of the ABR which are important in the estimation of hearing thresholds. There are variety of sampling rate value with variety of resolution bits that has been used to sample the ABR signal; 12.8, 20 and 50 kHz; 12 and 16 bit [19,20,26].

1.3. Wave V Detection

Various kinds of methods have been introduced for detection of ABR waves. Woodworth *et al.* [9], introduced a matched filter technique, derived from an ABR obtained at high stimulus level in order to calculate wave V latency at lower intensity level as shown in **Figure 2**. Strauss *et al.* [12], introduced an approach for detection of ABRs using a smart single sweep analysis system. The method used a small number of sweeps which is decomposed by optimized tight frames and evaluated by a kernel based novelty detection machine [12]. Delgado and Ozdamar [18], mentioned that results of spectral analysis, spectral filtering and fiber-tract modeling of ABRs were used to determine the most suitable filters to detect the position of the various peaks. These analyses revealed general trends in ABR

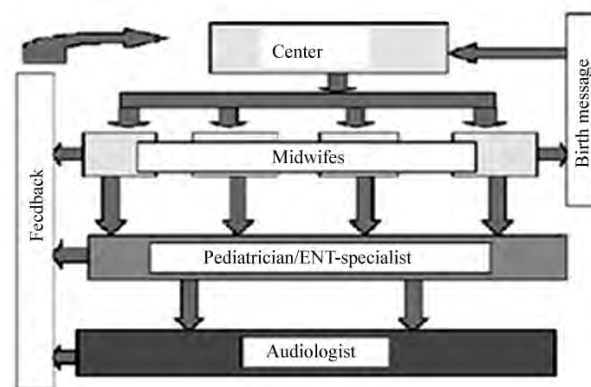


Figure 1. Organization of 3 stage universal NHS Program (implemented in the state of Saarland, Germany)

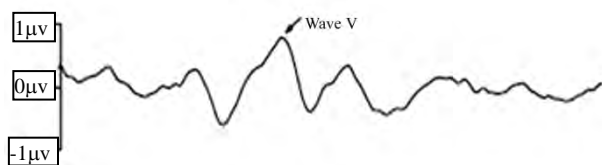


Figure 2. Detection of wave V in ABR.

composition from one intensity to another and were used to write labeling rules [18]. Wilson and Aghdasi [15], used a Discrete Wavelet Transform (DWT) of ABR signals in order to detect the ABR waves. The wavelets technique is used to decompose a signal into discrete sets of details (high frequencies) and approximations (low frequencies). The different scaled signals are then rebuilt from their resulting wavelet coefficients and analyzed in a method similar to the full signal analysis [24]. In this study, the instantaneous energy of ABR signal has been introduced as a marker to identify the ABR waves. Instantaneous energy technique has previously been employed in other applications of ECG and heart sound signal processing, such as heart sound segmentation [27,28].

2. MATERIALS AND METHODS

2.1. Experiment Setup

Figure 3 shows the diagram of the hardware system setup. It consists of (A) gTec USBamp, a biosignal amplifier and data acquisition machine, (B) gPAH, a programmable attenuator, (C) trigger box, (D) headphone, (E) laptop, (F) MP3 player and (G) electrodes. The gTec USBamp was used to amplify and acquire the ABR signals. The gPAH was used to attenuate the click stimulus produced by MP3 player. MP3 player could be replaced by a laptop as well. The study was done on infants at Pusat Kesihatan (Health Clinic) UTM, JB, Malaysia. The infants were included in the study after a written consent signed by their parents. Our Team included biomedical engineers, nurses and medical doctor. Under supervision of medical doctor, the electrodes were applied by nurses on the infant's frontal parietal (FP) area and mastoid process. Trigger box was used to produce trigger signal from the click stimulus where as different laptops were used in the experiments in order to get smooth clicks. The triggered signal was used to segment the ABR signals. The recorded signals were transferred to a laptop by gTec USBamp via USB port. The recorded signal was filtered at bandwidth ranges from 100 Hz-3000 kHz. The click stimulus rate was setup at 10 clicks sec^{-1} and the signal was sampled at 19.2 kHz with 24 bit resolution. The stimulus intensity levels used in the experiments are 80, 70 and 60 dBnHL. The signals were averaged after 2048 click stimulus

repetitions. **Figure 4** shows the electrode's configuration used in the experiments. The positive electrode (channel 1) was connected to FP2, the negative electrode (reference) was connected to mastoid and ground electrode was connected to forehead. The FP2 IS 10% from nasion on the right side of parietal bone.

Matlab R2006a simulink software had been used to capture the raw ABR signals from the gTec USBamp and analyze the signals. However, few configurations need to be carried out using the Matlab model. The analysis algorithm was written in Matlab M-file format.

3. RESULTS AND DISCUSSION

Figure 5 shows the presentation of the ABR averaged signal and the instantaneous energy of the averaged signal. **Figure 5(a)** shows the result acquired from a normal person and **Figure 5(b)** shows the result acquired from a hearing loss person. Both signals are recorded with the intensity of 80 dB. On the ABR averaging signal graph shows three different averaged signals.

The signals are plotted on three different baselines, 0, 1

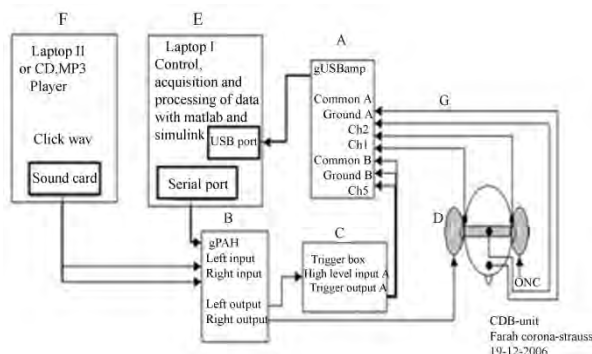


Figure 3. Diagram of the hardware system setup.

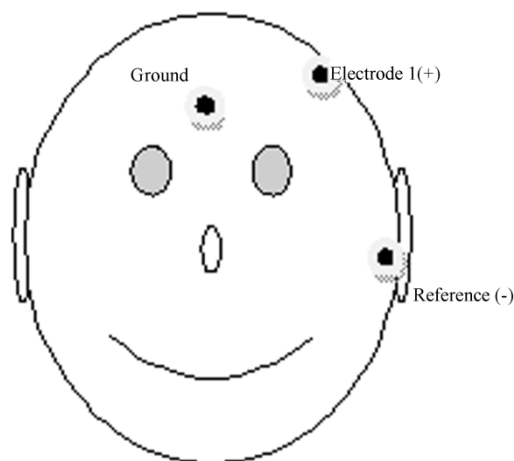


Figure 4. Electrodes configuration.

and 2 μV respectively. The averaged signal on the 0 baseline used is 500 sweeps, the averaged signal on the 1 baseline used is 250 sweeps, on the 2 baseline used is 125. The dotted vertical line marked the latency of wave V. It can be observed that wave V occurred at specific points in the signal of normal person, **Figure 5(a)**, but did not occur in the signal of hearing loss person, **Figure 5(b)**. **Table 1**

shows the summary of the graph. The normal subject showed results with the latency 5.313 m/sec and amplitude range from 0.335-0.235 μV . The hearing loss subject showed result with the latency 5.156msec and amplitude range from -0.9288 to -0.707 μV .

The objective of the study is, to investigate the effectiveness of instantaneous energy for the detection of

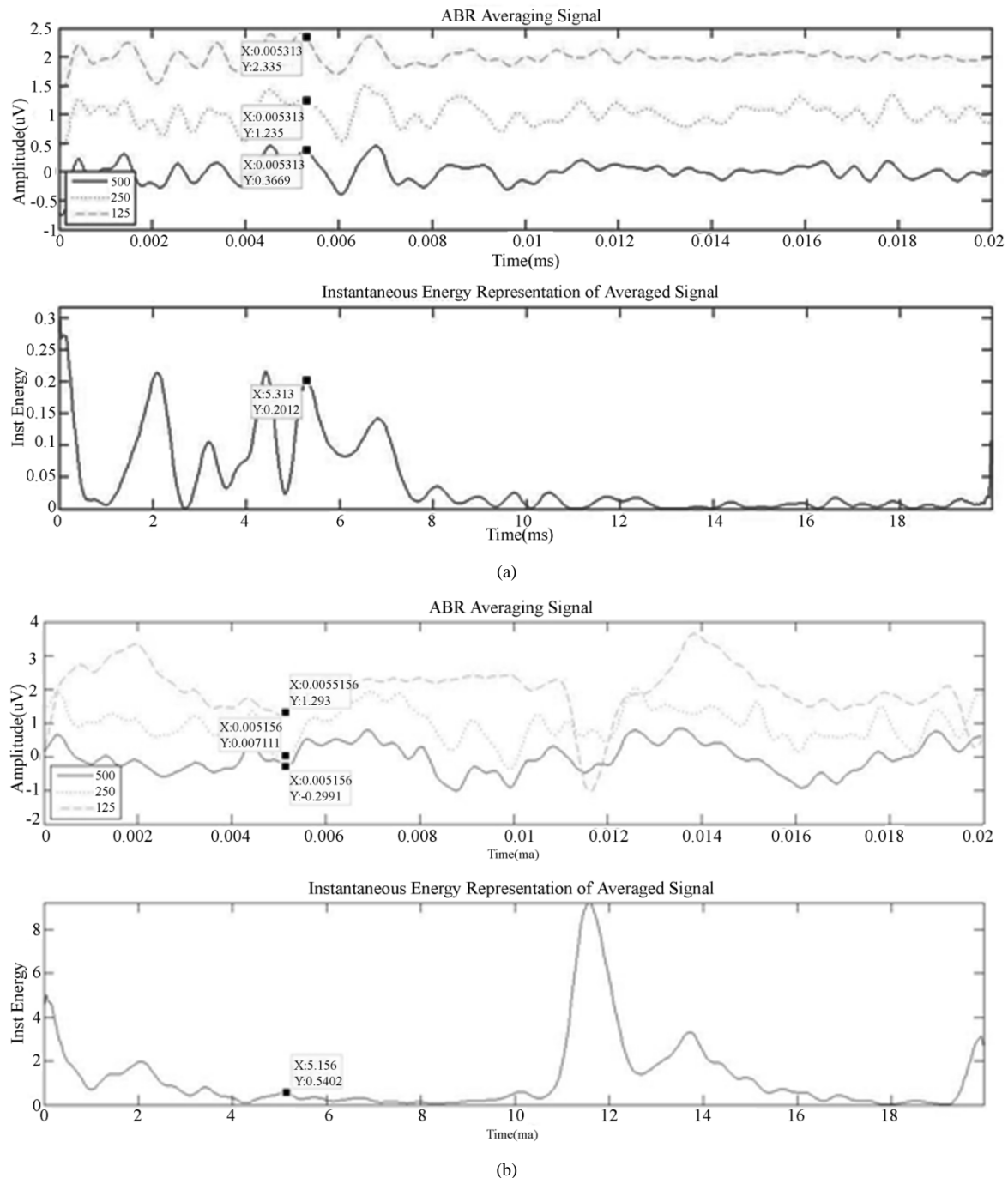


Figure 5. Wave V detection using instantaneous energy of ABR signal on (a) normal subject (b) hearing loss subject

Table 1. Summary of **Figure 5**.

Subject	Intensity (dB)	Latency (ms)	500 sweeps (uV)	250 sweeps (uV)	125 sweeps (uV)
Normal	80	5.313	$0.3669 - 0 = 0.3669$	$1.235 - 1 = 0.235$	$2.335 - 2 = 0.335$
Hearing loss	80	5.156	$-0.2991 - 0 = -0.2991$	$0.007111 - 1 = -0.99288$	$1.293 - 2 = -0.707$

Table 2. Mean, standard deviation, and variance of the Averaging signal and its Instantaneous Energy.

No. of sweeps	IE			Avg		
	Mean(msec)	Standard deviation	Variance	Mean(msec)	Standard deviation	Variance
1000	5.23008	0.40246	0.16197	5.19092	0.40615	0.16496
800	5.23442	0.41394	0.17135	5.19967	0.40035	0.16028
625	5.25175	0.36077	0.13015	5.18658	0.39949	0.15959
500	5.25608	0.3508	0.12306	5.22575	0.38868	0.15107
250	5.28217	0.55715	0.31042	5.26908	0.40694	0.1656
125	5.22125	0.42306	0.17898	5.16483	0.37817	0.14301
100	5.1475	0.4778	0.2283	5.02608	0.49029	0.24039
80	5.1735	0.44885	0.20146	5.05208	0.45242	0.20468
50	5.20817	0.40954	0.16772	5.04342	0.41723	0.17408
40	5.23008	0.43164	0.18631	5.19092	0.46978	0.22069
20	5.25175	0.49195	0.24202	5.21267	0.4842	0.23445
10	5.20408	0.44679	0.19962	5.17367	0.43821	0.19203

ABR waves. ABR is an important clinical tool in the identification and quantification of hearing impairment. It is objective, noninvasive and unaffected by sleep or drugs. Different signal detection techniques have been developed and evaluated to improve test efficiency and reliability [18]. The detection of responses at threshold levels is not trivial and requires an experienced professional. The amplitudes, a , in the **Table 1** are obtained by deduction of amplitude appeared on the graph from the baseline. Thus, a , can be written as

$$a = b - c \quad (1)$$

where:

a = The real amplitude

b = The graph amplitude

c = The baseline

The latency of the signals is obtained by considering the intensity of the click and the peak of instantaneous energy of the signal which is near the latency value that has been referred to the latency curve published by Woodworth *et al.* [19]. For the intensity of 80 dB, the latency curve shows that the latency should be within 5 m sec. In **Figure 5(a)**, the peak of the instantaneous energy is 0.2012 which is near the latency within 5 m sec. In **Figure 5(b)**, the peak of the instantaneous energy that near the latency within 5 ms is 0.5402. Instantaneous energy can detect wave 'V' even at lower sweeps while

some other techniques require higher number of sweeps.

Table 2 is showing mean, standard deviation and variance of averaged signal and instantaneous energy on time domain. From the table it's obvious that use of instantaneous energy is equally effective in capturing wave 'V' of ABR. So it can be concluded that this is a comparably effective technique. However, the limitation is noise disturbance which interferes with detection of ABR waves. A few false negative results were also noted but hopefully in future there will be improvement in technology and these problems will be overcome.

4. CONCLUSIONS

A new method of ABR wave detection has been designed. The new method of the ABR wave's detection such as described in this study is important in order to detect the hearing loss faster especially for infants and children. The results have shown in this study states that instantaneous energy of ABR signal can be used as marker in order to detect ABR waves. The performance of this method needs to be tested further.

5. ACKNOWLEDGEMENTS

This research project is supported by CBE (Center for Biomedical Engineering) at University Technology Malaysia and funded by University Technology Malaysia (UTM), Malaysia under grant

“Universal Hearing Screening in Malaysia Based On A Cost Efficient Organization Structure Using An Innovative ABR Technology: The Johor Screening Scheme” Vot 77013.

REFERENCES

- [1] Yoshinaga-Itano, C. (1999) Benefits of early intervention for children with hearing loss. *Otolaryngol. Clinics of North America*, **32**(6), 1089-1102.
- [2] Sivalal, S. (2005) Screening for hearing loss in infants. *Health Technology Assessment Report*. <http://www.moh.gov.my/MohPortal/DownloadServlet?id=717&type=2>
- [3] Joint Committee on Infant Hearing (1982) Position statement. American Academy of Paediatrics. *Pediatrics*, **70**, 496-497.
- [4] American Academy of Pediatric (1999) Newborn and infant hearing loss: Detection and intervention. *Pediatrics*, **103**, 527-530.
- [5] Helfand, O.M., Thompson, D.C., Davis, R., McPhillips, H., Homer, C.J. and Lieu, T.L. (2001) Newborn hearing screening: Systematic evidence review. AHRQ Publication No. 02-S001, Agency for Healthcare Research and Quality, Rockville.
- [6] Delb, W., Merkel, D., Pilorget, K., Schmitt, J. and Plinkert, P.K. (2004) Effectiveness of a teoae-based screening program. Can a patient-tracking system effectively be organized using modern information technology and central data management? *European Archives of Otorhinolaryngology*, **261**(4), 191-196.
- [7] Hall III, J. (1992) Handbook of auditory evoked responses. Allyn and Bacon, Needham Heights.
- [8] Wicke, J.D., Goff, W.R., Wallace, J.D. and Allison, T. (1978) On-line statistical detection of average evoked potentials: Application to evoked response audiometry (ERA). *Electroencephalography and Clinical Neurophysiology*, **44**(3), 328-343.
- [9] Woodworth, W., Reisman, S. and Fointaine, A.B. (1983) The detection of auditory evoked responses using a matched filter. *IEEE Transactions on Biomedical Engineering*, **30**(7), 369-376.
- [10] Mason, S.M. and Adams, W. (1984) An automated microcomputer based electric response audiometry system for machine scoring of auditory potentials. *Clinical Physics and Physiological Measurement*, **5**(3), 219-222.
- [11] Shangkai, G. and Loew, M.H. (1986) An autoregressive model of the BAEP signal for hearing threshold testing. *IEEE Transactions on Biomedical Engineering*, **33**(6), 560-565.
- [12] Strauss, D.J., Delb, W., Plinkert, P.K. and Schmidt, H. (2004) Fast detection of wave V in ABRs using a smart single sweep analysis system. *Proceedings of the 26th Annual International Conference of the IEEE Engineering in Medicine and Biology Society*, IEEE Xplore Press, **1**, 458-461.
- [13] Abdullah, A., Hazim, M.Y.S., Almyzan, A., Jamilah, A.G. and Roslin, S., *et al.* (2006) Newborn hearing screening: Experience in a Malaysian hospital. *Singapore Medical Journal*, **47**(1), 60-64.
- [14] Clemens, C.J., Davis, S.A. and Bailey, A.R. (2000) The false-positive in universal newborn hearing screening. *Pediatrics*, **106**(1), e7.
- [15] Wilson, W.J. and Aghdasi, F. (1999) Fast Fourier transform analysis of the auditory brainstem response: Effects of stimulus intensity and subject age, gender and test ear. *AFRICON, IEEE*, **1**, 285-290.
- [16] American Speech-Language-Hearing Association (1987) Short latency auditory evoked potentials. ASHA Practice Policy.
- [17] Neely, S. and Liu, Z. (1998) ABRAB: Auditory brainstem response average. <http://www.boystownhospital.org/Media/Research/abravtm.pdf>
- [18] Delgado, R.E. and Ozdamar, O. (1994) Automated auditory brainstem response interpretation. *IEEE Engineering in Medicine and Biology Magazine*, **13**(2), 227-237.
- [19] Dajani, H.R., Purcell, D., Wong, W., Kunov, H. and Picton, T.W. (2005) Recording human evoked potentials that follow the pitch contour of a natural vowel. *IEEE Transactions on Biomedical Engineering*, **52**(9), 1614-1618.
- [20] Boston, J.R. (1981) Spectra of auditory brainstem responses and spontaneous EEG. *IEEE Transactions on Biomedical Engineering*, **28**(4), 334-341.
- [21] Wilson, W.J. and Aghdasi, F. (2001) The importance of pre-analysis windowing on auditory brainstem response fast Fourier transform analysis. *Scandinavian Audiology*, **30**(1), 3-12.
- [22] Wilson, W.J. (2004) The relationship between the auditory brain-stem response and its reconstructed waveforms following discrete wavelet transformation. *Clinical Neurophysiology*, **115**(5), 1129-1139.
- [23] Bell, S.L., Smith, D.C., Allen, R. and Lutman, M.E. (2004) Recording the middle latency response of the auditory evoked potential as a measure of depth of anaesthesia. *British Journal of Anaesthesia*, **92**(3), 442-445.
- [24] Wilson, W.J. and Aghdasi, F. (1999) Discrete wavelet analysis of the auditory brainstem response: Effects of subject age, gender and test ear. *AFRICON, IEEE*, **1**, 291-296.
- [25] Beltran, N. and Cornejo, J.M. (2003) Simultaneous transient evoked otoacoustic emissions and auditory brainstem response for auditory evaluation. *Proceedings of the 25th Annual International Conference of the IEEE Engineering in Medicine and Biology Society*. IEEE Xplore Press, **4**, 3222-3224;
- [26] Strauss, D.J., Delb, W. and Plinkert, P.K. (2004) Objective detection of the central auditory processing disorder: A new machine learning approach. *IEEE Transactions on Biomedical Engineering*, **51**(7), 1147- 1155.
- [27] Malarvili, M.B., Kamarulafizam, I., Hussain, S. and Helmi, D. (2003) Heart sound segmentation algorithm based on instantaneous energy of electrocardiogram. *Computers in Cardiology*, **30**, 327-330.
- [28] Rushaidin, M.M., Salleh, S.-H., Swee, T.T., Najeb, J.M. and Arooj, A. (2009) Wave V detection using instantaneous energy of auditory brainstem response signal. *American Journal of Applied Sciences*, **6**(9), 1669-1674, 2009.

Tele-care for emergency announcements

Ching-Sung Wang¹, Chien-Wei Liu², Teng-Wei Wang³

¹Department of Electronic Engineering, Oriental Institute of Technology, Taipei, Taiwan, China;

²Department of Information Management, St. Mary's College, Yilan, Taiwan, China;

³The Third Department of Clinical Research Institute, Peking University, Beijing, China.

Email: ff020@mail.oit.edu.tw

Received 5 June 2010; revised 21 June 2010; accepted 22 June 2010.

ABSTRACT

The first aid and immediately help are very important in an accident. The earlier detection and treatment we do, the better prognosis and health patients have. In the senior populations, it is more important. Once seniors have an accident, not only physically injure in their body, but also mental and social ability, and may have severe sequela. Concerning about these populations, this research design a simple, practical, and portable device of real-time monitoring body activity with sphygmomanometer and pulsimeter. When an accident occurs, the signals go through mobile phone, immediately notify the remote ends and provide first time help.

Keywords: Real-Time; Monitoring; Mobile; Sphygmomanometer; Pulsimeter

1. INTRODUCTION

In 1991, American Heart Association suggests "The Chain of Survival" -Early Access, Early CPR, Early Defibrillation, and Early Advanced Care. It emphasizes that immediately after cardiac arrest, early CPR in the first 4 min. and early advance care in the first 8 min would have about 43% success rescue rate, on the contrary, lower than 20%. Cumnius, R.O.'s research points out that there is about 7-10% success rescue rate decreasing per minute delayed after patients' heart arrest [1]. In traumatic care, there is so called "golden hour" concept that means the first sixty minutes after the occurrence of multi-system trauma. It is widely believed that the victim's chances of survival are greatest if they receive definitive care in the operating room within the first hour after a severe injury (Committee on Trauma, 1993; Division of Trauma & EMS, 1992). For the cerebrovascular accident, it also points out "golden 3 hours", giving a proper deal in the first 3 hours after the accident occurring can increase the chance of survival. Whether what kind of emergency, they focus on immediately re-

sponse and properly deal, early detection and early treatment.

Accident is more important for the seniors, morbid populations and for those who have unstable life signs. According to studies, once seniors fall down, they would reduce their living activity [2,3], indirectly leveling down their life quality.

Based on people's habits, using mobile phone, this research suggests a device, real timely monitoring human body's activity with sphygmomanometer and pulsimeter, combining with mobile and Bluetooth etc. relative technology to edit a simple, practical, and suit for the current mobile phone that includes Bluetooth device. When the accident occurs, it can immediately and effectively provide relative rescuing information to remote GPS etc, expecting that is able to improve first aid effect. And, it provides senior population an effective preventing accident guarantee, enabling them to avoid decreasing their life activity caused by an accident.

2. SYSTEM ARCHITECTURE

This system divides into two parts, which are client side and server side respectively. Client side comprises BAD (Body Activity Detector) with sphygmomanometer and pulsimeter, GPS (Global Position System) device and mobile phone. Once BAD detected any unusual body responses, mobile phone would immediately delivers the emergent message by DTMF (Dual Tone Multi Frequency) coding with sphygmomanometer, pulsimeter and the GPS coordinates to the monitoring server [4]. The server, which includes PSTN (Public Switched Telephone Network) phone controller and a monitoring terminal, that is responsible for monitoring the client and emergency management. **Figure 1** shows the system architecture.

2.1. Client Side System

As considered the mobility, BAD with sphygmomanometer, pulsimeter and GPS devices are separated in client side device, yet information delivery by Bluetooth.

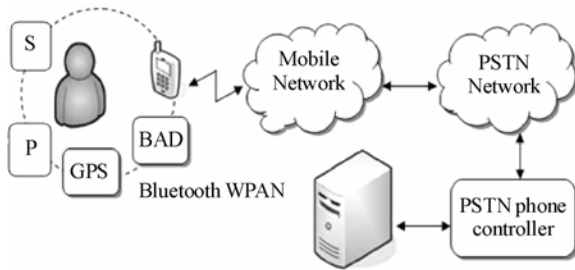


Figure 1. System architecture (P: pulsimeter; S: sphygmomanometer).

Details of BAD with sphygmomanometer, pulsimeter and GPS devices are mentioned in the following:

1) **BAD:** The main function is to monitoring the unusual body activity, and communicates with mobile phone by Bluetooth HFP (Hands-Free Profile) [5]. When BAD detects any unusual body responses, the emergent signals and the GPS coordinates information will be delivered to the mobile phone, and they simultaneously transport the signals to the cell phone by Pulsimeter and Sphygmomanometer, and the mobile phone sends such message to the monitoring server through the public mobile network immediately.

2) **GPS Device:** receiving GPS signals. GPS device could deliver GPS signals to BAD by Bluetooth SPP (Serial Port Profile) [6] every 5 seconds to keep BAD updated the latest position information.

3) **Pulsimeter and Sphygmomanometer:** when Pulsimeter and Sphygmomanometer receive any urgency messages from BAD, they immediately measure the urgency messages and transport the results to the cell phone by the BAD of Bluetooth. Then Pulsimeter and Sphygmomanometer transport them every 10 seconds.

2.2. Server Side System

Server side is constructed by PSTN phone controller and the monitoring terminal. When server side PSTN phone controller receives the incoming call from client side mobile phone, it will be forced to connect and output the sound to the monitoring terminal. The monitoring terminal reads the DTMF code and once the terminal determines the emergency signals are correct, it would send out the emergency tone and pop out the emergency screen.

3. HARDWARE ARCHITECTURE SHORT-LISTED

3.1. Client Side Hardware Architecture

Figure 2 details the block diagram of BAD hardware architecture. BAD is mainly constructed by a microprocessor, an accelerometer, Bluetooth transceiver, voice

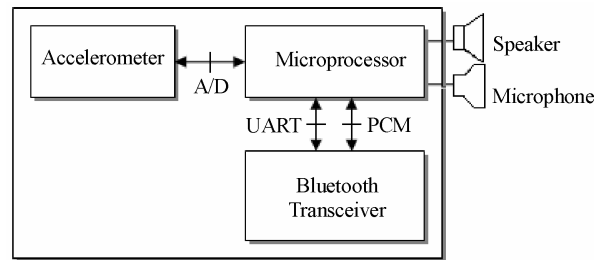


Figure 2. BAD hardware architecture.

device and other accessories. Its functions are detection of the body reaction signals, anomaly analysis, and the control of signal transfer and receive. Explanations of each device are listed below:

1) **Microprocessor:** SC14431 [7] is used as the controller of BAD in this research. SC14431 contains a RISC (Reduced Instruction Set Computer) micro controller, DSP (Digital Signal Processor), and PCM (Pulse Code Modulation) codec. Micro controller is used for operation of Bluetooth protocol stack, and analysis of the signals of accelerometer. DSP and PCM codec are used for sound signal operation and decoding. SC14431 is made by SiTel.

2) **Accelerometer:** MXA2500 Dual Axis Accelerometer [8] is used as the accelerometer in this research. MXA2500 is an electro-mechanical integrate device which can be used to detect the change of acceleration. The change of acceleration is a control point of the body condition in this research. MXA2500 communicates with the microprocessor through the A/D (Analog/Digital) interface. MXA2500 is made by MEMSIC.

3) **Bluetooth Transceiver:** BC03 [9] is used as the baseband IC of Bluetooth transceiver, communicates with the microprocessor through UART and PCM interface. BC03 is made by CSR.

Figure 3 details the block diagram of GPS device hardware architecture. The hardware structure of GPS device is similar to BAD, which contains the microprocessor, GPS module, Bluetooth transceiver and the

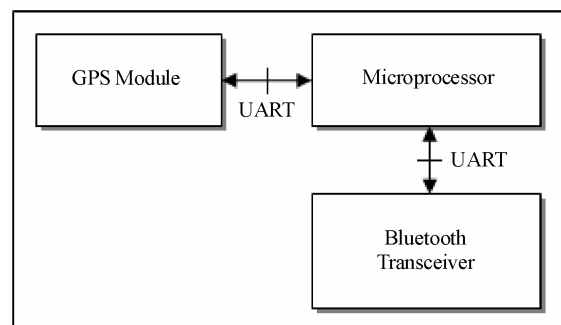


Figure 3. GPS device hardware architecture.

accessories. Microprocessor is used for the operation of Bluetooth protocol stack and receiving of the information of GPS module. Start2 GRF2I [10] is used as the GPS module RF IC and Start2 GSP2e is used as the GPS module baseband IC, which deliver the data to the microprocessor through UART interface. Start2 GRF2i and GSP2e are made by SiRF.

Sphygmomanometer [11-14]: The sphygmomanometer includes LDO (Low Dropout Regulators) as power controller, pressure sensor, filter, amplifier circuit and accessories. The research is using the pressure sensor of SCC series which is manufactured by HoneyWell company. The pressure sensor will transmit different message according to the changing pressure. The message passes through the procedures of magnifying (magnify the micro-message form sensor), and filtering (remove noise), then all the analog messages will be sent to the microcontroller via A/D (Analog/Digital) interface. **Figure 4** shows the block diagram of sphygmomanometer hardware architecture.

Pulsimeter [11-14]: The Pulsimeter includes LDO, pressure sensor, filter, amplifier circuit and accessories. The circuit is using the SCC series of HoneyWell company, but it is a different sensitivity pressure sensor. Putting sensor pad on pulse of hand, the pressure sensor will convert the normal pulse beat to a larger voltage output by magnifying, filtering, comparing (transform to digital signal) then inputs it into microcontroller. **Figure 5** is shown the block diagram of Pulsimeter.

3.2. Server Side Hardware Architecture

Figure 6 details the block diagram of server side hardware Architecture. Server side includes a PSTN phone controller and a monitoring terminal. Furthermore, PSTN

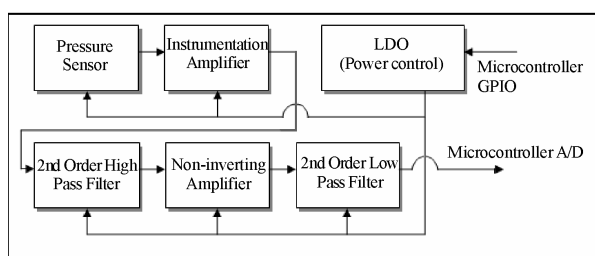


Figure 4. Sphygmomanometer hardware architecture.

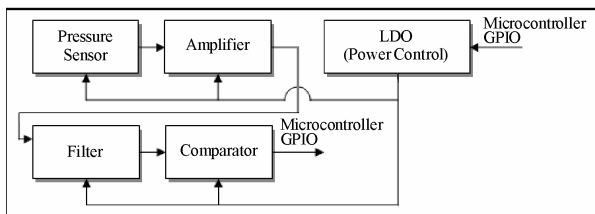


Figure 5. Pulsimeter hardware architecture.

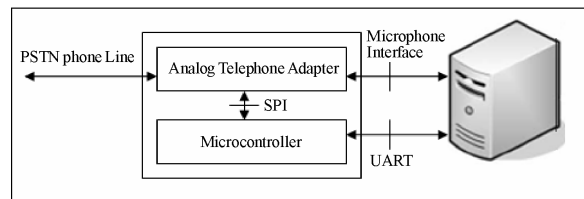


Figure 6. Server side hardware architecture.

phone controller is constructed by ATA (Analog Telephone Adapter), microcontroller, and the accessories, which takes the incoming call from the client. W681388 [15] is used as the baseband IC of ATA for ring detection and coding of signals of voice. PIC24FJ64 [16] is used as microcontroller, which receives the command of the monitoring terminal through the UART interface and controls W681388 Hook ON/OFF and voice output through SPI(Serial Peripheral Interface) interface. W681388 is made by Winbond. PIC24FJ64 is made by Microchip.

4. WIRELESS PERSONAL AREA NETWORK BASE ON BLUETOOTH

Bluetooth provides point to point and multipoint wireless connection according to the internet concept. Within any active communication scope, any devices are treated the same. The first one requesting communication is called master, and the passive one to accept signal is called slave. A master and one or more slaves construct the Piconet of Bluetooth [17,18]. Due to the reason that not all the mobile phone with Bluetooth function in the current market support Serial Port Profile, the GPS device used in this research cannot connect with all the mobile phone with Bluetooth via Bluetooth function. In order to cover most of the mobile phone with Bluetooth in the market in this research and make an active Piconet, we use the Bluetooth device of BAD as master, and the Bluetooth devices of mobile phone and GPS as slave. The Bluetooth of BAD connects with the Bluetooth of mobile phone and GPS and form a PAN (Personal Area Network) upon Bluetooth. **Figure 7** indicates the Bluetooth Piconet in this research.

5. SIGNAL PROCESSING

BAD in this research contains two different modes according to different body conditions, which are body stimulation mode and body activity detection mode respectively. Here are the details below:

5.1. Body Stress-Reaction Mode Signal Processing

In this mode, it means the system detect the body condition has changed from a low activity level to a continuing high consumption level and it represents there is something happened [19]. Then BAD turns into the

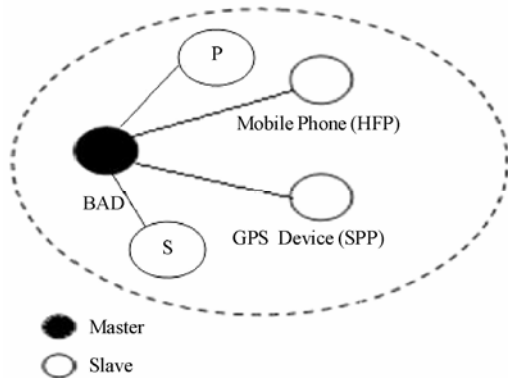


Figure 7. Client side bluetooth piconet (P: pulsimeter; S: sphygmo-manometer).

emergency processes right away. For example if the user falls down or breaks out epilepsy, the change of energy reaction would trigger the emergency task. **Figure 8** indicates the sample accelerometer signal in the low activity level of body. **Figure 9** indicates sample of accel-

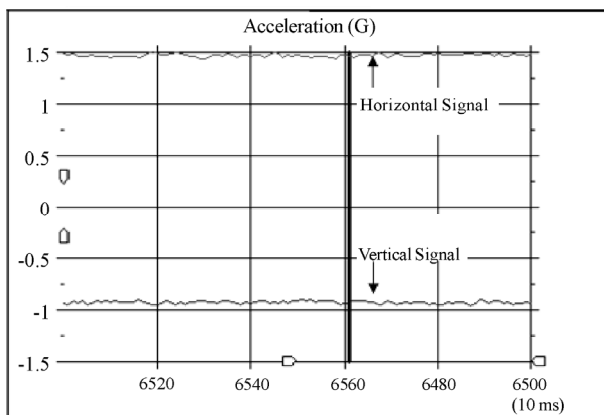


Figure 8. Sample of accelerometer signal in the low activity level of body.

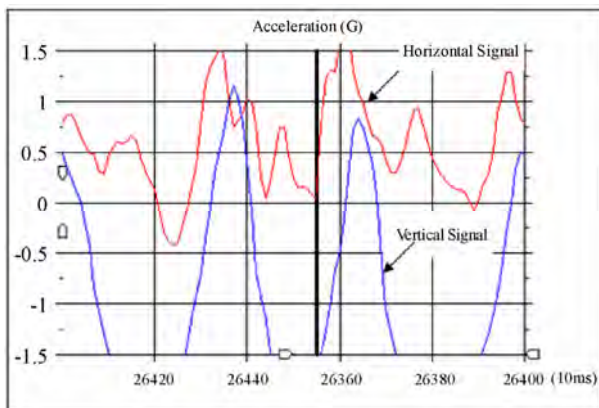


Figure 9. The sample accelerometer signal in the high activity level of body.

erometer signal in the high activity level of body. **Figure 10** indicates the body stress-reaction mode procedure flow chat.

Microprocessor reads the signal from accelerometer every 10 milliseconds, and pass the signal through one order passive HPF (High Pass Filter). Refer to **Eq.1** [19], and then calculate the RMS (Root Mean Square). Refer to **Eq.2**, if the RMS is upper than the preset dynamic RMS threshold for a period of time, it means that emergency has occurred. The system would beep out the warning sound in the first place and if the user does not turn off the alarm, the system would start emergency procedure.

$$Y(n) = \frac{R \times C \times (X(n) - X(n-1) + Y(n-1))}{(T + R \times C)} \quad (1)$$

HPF is used to screen out the signals over 1HZ. While the signal is over 1HZ it means it is not the system targeted signals. It perhaps just comes from the shaking or noises of the devices. 1HZ HPF RC = 0.16, T = 0.01 (100HZ) [19].

$$Y(rms) = \sqrt{\frac{1}{n} \sum_{i=1}^n Y_i^2} \quad (2)$$

RMS: The accelerometer provides absolute analog (AC) outputs, so we need to transform the AC signals into the equal DC signals.

5.2. Body Activity Detection Mode Signal Processing

This mode is opposite to the body stress-reaction mode, which means it detects the body activity turning from the

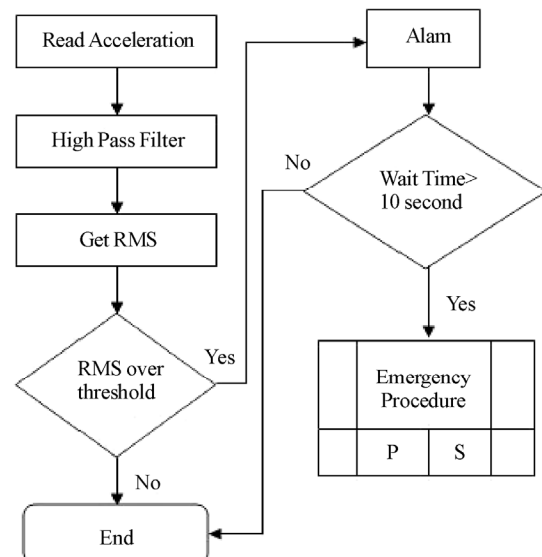


Figure 10. Body stress-reaction mode procedure flow chat.

normal level to a low activity level. It represent something wrong might happened as well [19], and BAD starts the emergency procedures immediately. For example if the user passes out while exercising or if there is no move reaction while working. **Figure 11** presents the body activity detection mode procedure flow chart.

Microprocessor reads the signal from accelerometer every-10 milliseconds, and pass the signal through one order passive HPF (High Pass Filter). Refer to **Eq.1** [19], and then calculate the RMS (Root Mean Square). Refer to **Eq.2**, if the RMS is lower than the preset static RMS threshold for a period of time, it means that emergency has occurred. The system would beep out the warning sound in the first place and if the user does not turn off the alarm, the system would start emergency procedure.

5.3. Emergency Mode Signal Processing

When BAD determines there is a unusual condition, it would beep out the warning sound in the first place to inform the user there is a problem detected, and if the user-does not turn off the alarm, BAD would deliver the ATD dialing command to the mobile phone through Bluetooth HFP [5], and mobile phone would build up a voice connection with the terminal. While remote party answered call active, BAD deliver the emergency signals with sphygmomanometer, pulsimeter and GPS informa-

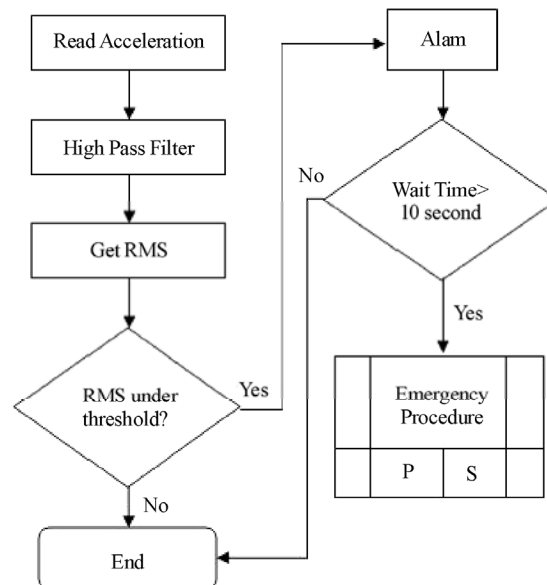


Figure 11. The body activity detection mode procedure flow chat.

tion to the monitoring server via HFP by DTMF [5] till the server is disconnected. **Figure 12** presents the signal process of emergency procedure.

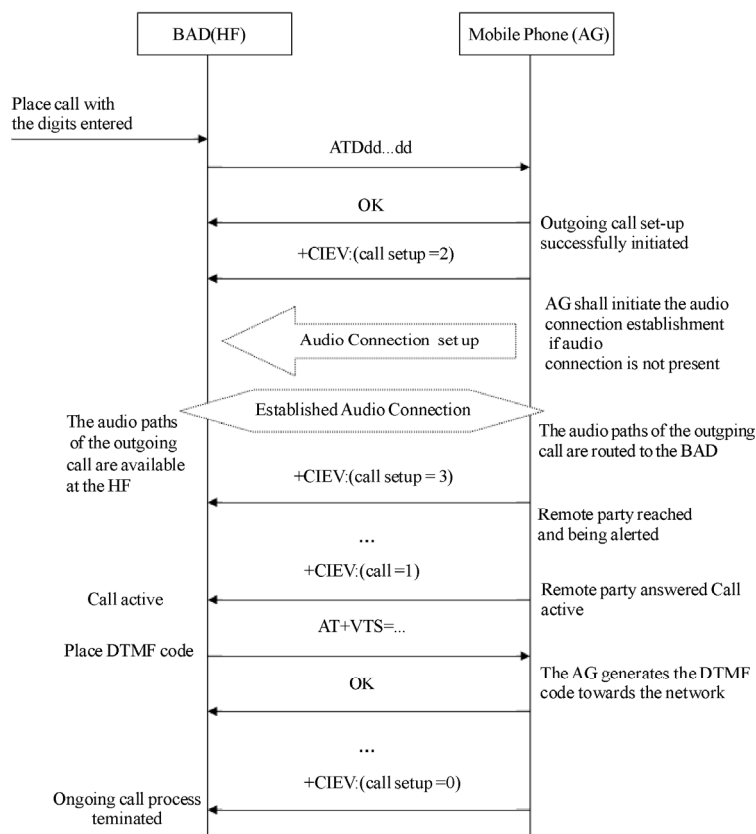


Figure 12. The signal processing of emergency procedure.

6. CONCLUSIONS

This research provides a simple, practical, and portable device of real-time monitoring human body activity to design a BAD with sphygmomanometer, pulsometer and GPS devices, combining mobile phone technology. These devices detecting user being in both dynamic and static emergency by body stress-reaction mode and body activity detection mode separately, and suggests a solution in the emergency situation. Especially for senior care and patients who do face a risk, we expect people, who carry with this device, would have more effective care and help from others.

REFERENCES

- [1] Cummins, R.O., Eisenberg, M.S., Hallstrom, A.P. and Litwin, P.E. (1985) Survival of out-of-hospital cardiac arrest with early initiation of cardiopulmonary resuscitation. *American Journal of Emergency Medicine*, **3**(2), 114-119.
- [2] Albarede, J.L., Lemieux, A., Vellas, B. and Groulx, B. (1989) Psychological factors in falls in elderly patients. *Canadian Journal of Psychiatry*, **34**(2), 94-96.
- [3] Maki, B.E., Holliday, P.J. and Topper, A.K. (1991) Fear of falling and postural performance in the elderly. *Journal of Gerontology*, **46**(4), 123-131.
- [4] Wang, C.S., Lee, J.H. and Chu, Y.T., (2007) Mobile telemedicine application and technologies on GSM. *Bioinformatics and Biomedical Engineering, ICBBE, the 1st International Conference*, 6-8 July 2007, 1125-1128.
- [5] Bluetooth Special Interest Group (2005) Bluetooth Specification, *Hands-Free Profile (HFP) 1.5*, November 25.
- [6] Bluetooth Special Interest Group (2001) Bluetooth specification. *Serial Port Profil*, **1.1**, February 22.
- [7] National Semiconductor Inc. (2005) SC14440/431/432, SC14435, SC14436/437/438. Baseband Processor for PP/FP DECT and WDC, **1.1**, June 16.
- [8] MEMSIC Inc. (2007) MXA2500G/M Improved, Ultra Low Noise ± 1.7 g Dual Axis Accelerometer with Absolute Outputs, Rev. G, June.
- [9] CSR Inc. (2006) BlueCore3-ROM CSP Product Data Book, November.
- [10] SiRF Inc. (2003) SiRF starIIe/LP Chip Set Data Sheet, Rev **1.1**, February.
- [11] Nissila, S., Sorvisto, M., Sorvoja, H., Vieri-Gashi, E. and Myllyla, R. (1998) Non-invasive blood pressure measurement based on the electronic palpation method. *Engineering in Medicine and Biology Society, Proceedings of the 20th Annual International Conference of the IEEE*, **4**, 1723-1726.
- [12] Y.-B. Lin and I. Chlamtac, (2000) Wireless and mobile network architectures. Wiley Computer Publishing, New Delhi.
- [13] Wang, C.-S. (2010) Mobile and wireless technologies applying on sphygmomanometer and pulsometer for patients with pacemaker implementation and other cardiovascular complications. *Journal of Biomedical Science and Engineering*, **3**(1), 47-51.
- [14] HoneyWell, (2002) SSC Series Pressure Sensors 0-5 psi Through 0-300 psi.
- [15] Winbond Inc., (2006) W681388 Single Programmable Extended CODEC/SLIC, Ver. **1.0**.
- [16] Micrpchip Inc., (2007) PIC24FJ64GA004 Family Data Sheet.
- [17] Bluetooth Special Interest Group (2004) Specification of the Bluetooth System Core, Ver., **2.0**.
- [18] Pravin Bhagwat Reefedge Inc., (2001) Bluetooth: Technology for short-range wireless apps, *IEEE Internet Computing*, **5**, 96-103.
- [19] MEMSIC Inc., (2005) Body Activity Detection Reference Design, August 25.

Use of traditional Chinese medicine in HIV/AIDS in China*

Jian Wang, Wen Zou, Ying Liu

Traditional Chinese Medicine Center for AIDS Prevention and Treatment, China Academy of Chinese Medicine Sciences, Beijing, China.

Email: 62tiger@163.com

Received 20 May 2010; revised 8 June 2010; accepted 22 June 2010.

ABSTRACT

This paper gives a general introduction of HIV/AIDS treatment with Traditional Chinese Medicine (TCM) in China during the past 20 years. Although the role of TCM in treatment of HIV/AIDS is promising, there is still a long way to go.

Keywords: HIV/AIDS; Traditional Chinese Medicine (TCM)

1. INTRODUCTION

Since the early 1980's over 40 million individuals have infected with HIV worldwide and over 12 million have died. In China there had by 2009 been 319,877 cases were identified as HIV/AIDS [1]. The medical, social and economic implications of HIV infection are devastating.

In 1996, protease inhibitor therapy became widely available for use in the treatment of HIV infection, thus a decline in HIV-related morbidity and mortality had been reported. Over the last decade, more and more Chinese HIV/AIDS patients turn to seek TCM treatment, among the reasons commonly cited for the use of TCM by patients with HIV infection are: expectation of good effect, reduction of symptoms from the disease or reduction of medicine side effect, or desire for improved quality of life and increased control over the disease process. In all, there is a growing need in china for TCM to support people living with HIV/AIDS, to help to alleviate some of the side effects of the drug therapy, to improve quality of life and to assist in the treatment of individuals who are either unwilling, unresponsive or resistant to combination therapy.

This paper gives a general introduction of use of traditional Chinese medicine in HIV/AIDS in China over the past 20 years.

2. TCM VS AIDS

TCM is a complete medical system with its own unique philosophy, diagnostics and treatment methods which is different from conventional therapy. As a kind of medical system with thousands years of history, the reason why TCM could exist after such a long time is efficacy in clinical practice that help ancient people alive under arduous climate conditions. The basis of TCM theory is Yin-yang and five elements which related to the whole universe, so TCM views the human body and nature as integral not divided. A healthy human is under the state of relatively dynamic balance maintained by both inside and outside of the body, if the balance is broken, the illness occurs. TCM aims to recover the balance of human body, just as the old saying in TCM bible "The Yellow Emperor's Classic of Internal Medicine": once Yin balances with Yang, there comes the harmony of the body and the spirit.

Syndrome differentiation and integral regulation are two main characteristics of TCM. TCM focuses on differentiation of syndromes with the holistic and dynamic perspective and aims to the patient with suffering disease instead of only the disease itself. The constitution of the patient is different, the illness phase is various, the body response is diverse, the manifestation is not the same, and therefore the treating principle should be varied.

Because AIDS is a "new" disease, having only been identified in 1981, there is no specific research on the disease from the past or in the classics. TCM does possess a large body of information about infectious diseases and epidemics, and ways to describe the symptoms of those suffering from AIDS. AIDS can be defined in several different ways according to TCM pattern identification. TCM uses the term "yi bing" (infectious epidemic diseases), to describe epidemic diseases such as AIDS, which are caused by invading evils (viruses). AIDS can also be thought of as a "pestilence," The Chinese term for this is "wen yi", such a disease was thought to have a long latency, sudden onset, and severe symptoms. TCM methods used for treating AIDS is di-

*Granted Fund: State Major Science & Technology Specific Projects (2008ZX10005-001)

verse, such as herbal medicine, acupuncture and moxibustion, Qigong, which aims to enhance immune function of the body, delay the development of disease, reduce or remove the symptom-signs, so as to improve quality of life and prolong life expectancy. The purpose of TCM is to support the strong energy and body resistance so as to inhibit the progress of disease. Someone has enough strong energy and body resistance in TCM, even if infected with HIV, he can live with it, being a long term HIV carrier, so as to postpone onset and death. In all, from our point of view, the best time of intervening in AIDS with TCM is: For asymptomatic stage (HIV carrier) patients, the key aim of TCM is to maintain and enhance the immune-function so as to delay its progression to AIDS stage. For AIDS stage, TCM treatment focuses on relieving symptoms of patients who have AIDS-related opportunistic infection so as to improve the quality of life or combines with HAART therapy to alleviate the side effect of biomedical drugs.

3. WHERE IS THE EFFECTIVE EVIDENCE?

3.1. Chinese Herbal Medicine Screening

Tens of thousands of herbs have been screened for anti-HIV activity. More than 140 kinds of herbs demonstrated to harbor HIV inhibitory activity, such as *Radix Arnebiae*, *Herba Violae*, *Flos Lonicerae*, *Flos Chrysanthemi Indici*, *Fructus Mume*, *Cortex Cinnamomi*, *Fructus Ligustri Lucidi* *et al.* [2-5] Some bioactive materials extracted or isolated from medicinal herbs showed inhibition of HIV activity as well: polysaccharides (such as polysaccharides of *Radix Ginseng*, *Glossogyne tenuifolia* Cass, *Radix Astragali*, *Ganoderma Lucidum* seu *Japonicum*, *Radix Actinidiae*); protein components (such as glucoprotein in *Aloe*, a component from *Radix Trichosanthis*, α and β Momordicines in *Momordica charantia*, Ricin bond A, cimigenol saponin); alkaloids (such as castanospermine and colchicines); lactones (such as baicalein and hypericin); terpenes (such as glycyrrhizin and goddypol) *et al.* Mechanisms of action included inhibition of reverse transcriptase, protease inhibition and integrase inhibition or interference of infection at the viral cell entry level. Among them, *Trichosanthin* is a kind of prospective one that acquired worldwide attention, it was shown to inhibit HIV replication in infected cells of lymphocyte and mononuclear phagocytic lineage, with no measurable toxicity in uninfected cells, and it was applied in the treatment of patients with AIDS or AIDS-related complex in phase I and II studies [6-11].

Many more herbs or herb extracts may attenuate the course of HIV infection via immune enhancement, cytokine or other pathways, such as *Radix Astragali*, *Cordy-*

ceps been reported to enhance helper lymphocyte T and promote CD4/CD8 ratio. [12-13] Shikonin was shown to decline the expression of CCR5 and CCR5mRNA [14].

Many herbal compounds have been tested to have potent HIV inhibitory activity and their experimental or clinical manifestation may provide valuable leads for further investigations. For instance, Xiao chaihu tang, [15] Zhongyan-1, [16] Zhongyan-2, Zhongyan-4, Compound SH [17], Tangcao Tablets *et al.*

3.2. Clinical Trials

According to the regulation of State Food and Drug Administration (SFDA) in China, new Chinese patent medicine treating AIDS can be classified into anti-HIV patent that testified through *in vitro* and *in vivo* experiments and patent supplementary for AIDS treatment that either adds synergistic effect or alleviates toxic-side effect on antiretroviral drugs already existed. Tangcao Tablets is the first patent approved by SFDA for alleviating symptoms and signs of HIV/AIDS patients, 5 other relatively matured compounds (Qiankunling Tablets, Keaite capsule, Chuankezhi injection, Zhongyan-2 Granule and Compound Sanhuangsan) are still under clinical trials.

Tangcao Tablets: Wu Hao *et al.* [18] recruited 173 HIV/AIDS participants for randomized double blind placebo controlled clinical study in 5 medical centers for 6 months, result showed that Tangcao Tablet could significantly raise CD4 count, increase weight and CD4/CD8, and it was possible to delay the replication of HIV.

Zhongyan-4 Granule: Wang Jian *et al.* [19] recruited 72 HIV/AIDS participants for a randomized double-blind placebo-controlled trial for 6 months. Results showed that 15 out of 30 patients in Zhongyan-4 group had their CD4 counts increased by $7.70 \pm 150.96/\text{mm}^3$, markedly higher than that in placebo group, no adverse reaction was found.

Qiankunling Tablets: Shi Dan *et al.* [20] recruited 36 HIV/AIDS participants for a randomized double-blind placebo-controlled trial for 7 months. The results showed that significant difference of plasma HIV-1RNA level was found between patients treated with Qiankunling Tablet and those treated with placebo for control after they were medicated for 7 months, suggesting the Qiankunling tablet was effective in reducing viral load. Moreover, in the next 3 months open treatment, it illustrated further the evident effect of Qiankunling Tablets in reducing plasma level of HIV-1RNA, and raising CD4 dose-dependently. Symptoms and QOL in patients were improved as well.

Xiaomi Granule: Chen Jizhong [21] recruited 34 HIV/AIDS patients with oral candidiasis for a two weeks RCT trial, Participants were randomized into two groups, the 34 cases in treatment group received Xiaomi Granule,

and the 34 cases in control group received Nystatin. The result showed that Xiaomi Granule group had better effect than the controlled group, and a lower reoccurrence rate was found after two weeks follow-up.

3.3. Medical Care

TCM intervention on HIV/AIDS treatment started from 2004, a pilot project named National Free TCM HIV/AIDS Treatment Program had been launched by The State Administrative Bureau of Traditional Chinese Medicine, and quickly scaled up from 5 provinces (Henan, Hebei, Anhui, Hubei, Guangdong) to 19 provinces, autonomous regions, and municipalities in China including some places with high prevalence, 9267 cases have been treated with TCM accumulatively. The therapeutic effects on 8946 cases from pilot project are as follows: most of the cases maintained stable immune function; main symptoms and signs like fever, cough, fatigue, poor appetite, diarrhea had significantly been improved ($P < 0.001$), no adverse reaction was found in TCM treatment.

4. HOW TO EVALUATE THE EFFECTIVENESS?

Current used effectiveness evaluation gold standard: viral load and CD4+T cell count seemed to be not proper for TCM. Some AIDS patients had improved quality of life or prolonged life after TCM treatment, but their viral load might be still in a high level and CD4+T cell count can't see significant elevation. As to patients, improvement in quality of life rather than biomedical parameters changes matters so much to them. So if TCM clinical effectiveness evaluation take items such as patients reported outcomes (PRO), quality of life, clinical end points (morbidity, mortality, life span), activities in daily life (work ability) *et al.* into consideration, or even let those items play key part in the evaluation, that might be more appropriate for TCM evaluation.

From 2008, China State Major Science & Technology Specific Projects granted about 100 million on TCM research on HIV/AIDS, which posed big opportunity to TCM researchers. In other words it is also big challenge. Although TCM appears to be associated with improvements in immune function, quality of life, and some AIDS related opportunistic diseases. Definitive conclusions were limited due to variation in designs, comparisons, heterogeneous outcomes and inadequate controls. High-quality, well-controlled, longer randomized trials are needed to better inform clinical decisions in the coming works.

REFERENCES

- [1] Wang, L., Wang, N., Wang, L., Li, D., Jia, M., Gao, X., *et al.* (2009) The 2007 estimates for people at risk for and living with HIV in China: Progress and challenges. *Journal of Acquired Immune Deficiency Syndromes*, **50**(4), 414-418.
- [2] Luo, S.D. and Ju, P. (2006) Compared traditional Chinese medicine and western medicine to treat AIDS. *Journal of Henan University of Chinese Medicine*, **21**(3), 1-3.
- [3] Lam, T.L., Lam, M.L., Au, T.K., *et al.* (2000) A comparison of human immunodeficiency virus type-I protease inhibition activities by the aqueous and methanol extracts of Chinese medicine herbs. *Life Science*, **67**(23), 2889-2896.
- [4] Au, T.K., Lam, T.L., Ng, T.B., *et al.* (2001) A comparison of HIV-1 integrase inhibition by aqueous and methanol extracts of Chinese medicine herbs. *Life Science*, **68**(14), 1687-1694.
- [5] Kobayashi, Y., Watanabe, M., Ogihara, J., *et al.* (2000) Inhibition of HIV-1 reverse transcriptase by methanol extracts of commercial herbs and spices. *Journal of the Japanese Society for Food Science and Technology*, **47**(8), 642-645.
- [6] McGrath, M.S., Santulli, S. and Gaston, I. (1990) Effects of GLQ223 on HIV replication in human monocyte/macrophages chronically infected *in vitro* with HIV. *AIDS Research and Human Retroviruses*, **6**(8), 1039-1043.
- [7] McGrath, M.S., Hwang, K.M., Caldwell, S.E., *et al.* (1989) GLQ223: An inhibitor of human immunodeficiency virus replication in acutely and chronically infected cells of lymphocyte and mononuclear phagocyte lineage. *Proceedings of the National Academy of Sciences*, **86**(8), 2844-2848.
- [8] Byers, V.S., Levin, A.S., Malvino, A., *et al.* (1994) A phase II study of effect of addition of trichosanthin to zidovudine in patients with HIV disease and failing anti-retroviral agents. *AIDS Research and Human Retroviruses*, **10**(4), 413-420.
- [9] Mayer, R.A., Sergios, P.A., Coonan, K., *et al.* (1992) Trichosanthin treatment of HIV-induced immune dysregulation. *European Journal of Clinical Investigation*, **22**(2), 113-122.
- [10] Byers, V.S., Levin, A.S., Waites, L.A., *et al.* (1990) A phase I/II study of trichosanthin treatment of HIV disease. *AIDS*, **4**(12), 1189-1196.
- [11] Kahn, J.O., Kaplan, L.D., Gambertoglio, J.G., *et al.* (1990) The safety and pharmacokinetics of GLQ223 in subjects with AIDS and AIDS-related complex: A phase I study. *AIDS*, **4**(12), 1197-1204.
- [12] Gai, L., Song, C.Q., Hu, Z.B., *et al.* (2001) Review of anti-HIV plants. *Foreign Medical Sciences*, **23**, 139.
- [13] He, J.H. and Mai, E.D. (2004) Review of AIDS treatment with Chinese medicine. *Chinese Pharmaceutical and Clinical Research*, **4**, 454.
- [14] Chen, X., Yang, L., Zhang, N., *et al.* (2003) Shikonin, a component of Chinese herbal medicine, inhibits chemokine receptor function and suppresses human immunodeficiency virus type 1. *Antimicrobial Agents and Chemotherapy*, **47**(9), 2810-2816.
- [15] Zhang, Z.J. (1995) The phagocytosis of HIV infected cells by Xiao chaihu tang extracts. *Foreign Medical Sciences*, **17**, 64.
- [16] Guan, C.F. (1995) Experimental study of SIV infected monkey model treatment by Zhongyan-1. *Chinese Jour-*

nal of Information on Traditional Chinese Medicine, **2**, 42-46.

- [17] Kusum, M., Klinbuayaem, V., Bunjob, M., *et al.* (2004) Preliminary efficacy and safety of oral suspension SH, combination of five Chinese medicinal herbs, in people living with HIV/AIDS; the phase I/II study. *Journal of the Medical Association of Thailand*, **87**(9), 1065-1070.
- [18] Wu, H., Zhang, F.J., Yao, C., *et al.* (2004) Clinical study of Tangcao tablet in treating HIV/AIDS. *Compilation of Theses of Treatment and Research on AIDS*, **3**, 95-103.
- [19] Wang, J., Yang, F.Z., Zhao, M., *et al.* (2006) Randomized double-blinded and controlled clinical trial on treatment of HIV/AIDS by Zhongyan-4. *Chinese Journal of Integrative Medicine*, **12**(1), 6-11.
- [20] Shi, D. and Peng, Z.L. (2003) Randomized double blind placebo paralleled clinical research on HIV/AIDS with Qiankunning tablets. *Study Journal of Traditional Chinese Medicine*, **21**, 1472-1474.
- [21] Chen, J.Z. (2009) Xiaomi granule on HIV/AIDS patients with oral candidacies. *Guangming Journal of Chinese Medicine*, **24**, 633-636.

Journal of Biomedical Science and Engineering (JBiSE)

www.scirp.org/journal/jbise

JBiSE, an international journal, publishes research and review articles in all important aspects of biology, medicine, engineering, and their intersection. Both experimental and theoretical papers are acceptable provided they report important findings, novel insights, or useful techniques in these areas. All manuscripts must be prepared in English, and are subject to a rigorous and fair peer-review process. Accepted papers will immediately appear online followed by printed in hard copy.

Subject Coverage

- Bioelectrical and neural engineering
- Bioinformatics and Computational Biology
- Biomedical modeling
- Biomedical imaging, image processing and visualization
- Clinical engineering, wearable and real-time health monitoring systems
- Biomechanics and biotransport
- Software, tools and application in medical engineering
- Biomaterials
- Physiological signal processing
- Biomedical devices, sensors, artificial organs and nano technologies
- NMR/CT/ECG technologies and electromagnetic field simulation
- Structure-based drug design

Notes for Intending Authors

Submitted papers should not have been previously published nor be currently under consideration for publication elsewhere. Paper submission will be handled electronically through the website. All papers are refereed through a peer review process. For more details about the submissions, please access the website.

Website and E-Mail

www.scirp.org/journal/jbise

Email: jbise@scirp.org



Editor-in-Chief

Kuo-Chen Chou

Gordon Life Science Institute, San Diego, California, USA

Editorial Board

Prof. Suleyman I. Allakhverdiev	Institute of Basic Biological Problems, Russia
Prof. Christopher J. Branford-White	London Metropolitan University, UK
Prof. Thomas Casavant	University of Iowa, USA
Dr. Arezou Ghahghaei	University of Sistan ad Baluchistan, Iran
Prof. Reba Goodman	Columbia University, USA
Prof. Fu-Chu He	Chinese Academy of Science, China
Prof. Robert L. Henrikson	Proteos, Inc., USA
Prof. Zeng-Jian Hu	Howard University, USA
Prof. Sami Khuri	San Jose State University, USA
Prof. Takeshi Kikuchi	Ritsumeikan University, Japan
Prof. Rob Krams	Imperial College, UK
Prof. Lukasz Kurgan	University of Alberta, Canada
Dr. Girdhar K. Pandey	University of Delhi South Campus, India
Prof. Zhi-Pei Liang	University of Illinois, USA
Prof. Juan Liu	Wuhan University, China
Dr. Patrick Ma	The Hong Kong Polytechnic University, China
Dr. Bouzid Menaa	Fluorotronics, Inc. USA
Prof. Eddie Ng	Technological University, Singapore
Prof. Harold A. Scheraga	Cornell University, USA
Prof. Hong-Bin Shen	Shanghai Jiaotong University, China
Prof. Min-Gui Sun	University of Pittsburgh, USA
Prof. Yan-Mei Tie	Harvard Medical School, USA
Dr. Elif Derya Ubeyli	TOBB University of Economics and Technology, Turkey
Prof. Ching-Sung Wang	Oriental Institute Technology, Taiwan (China)
Prof. Dong-Qing Wei	Shanghai Jiaotong University, China
Prof. Zhi-Zhou Zhang	Harbin Institute of Technology, China
Prof. Jun Zhang	University of Kentucky, USA

ISSN 1937-6871 (Print), 1937-688X (Online)

TABLE OF CONTENTS

Volume 3 Number 8

August 2010

Dextran coating on and among fibers of polymer sponge scaffold for osteogenesis by bone marrow cells <i>in vivo</i> M. Yoshikawa, N. Tsuji, H. Kakigi, T. Yabuuchi, Y. Shimomura, H. Hayashi, H. Ohgushi.....	751
Antimicrobial activity of the autochthonous compound Enoxil L. Lupaşcu, V. Rudic, V. Cotos, T. Lupaşcu.....	758
MRI monitoring of lesions created at temperature below the boiling point and of lesions created above the boiling point using high intensity focused ultrasound C. Damianou, K. Ioannides, V. Hadjisavvas, N. Mylonas, A. Couppis, D. Iosif, P. A. Kyriacou.....	763
Anisotropic WM conductivity reconstruction based on diffusion tensor magnetic resonance imaging: a simulation study D. D. Yan, W. L. Xu, J. Li.....	776
Categorizing HIV-1 subtypes using an ant-based clustering algorithm D. King, W. Hu.....	785
Innovative data mining approaches for outcome prediction of trauma patients E.-M. Theodoraki, S. Katsaragakis, C. Koukouvinos, C. Parpoula.....	791
Uncovering preferences from patient list data using benefit efficient models J. Ubøe, J. Lillestøl.....	799
Study of the bones tissue reparation using nanostructured titanium implants with hydroxylapatite coatings by scanning electron microscopy T. V. Pavlova, S. Y. Zaitsev, L. A. Pavlova, D. A. Kolesnikov.....	807
Shoulder joint flexibility in top athletes H. Daneshmandi, F. Rahmaninia, H. Shahrokhi, P. Rahmani, S. Esmaili.....	811
Use of instantaneous energy of ABR signals for fast detection of wave V A. Arooj, M. M. Rushaidin, S.-H. Salleh, M. H. Omar.....	816
Tele-care for emergency announcements C.-S. Wang, C.-W. Liu, T.-W. Wang.....	822
Use of traditional Chinese medicine in HIV/AIDS in China J. Wang, W. Zou, Y. Liu.....	828